

**HOLLOW GLASS WAVEGUIDES WITH MULTILAYER POLYSTYRENE AND
METAL SULFIDE THIN FILM COATINGS FOR IMPROVED INFRARED
TRANSMISSION**

By Valencia S. Johnson

A dissertation submitted to the
Graduate School – New Brunswick
Rutgers, The State University of New Jersey
in partial fulfillment of the requirements
for the degree of
Doctor of Philosophy

Graduate Program in Ceramics and Materials Science and Engineering

written under the direction of

Professor James A. Harrington

and approved by

New Brunswick, New Jersey

October, 2007

ABSTRACT OF THE DISSERTATION

Hollow Glass Waveguides With Multilayer Polystyrene and Metal Sulfide Thin Film Coatings For Improved Infrared Transmission

By Valencia S. Johnson

Dissertation Director:

Professor James A. Harrington

The overall goal of this project was to improve transmission of infrared radiation in hollow waveguides. First, polystyrene was studied as a new dielectric material for silver-coated hollow glass waveguides. The deposition and performance of polystyrene, as a single dielectric layer, were investigated. The potential of polystyrene as the low index of refraction material in a multilayer coating was also demonstrated. Cadmium sulfide and lead sulfide were each considered as the high index material in the multilayer stack. Multilayer silver coated hollow glass waveguides can be formed using polystyrene and either cadmium sulfide or lead sulfide. These material pairs are interesting because they form a multilayer structure with high index contrast, which can significantly lower the loss of a waveguide.

The deposition of lead sulfide was also optimized in this project. Lead sulfide, as a single layer dielectric coating, is an attractive material for transmission of longer wavelength radiation, especially 10.6 μm . It is also of interest for emerging applications such as metals processing by lasers because hollow waveguides with silver and lead sulfide can make a low loss waveguide. Losses as low as 0.1dB/m were achieved.

The deposition of zinc sulfide and zinc selenide was also investigated in this project. They are of interest because of their small extinction coefficients at longer wavelengths and potential for use in waveguides used for materials processing. The numerous simultaneous chemical reactions occurring during deposition of these materials makes obtaining pure films difficult.

Gold was evaluated as a replacement for silver as the highly reflecting metallic layer. It was considered an attractive alternative because it has greater resistance to degradation in high temperature and corrosive environments.

All samples were made using an electroless process. Characterization of the samples was performed using the optical techniques of FTIR and UV-visible spectroscopy. Loss measurements were performed in the laboratory using Er:YAG and CO₂ infrared lasers. Profilometry measurements were conducted to quantify the roughness of the polymer films and the metal sulfide films. Polymer films had roughness values between 25 and 40 nm and when overcoated with CdS the roughness increased to 240 nm.

Acknowledgements

First, I would like to THANK GOD!!! I have FINALLY reached the point.

I would like to thank Professor James A. Harrington for his gentle prodding and calm leadership. I would like to thank Professors Lisa Klein and George Sigel for being members of my committee and able educators while I was conducting these experiments.

I would also like to thank Dr. David Johnson (no relation!) for being an ear and a shoulder when I needed either one both here at Rutgers and at Stevens. I would also like to thank Prof. Matthewson for serving on my committee.

I would like to thank my parents for their initial support of my pursuit of this degree.

I am forever grateful for the efforts of my labmates both past and present: Veena Gopal, Pal Pedersen, Roshan George and Bradley Bowden. I would also like to thank other graduate students who helped me along the way with equipment (Navin Venugopal), or friendship (Ray Brennan, Cari August, and Asha Hall).

TABLE OF CONTENTS

ABSTRACT OF THE DISSERTATION.....	ii
ACKNOWLEDGEMENTS	iv
TABLE OF CONTENTS	v
LIST OF FIGURES	viii
LIST OF TABLES	xiii
Chapter I Introduction	1
I.A GENERAL INTRODUCTION	1
I.B ORGANIZATION OF THE DISSERTATION.....	2
I.C RELEVANCY OF WORK.....	2
I.D CLASSIFICATION OF HOLLOW WAVEGUIDES.....	5
I.E FUNDAMENTALS OF MULTILAYER HOLLOW WAVEGUIDES.....	6
I.F DEPOSITION PROCESS	10
REFERENCES	17
Chapter II Theory	21
II.A GENERAL	21
II.B MS THEORY.....	22
II.B.1 MS THEORY FOR STRAIGHT LOSS.....	22
II.B.2 MS THEORY FOR BENDING LOSS	31
II.C MK THEORY	32
II.C.1 MK THEORY FOR STRAIGHT LOSS	33
II.C.2 MK THEORY FOR MINIMIZING ATTENUATION OF HYBRID MODES	34
II.C.3. OTHER CONTRIBUTORS TO STRAIGHT LOSS.....	42

II.C.4. MK THEORY FOR BENDING LOSS	42
II.D ADDITIONAL BENDING LOSS CONSIDERATIONS	43
II.E COUPLING RADIATION TO WAVEGUIDES	43
II.F SURFACE ROUGHNESS	48
II.G POLYMER CHARACTERISTICS.....	51
REFERENCES	57
Chapter III Lead Sulfide	59
III.A INTRODUCTION	59
III.B PROPERTIES AND PROCESSING	61
III.C. EXPERIMENTAL RESULTS FOR PbS IN A SINGLE DIELECTRIC LAYER HGW.....	64
III.C.1. CO ₂ LASER LOSS MEASUREMENTS – STRAIGHT LOSS	69
III.C.2. CO ₂ LASER LOSS MEASUREMENTS – BENDING LOSS.....	72
III.D CONCLUSIONS.....	74
REFERENCES	75
Chapter IV Polystyrene: Properties and Processing of an Optical Material	77
IV.A.1 GENERAL INTRODUCTION	77
IV.A.2 INTRODUCTION TO POLYSTYRENE.....	80
IV.B PROCESSING.....	84
IV.C EXPERIMENTAL RESULTS AND DISCUSSION	85
IV.C.1 PS Deposition Results and Discussion.....	86
IV.C.2 PS Loss Measurements and Discussion	102
IV.D CONCLUSIONS.....	107
REFERENCES	109

Chapter V	PS in a Multilayer Dielectric HGW	112
V.A	INTRODUCTION	112
V.B	PROCESSING.....	118
V.C	EXPERIMENTAL RESULTS AND DISCUSSION	119
	V.C.1 PS AS THE LOW INDEX DIELECTRIC MATERIAL IN AN ADDITIVE STACK WITH CdS	119
	V.C.2. PS AS THE LOW INDEX DIELECTRIC MATERIAL IN AN ADDITIVE STACK WITH PbS.....	122
	REFERENCES	125
Chapter VI	Potential Dielectric Materials by DLPD: ZnS/ZnSe and Gold	126
VI.A	ZNS/ZNSE INTRODUCTION.....	126
VI.B	ZNS/ZNSE PROCESSING	130
	VI.B.1 ZNS/ZNSE PROCESSING – LITERATURE REVIEW	130
	VI.B.2. ZNS/ZNSE PROCESSING – EXPERIMENTAL	136
VI.C	ZNS/ZNSE EXPERIMENTAL RESULTS	138
VI.D	ZNSE/ZNS CONCLUSIONS	142
VI.E	GOLD (AU) INTRODUCTION	143
VI.F	PROCESSING AND PROPERTIES OF AU	143
VI.G	RESULTS AND DISCUSSION FOR AU.....	145
	REFERENCES	150
Chapter VII	Conclusions and Future Work	153
	REFERENCES	157
	Curriculum Vita.....	158

LIST OF ILLUSTRATIONS

Chapter I

Figure I-1	A schematic of our electroless Dynamic Liquid Deposition Process (DLPD).[37]	12
Figure I-2	A cross-sectional view of a multi-layer hollow waveguide	16

Chapter II

Figure II-1	A) The planar view of a hollow waveguide of diameter $2a$ and B) the cross sectional view. The radiation propagates in the z direction	24
Figure II-2	Electric field time average energy density for the first 5 modes as determined from a cross section of hollow waveguides[4].	30
Figure II-3	The two types of ray paths and the angles: A) Normal propagation, and B) Whispering gallery mode propagation. [5].....	32
Figure II-4	A) The planar view of a hollow waveguide of diameter $2a$, and B) the cross sectional view[3]	33
Figure II-5	A schematic of the waveguide structure from the centerline (at $x=0$) of the WG to the inner surface of the substrate tubing (at $x=a$) [3]	35
Figure II-6	Calculated reduction of the attenuation for HE ₁₁ mode/attenuation for Ag-only ratio for single layer and multilayer dielectric coatings in Ag coated HGWs at 2.94 μm [3,6]	41

Figure II-7	The increase in attenuation with decreasing bore size for the lowest four hybrid modes[13].	45
Figure II-8	Dependence of measured loss on the launch condition[13].	46
Figure II-9	The optimal value of ω/a varies[10].	47
Figure II-10	A rough surface, with RMS roughness of σ , is shown here. The roughness either increases or decreases the incident angle, θ [12].	49
Figure II-11	The increase in roughness of the silver layer with longer deposition times for our DLPD process, as evidenced by an increase in absorption[17]	50
Figure II-12	A plot showing how F_{film} varies with a_1 , the index of the material coating the metal[3].	52
Figure II-13	A chart showing the value of the extinction coefficient of PS from 4000 cm^{-1} ($2.5 \text{ }\mu\text{m}$) to 1000 cm^{-1} ($10 \text{ }\mu\text{m}$)[24].	54
Figure II-14	An FTIR spectrum of a free-standing COP film.	55

Chapter III

Figure III-1	Optical constants, n and κ , for PbS	61
Figure III-2	Modeled and experimental FTIR spectra of a $320 \text{ }\mu\text{m}$ bore Ag/PbS sample optimized for transmission at $10.6 \text{ }\mu\text{m}$	66
Figure III-3	Modeled and experimental FTIR spectra of a $1,000 \text{ }\mu\text{m}$ bore Ag/PbS sample optimized for transmission at $10.6 \text{ }\mu\text{m}$	67
Figure III-4	FTIR spectrum of a $1,000 \text{ }\mu\text{m}$ bore speckled Ag/PbS sample.	68

Figure III-5	A comparison of the calculated (thinner line) and the measured (thicker line) straight loss for Ag/PbS samples of different inner diameters at 10.6 μm.....	70
Figure III-6	Bending loss for a 1 m long 1,000 μm bore Ag/PbS sample.	73
 Chapter IV		
Figure IV-1	The molecular structure of the monomer, styrene.	80
Figure IV-2	An FTIR spectrum of a free-standing PS film 1.5 mm thick.....	81
Figure IV-3	Viscosity data for PS/toluene solutions of different viscosities.	87
Figure IV-4	FTIR spectra of 3 Ag/PS samples made with different PS concentrations in the coating solutions	88
Figure IV-5	The left side (A) shows extended and well spaced chains as would be expected for a low concentration PS solution. The right side (B) shows more voluminous chain configurations as would be expected in a high concentration solution.....	90
Figure IV-6	The primary peak is shifting to longer wavelengths for slower deposition rates.....	91
Figure IV-7	The primary peak is shifting to longer wavelengths for slower deposition rates.....	93
Figure IV-8	The primary peak is shifting to longer wavelengths for slower deposition rates.....	94
Figure IV-9	This is a schematic of the FCP deposition in which the solution is “pulled” through the WG.....	96
Figure IV-10	The change in thickness for drying conditions can be seen	99

Figure IV-11	Losses measured on Ag/1 wt% PS samples for three different bore sizes (530 μm, 750 μm, and 1,000 μm) using an MPB CO₂ laser	103
---------------------	---	------------

Figure IV-12	Loss values measured for the Er:YAG wavelength with a) a laser as a source and b) FTIR as a source for 530 μm, 750 μm, and 1,000 μm bore waveguides.....	105
---------------------	---	------------

Chapter V

Figure V-1	Modeling showing the decrease in attenuation with a single layer (Ag/PS) and multilayers (Ag/PS/CdS and Ag/PS/CdS/PS) in a HGW at 2.94 μm.	113
-------------------	---	------------

Figure V-2	Modeling showing the decrease in attenuation with a single layer (Ag/PS) and multilayers (Ag/PS/PbS and Ag/PS/PbS/PS) in a HGW at 2.94 μm	114
-------------------	--	------------

Figure V-3	FTIR spectra of a Ag/1 wt% PS sample before and after CdS deposition.....	117
-------------------	--	------------

Figure V-4	The growth rate of CdS on a PS surface as a function of time at room temperature	120
-------------------	---	------------

Figure V-5	Optical constants, n and κ, for CdS.....	121
-------------------	---	------------

Figure V-6	The growth rate of PbS on a PS surface as a function of time at room temperature.	123
-------------------	---	------------

Chapter VI

Figure VI-1	Optical constants, n and κ for ZnSe.....	127
--------------------	---	------------

Figure VI-2	Optical constants, n and κ for ZnS.....	128
--------------------	--	------------

Figure VI-3	Optical constants, n and κ for PbSe	129
Figure VI-4	A comparison of conditions for which ZnS (and/or Zn(OH)₂) and CdS (and/or Cd(OH)₂) formation occurs.....	131
Figure VI-5	An FTIR spectrum of an Ag/ZnSe sample made using Recipe A	139
Figure VI-6	An FTIR spectrum of an Ag/ZnS sample made using Recipe B.....	140
Figure VI-7	An FTIR spectrum of an Ag/ZnS sample made using Recipe C	141
Figure VI-8	Optical constants for Au.....	145
Figure VI-9	A picture of the outer surface of an Au coated tube, as viewed through an optical microscope.....	146
Figure VI-10	A picture of small area of the inner surface of an Au coated tube, as viewed through an optical microscope.	147
Figure VI-11	A picture taken from an optical microscope showing both the bubbling of the underlying Au layer and the particles formed during ZnSe deposition	148

LIST OF TABLES

Chapter II

Table II-1	Waveguide Mode Parameters, U_{nm} .	29
------------	---------------------------------------	----

Chapter III

Table III-1	Cutback lengths of Ag/PbS samples	71
-------------	-----------------------------------	----

Table III-2	Calculated and Measured Loss Values for Ag/PbS at 10.6 μm and previously measured loss values for Ag/AgI comparison	71
-------------	--	----

Chapter IV

Table IV-1	Indices of refraction of polymers used in HW technology [8, 17, 18].	79
------------	--	----

Table IV-2	Properties of Polystyrene 148G K21.[22]	81
------------	---	----

Table IV-3	Characteristics of 3 Common Solvents and PS [23,25]	83
------------	---	----

Table IV-4	PS thickness for different PS/toluene solution concentrations	89
------------	---	----

Table IV-5	PS thickness for different deposition rates	92
------------	---	----

Table IV-6	PS thickness for different drying conditions	100
------------	--	-----

Table IV-7	Profilometry Results of PS alone and Ag/PS/CdS Samples	101
------------	--	-----

Table IV-8	Comparison of loss values for polymers at 2.94 μm (Er:YAG)	107
------------	---	-----

CHAPTER V

Table V-1	Calculated Optimal Thickness for 1,2 and 3 Layer Systems at 2.94 μm	115
------------------	--	------------

CHAPTER VI

Table VI-1	Index Contrast between 3 Potential DLDP Low Index Materials and PbSe	130
-------------------	---	------------

Chapter I Introduction

I.A. General Introduction

The primary goal of this project was to produce hollow glass waveguides (HGWs) which transmit infrared (IR) radiation, within the wavelength range of 2 to 20 μm , with lower total loss than what is currently available. The materials studied in this project were: polystyrene (PS), metal sulfides (cadmium sulfide, CdS, and lead sulfide, PbS), zinc selenide (ZnSe), zinc sulfide (ZnS) and gold (Au). PS was studied as a single dielectric layer, and as the low index dielectric material in a multilayer dielectric coating with either CdS or PbS included as the high index dielectric material. The objective was a better understanding of: (1) the performance of PS alone as an optical material in a hollow waveguide; (2) the potential to deposit a metal sulfide on a PS layer; and (3) the benefit of using a pair of materials (PS and PbS) with a higher index contrast than has been previously achieved. The results of this work are especially interesting because it is the first time Ag/PS/CdS or Ag/PS/PbS multilayers samples were successfully prepared. PbS deposition was optimized to form a single dielectric layer, low-loss HGW for the CO₂ laser at 10.6 μm . The focus of the efforts on Au was in optimizing the deposition on the glass substrate tubing. The use of Au is desirable because it allows our HGWs to be used at higher temperatures, or in more corrosive environments where the Ag film would not be as stable. The work done on Au in this project extends previous work.

I.B. Organization of the Dissertation

The following topics are each the subject of their own chapters in this dissertation:

Introduction, Theory, PbS as a single layer, PS as a single layer, PS as part of a multilayer structure, Potential Deposition by the Dynamic Liquid Phase Deposition process: ZnS, ZnSe and Au, and Conclusions and Future Work. The Theory section will present the mathematical basis for understanding radiation propagation within hollow waveguides and the relationship between materials and performance. Each chapter will include a discussion on processing, performance, a review of the use or potential use of the material in hollow waveguides. The topic of PS in multilayer coatings is in a chapter separate from the PS as a single layer work for clarity. The Potential Deposition chapter will discuss the current progress to deposit ZnS, ZnSe and Au with observations and recommendations to make future attempts more successful. Finally, in the Conclusions and Future Work chapter, the findings of this work will be summarized and suggestions for future work will be made in an attempt to guide others who will continue this work.

I.C. Relevancy of Work

In the mid 1970s efforts were made to develop hollow waveguides (HWs) as devices for transmitting infrared radiation. The need for an alternative to solid core silica fibers arose because the silica fibers cannot transmit in the infrared region due to the absorption behavior of silica.[1]

Hollow waveguides have several features that make them more suitable for some applications. The fact that the core of the hollow waveguide is air is ideal for

transmitting high power laser beams because air has a higher damage threshold than the materials typically used in these waveguides.[1] In addition, nonlinear material absorptions are less important because only very thin films are deposited, therefore, very little material is present.[2] Also, there is little interaction between the light and these materials. The most notable and attractive attribute of these devices is that the performance can be optimized for a specific wavelength over a broad range of wavelengths in the IR, up to 20 μm . This is achieved by designing a waveguide (WG) with dielectric layers of appropriate thickness. The wavelength of low absorbance is ultimately determined by thin film effects. Low insertion loss, small beam divergence and the absence of end reflections make these waveguides more efficient than the more traditional, solid core fibers. [1]

Today infrared light has applications in diverse areas including chemical sensing [6, 12, 18], remote temperature measurement [12-15], medicine and dentistry [3-5, 7-11, 16, 17, 19-22, 25] and metals processing [23,24]. In all of these applications, the IR radiation must be transmitted from the source location to another location where it can be detected or used. Hollow waveguides are the most efficient devices for this function. For metals processing, the CO_2 and Nd:YAG (1.06 μm) lasers are used. Two commonly used wavelengths in medicine and dentistry are 2.94 μm , emitted by the Er:YAG laser and 10.6 μm , emitted by the CO_2 laser. These two wavelengths have become prominent because tissues are highly absorbing at these wavelengths. Therefore, making incisions and ablating tissue can be easily done with these lasers. It is noteworthy that there is minimal damage to surrounding tissue. Pulsed lasers and small inner diameter WGs or

WGs that include focusing elements ensure only the target tissue interacts with the laser beam. For most medical and industrial applications, transmission of 100 watts or less is sufficient; however for metals processing, i.e. cutting and welding, transmission of a few kilowatts is necessary.

In our group we have developed a process for producing single layer and multilayer waveguides that are rugged and stable for long term usage and storage. The materials used in making these waveguides are not reactive with water, and have high melting temperatures.[26] Circular, opposed to rectangular waveguides, glass waveguides with inner diameters of one millimeter or less have sufficient flexibility to be well suited for medical applications in which small, easily handled fibers that require bending are needed. In addition, these devices are appropriate in industrial applications where they will be permanently bent.[1]

A comparison between HWs and solid core silica fibers would show that hollow waveguides are inferior in several aspects. They are mechanically weaker; have an increase in loss when bent; have a small numerical aperture; and, in general, higher transmission losses. Therefore, these waveguides are typically only a few meters in length with the lowest loss being approximately 0.1 dB/m but with transmitted powers as high as 3 kW.[1,27-29]. These fibers have remained a topic of research for more than thirty years because they are capable of transmitting light in the infrared region, where silica cannot be used. [1]

I.D. Classification of Hollow Waveguide Types

There are two distinct types of hollow core waveguides. One type uses attenuated total reflection (ATR) to guide light and operates very similarly to solid core silica fibers. The structure of an ATR WG is somewhat analogous to the familiar solid core fiber with air as the core material surrounded by a cladding material of a lower index of refraction. Since air has an index of refraction of one, the cladding material of an ATR waveguide must have an index of refraction less than one at some technologically important wavelength. This low index of refraction is achieved in the region of anomalous dispersion. It is usually accompanied by high absorption due to large extinction coefficients, κ . The high absorption that is common in the region of anomalous dispersion makes this type of waveguide more absorbing than other hollow waveguides. ATR WGs are not the subject of significant research interest. There are important differences between the ATR guides and solid core fibers: the outer diameter of the waveguide is 3 to 10 times greater than the fiber and the core/clad diameter ratio is not the same as with solid core fibers. One example of an ATR WG, is the hollow sapphire waveguide (HSW). This material is an ideal candidate because it has a region of anomalous dispersion ($n < 1$) in the 10 to 16.7 μm wavelength range – which includes the wavelength where the commonly used the CO_2 laser operates. In addition, this material can be grown as a tube and it shows relatively low loss.[30,31] Most importantly, the κ value is 0.05 at 10.6 μm .[1] Absorption values of this order of magnitude have been shown to significantly influence the performance of a waveguide and the material is considered transparent with respect to the propagating radiation.

In the other type of waveguide, the so called leaky type, materials with indices greater than one surround the air core. Light is propagated by reflection off the inner surfaces as it travels down the waveguide. The inner surface is first coated with a metallic layer that is highly reflecting in the IR. One or multiple dielectric layers are deposited on the metal to minimize the reflection loss at the interfaces and on bending.[1,42,43] The substrate tubing can be plastic, glass or metal. All of the samples described in this dissertation are leaky type waveguides with silica substrate tubing. In comparison to the ATR type, these waveguides can be more efficient because the dielectric materials do not usually have high absorption values in the wavelength range of interest. In theory, the loss can also be continually decreased, in theory, with the addition of more dielectric layers or the use of larger inner diameters or both.[1] In addition, these waveguides can be formed using our low cost, efficient electroless chemical deposition process.

I.E. Fundamentals of Multilayer HWs

Hollow cylindrical leaky type waveguides propagate light by reflection just like a normal mirror. To produce a WG that is able to efficiently transmit at one or more specific wavelengths, reflection at that wavelength is maximized by depositing one or more dielectric layers with the correct optical thickness for enhanced reflection. These layers create interfaces from which multiple reflections occur. The phase shift of the waves is 180° when going from lower index of refraction to a higher refractive index layer. The calculated thickness of the topmost layer (adjacent to the air core) also takes into account the phase shift. Thus, these waves constructively interfere to produce greater reflection,

at regularly spaced wavelengths, than is possible from the silver surface alone. Thus, a thin film interference pattern is created. [32-34]

The parameters most commonly used to characterize the performance of HWs are straight transmission loss, loss on bending. As will be developed mathematically in the next chapter the total loss, for either single or multilayer WGs made with any metallic and dielectric materials, has three contributions: straight loss, α_{∞} , bending loss, α_{bend} and surface roughness, α_{surface} . The loss on bending is an additional contribution that is added to the loss measured when the WG is straight. The straight loss is directly dependent on the square of the wavelength of operation, and the mode(s) being propagated. It is inversely dependent on the cube of the bore radius. Surface roughness and film thickness variation are processing related parameters which contribute to the measured loss.[33,35] Equations I.1-3 give the dependence of the total loss on bending, core size, wavelength of operation, optical characteristics of the reflective metal layer, the individual dielectric layers, surface roughness, and index contrast between the dielectrics. [1,44]

$$\alpha_{\text{total}} = \alpha_{\infty} + \alpha_{\text{bend}} + \alpha_{\text{surface}} \quad (\text{I.1})$$

where

$$\alpha_{\infty} = \left(\frac{U_{nm}}{2\pi} \right)^2 \left(\frac{\lambda^2}{a^3} \right) \left(\frac{n_{Ag}^2}{n_{Ag}^2 + \kappa_{Ag}^2} \right) * F_{\text{film}} \quad (\text{I.2})$$

$$\alpha_{\text{bend}} \propto \frac{a^3}{R}$$

$$\alpha_{\text{surface}} \propto (\sigma/\lambda)^2$$

and U_{nm} is a parameter that is determined by the mode being propagated.

For the first contribution to the total loss, straight loss denoted by α_{so} , U_{nm} is a parameter determined by the propagating mode; λ is the wavelength of interest, [μm]; a is the inner radius [μm]; n_{Ag} is the real part of the index of refraction for silver layer at λ ; κ_{Ag} is the extinction coefficient for silver layer at λ ; F_{film} is the contribution to the loss from the dielectric layer. Most calculations of F_{film} are made using only the real part of the index of refraction and do not include the absorption in the calculation (as shown below).

For a single dielectric layer,

$$F_{film} = \frac{1}{2} \left(1 + \frac{n_{low}^2}{\sqrt{(n_{low}^2 - 1)}} \right)^2 \quad (I.3)$$

and for a multilayer dielectric stack, the

$$F_{film} \propto \left[1 + \frac{n_{low}^2}{(n_{low}^2 - 1)^{1/2}} \left(\frac{n_{low}}{n_{high}} \right)^{2mp} C^{-m_p} \right] \quad (I.4)$$

where n_{low} is the index of refraction of the low index material and n_{high} is the index of refraction of the high index material. $C = (n_{low}^2 - 1)/(n_{high}^2 - 1)$ where m_p is the number of pairs of low and high index dielectric layers.

For the bending loss, α_{bend} , the approximation is appropriate when the bending radius, R , is much greater than the inner core radius. The third contribution is the loss due to

surface roughness of the film denoted by α_{surface} . Note the strong increase in loss with surface roughness, σ , as shown for this term in the second line of Equation I.2. The roughness from all layers contributes to the final roughness.

Dielectric materials are chosen based on optical properties, and ease of deposition. Pairs of dielectrics are chosen with high index contrast.

In addition to the dependence of loss on the size of the core given in Eq. I.2, the shape of the core and the symmetry of the mode of propagation directly determine the loss in hollow waveguides. The explicit loss dependence on the bore size and cross-sectional geometry (circular or rectangular) is due to the fact that the core is assumed to be essentially lossless as the loss is due mainly to the thin films. Specifically, it is the material absorption, the deviation from the optimized thickness, and surface roughness of each layer that increases the loss. The spatial distribution of the electric field energy within the circular core varies for the different modes of radiation. The ideal distribution would have a zero energy density at the waveguide wall so that there would be a minimal amount absorption by the wall material. The HE_{11} mode has a distribution in which most of the energy is concentrated in the center of the core with less at the waveguide wall. The energy distributions for the first five modes, for which HE_{11} is the lowest loss mode, will be further discussed in Chapter II. [36]

Surface roughness increases with increased deposition time (thicker layers) and with an increasing number of layers. Thus, for multilayer coatings, surface roughness becomes a

more significant consideration because each additional layer follows the existing surface topography and adds its own roughness. Greater surface roughness of the layer in contact with the air core also means increased scattering which can be significant at shorter wavelengths. Non-uniform film thickness also increases the loss. The appropriate dielectric layer thickness for a given wavelength, λ_{opt} , in a single dielectric layer waveguide is calculated using the equation: [1,35]

$$d = \frac{\lambda_{opt}}{2\pi\sqrt{(n_d^2 - 1)}} \tan^{-1} \left[\frac{n_d}{(n_d^2 - 1)^{1/4}} \right] \quad (I.5)$$

where d is the physical thickness of the layer being considered [μm]; λ_{opt} is the wavelength [μm] for which the waveguide design is optimized; n_d is the real part of the index of refraction of the dielectric layer being considered at λ_{opt} .

I.F. Deposition Process

Thin film coating can be accomplished using a number of techniques including pyrolysis, sputtering, evaporation and chemical deposition. All of the samples used in this project were made using a wet chemistry, electroless process to deposit all of the layers, as shown in Figure I.1. This process has been used for some time in this group and is referred to as the Dynamic Liquid Phase Deposition (DLPD) method.[37] Another common, similar deposition process that is also relatively easy is the electroless method called chemical bath deposition (CBD). CBD is another process used to coat large surface area pieces. Often the chemical reactions and the precursor salts used in CBD are

also used in DLPD. The deposition times for the two methods are often similar. In addition, the resultant films have similar microstructures.

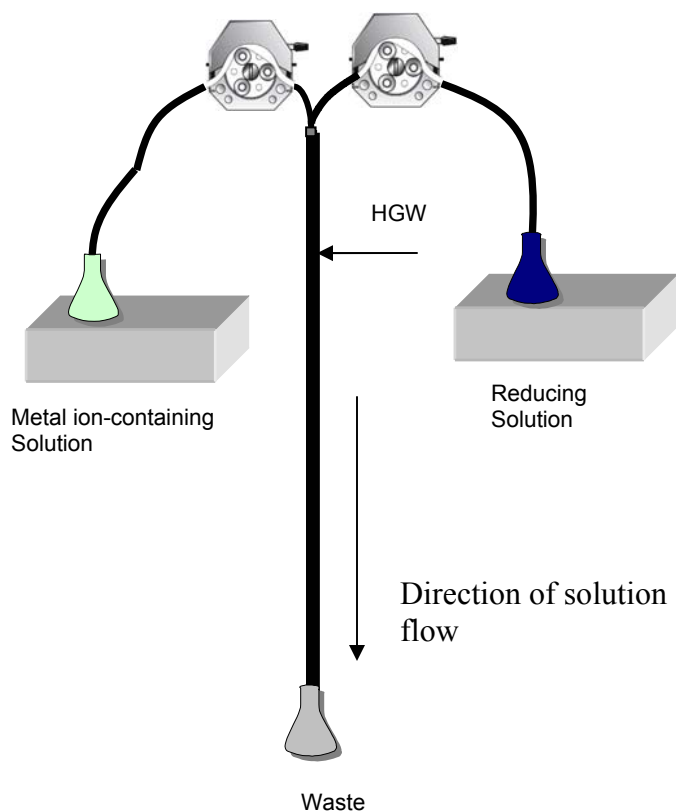
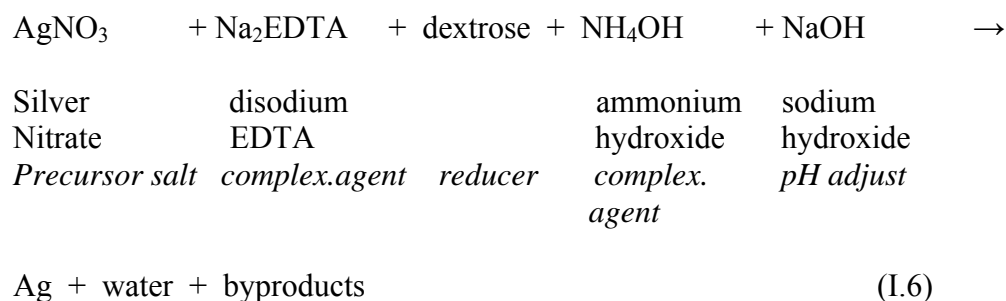


Figure I.1 A schematic of the electroless Dynamic Liquid Deposition Process (DLPD).[37] The metal ion containing solution could contain silver ions (Ag^{1+}), cadmium ions (Cd^{2+}) or lead ions (Pb^{2+}). The reducing solution would contain a dextrose solution if silver were being deposited. If CdS or PbS were being deposited, the reducing solution would be a solution containing the anion (sulfur) portion of the compound.

In both processes, a precursor salt serves as a source of the metal to be deposited. Once the precursor is dissolved in water, the salt yields the metal as a cation. Additional precursors supply reducing species or anions. When these species are mixed in solution, chemical reactions between them form dielectric compounds. Other additives may be added to the solution to control the reaction rate between the cations and the anions or reducers. These additives are either complexing agents or agents for adjusting the pH level of the solution. In the presence of the ionic species, the complexing agents form bonds creating new species called complexes. The complexes dissociate at a rate that is determined by solution characteristics such as temperature, pH, and concentration of each species.

A typical bath composition, used for the common process of silvering a glass surface via CBD or DLDP is:



There are a few significant differences between CBD and DLDP that make the latter process distinctly more appropriate for producing optical coatings. First, there are two separate starting solutions for deposition that require chemical reactions. One solution contains the cations and the other contains the anions. If the DLDP process were used to deposit silver, the Ag precursor salt, ammonium hydroxide, and pH adjuster would be in

one solution and the other complexing agent (Na_2EDTA) and the reducer would be in the other solution. The solutions would be mixed at a rate to control when the reaction begins. Second, the concentrations of the starting solutions are more dilute than the CBD deposition, which allows the growth of each layer to be carefully controlled because the kinetics are well understood and on a time scale that allows thickness to be determined on a nanometer level. Third, in DLPD, the solutions are not mixed until immediately before they are brought into contact with the surface to be coated, which minimizes the surface/reacted solution interaction time. Fourth, they are kept in constant motion because they are being pumped from the flask through the substrate tubing to the waste container. This constant motion ensures adequate mixing. In addition, the constant motion decreases the likelihood that undesirable contaminants such as waste products and individual particles remain on the surface or are imbedded in the layer which would increase surface roughness and possibly reduce adhesion. The individual particles form in solution when there is homogeneous nucleation rather than the desired heterogeneous nucleation.[37-41]

For deposition of Ag, Au, CdS, PbS and the Zn compounds there is a chemical reaction occurring. In these cases deposition time, quality of mixing of the reactants and rate of reaction are the important parameters. For the polymer deposition there is no chemical reaction occurring. For all depositions pump speed and concentration of precursor solutions are important.

The first layer deposited is usually Ag. The Ag layer is then overcoated with a dielectric layer of controlled thickness. Another dielectric layer may be deposited upon the first, and this second layer will have a higher index of refraction than the first dielectric material. The process of depositing a low and then a high index dielectric material can be repeated and in this way a multilayer dielectric is formed on the Ag layer. A cross-sectional schematic of the final multilayer hollow waveguide is shown in Figure I.2. Characterization of the films was done primarily using Fourier Transform Infrared (FTIR) spectroscopy. Calculations of film thickness were based solely on the FTIR spectra because SEM imaging has shown that peaks in the FTIR spectra accurately indicate layer thickness.[37,45] Therefore the FTIR results are reliable. The physical thickness was calculated using:

$$d = \frac{m\lambda^{(m)}}{4 * \sqrt{n_d^2 - 1}} \quad (I.7)$$

In Equation I.7, the superscript m is an ordinal label and not an exponent. The first or primary wavelength (for which m=1) is the longest wavelength at which a peak occurs. The wavelength of lowest loss was also finally determined by examining the interference pattern of the FTIR spectrum.

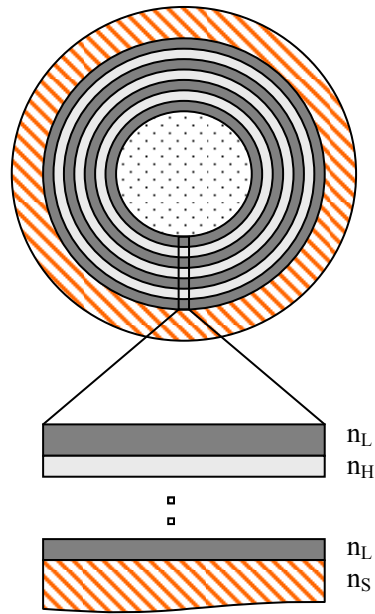


Figure I.2 A cross-sectional schematic of a multi-layer hollow waveguide. The outermost ring, which corresponds to the bottom layer in the lower section of the figure, is silver. The darker rings and layers are the low index material. The lighter rings and layers are the high index material. The center is the air core.

REFERENCES

1. Harrington, J.A., *Infrared Fibers and Their Applications*, SPIE Press, Washington, 2004.
2. Matsuura, Y., Tsuchiuchi, A., Noguchi, H., and Miyagi, M., "Hollow fiber optics with improved durability for high-peak-power pulses of Q-switched Nd:YAG lasers," *Appl. Opt.* **46**(8), pp.1279-1282 (2007).
3. Nemec, M., Jelinkova, H., Kornada, P., et al., "Medical application of 3 μ m delivery waveguide system," *Proc. SPIE* Vol. 6083, pp.60830M1-9 (2006).
4. Fried, D., Zuerlein, M., Featherstone, J.D.B., et al., "IR laser ablation of dental enamel: mechanistic dependence on primary absorber," *Appl. Surf. Sci.* **127-129**, pp. 852-856 (1998).
5. Nakazawa, M., Shi, Y.W., Matsuura, Y., "Hollow polycarbonate fiber for Er:YAG laser light delivery," *Opt. Lett.* **31**(10), pp. 1373-1375 (2006).
6. Haan, D., Harrington, J.A., "Hollow waveguides for gas sensing and near-IR applications," *Proc. SPIE*. Vol. 3596, pp. 43-48 (1999).
7. Jelinkova, H., Nemec, M., Kornada, P., et al., "Compact hollow glass waveguide system for Er:YAG laser radiation," *Proc. SPIE* Vol. 5691, pp. 192-199 (2005).
8. Dostlova, T., Jelinkova, H., Miyagi, M., et al., "Contact and non-contact laser preparation of hard dental tissues by Er:YAG laser radiation delivered by hollow glass waveguide or articulated arm," *Proc. SPIE* Vol. 3593, p. 211 (1999).
9. Dostlova, T., Jelinkova, H., Nemec, M., et al., "Er:YAG laser micro-preparation of hard dental tissue," *Proc. SPIE* Vol. 6425, pp.64250G1 (2007).
10. Kornada, P., Jelinkova, H., Nemec, M., et al., "Er:YAG laser radiation for soft and hard urological tissue treatment," *Proc. SPIE* Vol. 6078, p. 60781E1 (2006).
11. Nemec, M., Kornada, P., Jelinkova, H., et al., "Application of hollow glass waveguides in urological treatment," *Proc. SPIE* Vol. 5691, p. 183 (2005).
12. Matsuura, K., Matsuura, Y., Harrington, J.A., "Evaluation of gold, silver, and dielectric-coated hollow glass waveguides," *Opt. Eng.* **35**(12) pp. 3418-3421 (1996).
13. Dekel, B., Inberg, A., Croitoru, N., "Fiber optic thermal imaging system based on hollow glass waveguides or silver halide fibers as scanning elements," *Opt. Eng.* **39**(4), pp. 941-946 (2000).

14. Markham, J.R., Kinsella, K., "Thermal Radiative Properties and Temperature Measurement from Turbine Coatings," *International Journal of Thermophysics* **19**(2), pp.537-545 (1998).
15. Sagesse, S.J., Harrington, J.A., Sigel, G.H., "Hollow sapphire waveguides for remote radiometric temperature measurements," *Electron. Lett.* **27**(9), pp.707-709 (1991).
16. Kozodoy, R.L., Zazanis, G.A., Schwarz, K.O., et al., "A hollow sapphire waveguide for stereotactic intraventricular CO₂ laser neurosurgery: a rat model," *Lasers in Medical Science* **9**(4), pp.273-281 (1994).
17. Michel, J-L., Grogard, C., Toubel, G., et al., "CO₂, Er:YAG and Pulsed Dye Laser Treatment of Angiofibromas in Patients with Tuberous Sclerosis", *Medical Laser Application* **19**(3), 136-145, 2004.
18. Kozodoy, R.L., Micheels, R.H., Harrington, J.A., "Small-bore hollow waveguide infrared absorption cells for gas sensing," *Appl. Spec.* **50**(3), pp.415-417 (1996).
19. Lanzafame, R.J., "Laser use and research in gastroenterology, gynecology, and general surgery: A status report," *Journal of Clinical Laser Medicine and Surgery* **19**(3), pp. 133-140 (2001).
20. Tanzi, E.L., Lupton, J.R., Alster, T.S., "Lasers in dermatology: Four decades of progress," *Journal of the American Academy of Dermatology* **49**(1), pp. 1-31 (2003).
21. Duclos, D., "Lasers in veterinary dermatology," *Veterinary Clinics of North America –Small Animal Practice* **36**(1), p.15 (2006).
22. Hantash, B.M., Stewart, D.B., Cooper, Z.A., et al., "Facial resurfacing for nonmelanoma skin cancer prophylaxis," *Archives of Dermatology* **142**(8), pp. 976-982 (2006).
23. Matsuura, Y., Oyama, T., Miyagi, M., "Soft-x-ray hollow fiber optics with inner metal coating," *Appl. Opt.* **44**(29), pp.6193-6196 (2005).
24. Berretta, J.R., de Rossi, W., das Neves, M.D.M., et al., "Pulsed Nd:YAG laser welding of AISI 304 to AISI 420 stainless steels," *Optics and Lasers in Engineering* **45**, pp.960-966 (2007).
25. Jelinkova, H., Nemec, M, Sulc, J., et al., "Hollow waveguide delivery systems for laser technological application," *Progress in Quantum Electronics* **28**, pp.145-164 (2004).
26. Lide, D.R., CRC Handbook of Chemistry and Physics, 2002-2003.

27. Jelinkova, H., Miyagi, M., Sulc, J., et al, "Delivery of high-powered picosecond pulses in near-IR region by special silver hollow glass waveguides," *Proc. SPIE* Vol. 3596, pp. 32-42 (1999).
28. Honga, A., Morosawa, K., Siota, T., et al. "Transmission of 1kW-class CO₂ laser light through circular hollow waveguides for material processing," *Appl. Phys. Lett.* **58**(15), pp.1582-1584 (1991).
29. Honga, A., Morosawa, K., Siota, T., et al. "Transmission of 1kW-class CO₂ laser light through circular hollow waveguides for material processing," *Appl. Opt.* **31**(24), pp. 5114-5120 (1992).
30. Gregory, C.C., Harrington, J.A., "High peak power CO₂ laser transmission by hollow sapphire waveguides," *Appl. Opt.* **32**(21), pp.3978-3980 (1993).
31. Nubling, R.K., Harrington, J.A., "Hollow-waveguide delivery systems for high-power, industrial CO₂ lasers," *Appl. Opt.* **34**(3), pp.372-380(1996).
32. Matsuura, Y., Hongo, a., Miyagi, M., "Dielectric-coated metallic hollow waveguide for 3 μ m Er:YAG, 5 μ m CO, and 10.6 μ m CO₂ laser light transmission," *Appl. Opt.* **29**(15), pp.2213-2218 (1990).
33. Shi, Y.W., Ito, K., Matsuura, Y., et al., "Multiwavelength laser light transmission of hollow optical fiber from the visible to the mid-infrared," *Opt. Lett.* **30**(21), pp.2867-2869 (2005).
34. Hecht, E., *Optics*, Addison-Wesley, New York, 1998, pp.418-423.
35. Rabii, C., Gibson, D., Harrington, J.A., "Processing and characterization of silver films used to fabricate hollow glass waveguides," *Appl. Opt.* **38**(21), pp. 4486-4493 (1999).
36. Edited by Sanghera, J.S. and Aggarwal, I.D., *Infrared Fiber Optics*, CRC Press, New York, 1998.
37. Gopal, Veena, New Dielectric Coatings for Low-Loss Hollow Glass Waveguides and Bundles, Rutgers University thesis, 2003.
38. Grozdanov, I., Najdoski, M., Dey, S.K., "A simple solution growth technique for PbSe thin films," *Mat. Lett.* **38**, pp.28-32 (1999).
39. Grozdanov, I., "A simple and low-cost technique for electroless deposition of chalcogenide thin films," *Semicond. Sci. Technol* **9**, pp.1234-1241 (1994).

40. Kainthla, R.C., Pandya, D.K., Chopra, K.L., "Solution growth of CdSe and PbSe films," *J. Electrochem. Soc.: Electrochemical Science and Technology* **127**(2), pp. 277-283 (1980).
41. Nair, P.K., Nair, M.T.S., Garcia, V.M., et al. "Semiconductor thin films by chemical bath deposition for solar energy related applications," *Solar Energy Materials and Solar Cells* **52**(3-4), pp. 313-344 (1998).
42. Croitoru, N., Dror, J., Gannot, I., "Characterization of hollow fibers for the transmission of infrared radiation," *Appl. Opt.* **29**(12), pp.1805-1809 (1990).
43. Miyagi, M., Hongo, A., Aizawa, Y., Kawakami, S., "Fabrication of germanium-coated nickel hollow waveguides for infrared transmission," *Appl. Phys. Lett.* **43**(5), pp.430-432 (1983).
44. Miyagi, Kawakami, S., "Design Theory of Dielectric-Coated Circular Metallic Waveguides for Infrared Transmission," *J Lightwave Tech.* **LT-2**(2), pp.116-126 (1984).
45. Alaluf, M., Dror, J., Dahan, R., Croitoru, N., "Plastic hollow fibers as a selective infrared radiation transmitting medium," *J Appl. Phys.* **72**(9), pp.3878-3883 (1992).

Chapter II Theory

II.A. General

In 1964, Marcatili and Schmeltzer (MS) were the first to attempt to fully describe mathematically the transmission of IR radiation within hollow circular waveguides. Their work is far reaching in its scope.[1,2] Prior to their publication, only the transmission of microwave frequencies in HWs had been thoroughly detailed. The second seminal source by Miyagi and Kawakami [1,3] was published 20 years later after it was shown that HWs were truly a viable option because bending does not severely decrease transmission as stated by MS. Their conclusions are the basis of the current understanding of behavior of WGs on bending. Further encouraging the development of HW was the potential to replace the unwieldy and complicated articulated arm mirror system for directing IR radiation. Miyagi and Kawakami's work was particularly relevant because they also developed a mathematical basis for understanding the loss reduction of the HE_{11} mode using a dielectric-coated metallic WG. Many commonly available lasers emit light with a TEM_{00} mode which couples to the propagating mode of hollow waveguides, the HE_{11} mode. The TE_{01} mode is the propagation mode of lowest loss in metal-only WGs, while HE_{11} is the lowest loss mode propagating in dielectric coated leaky type WGs.

Other topics that will be discussed in this chapter are the effect of surface roughness on WG performance, efficient coupling of radiation into HWs for loss measurements, and low loss single mode transmission. Finally the relevant parameters of the polymeric dielectric, PS, will be discussed. It is necessary to consider the properties of PS

separately because this material is so unlike the metal sulfides and metal selenides dielectrics that are commonly used.

II.B. MS Theory

MS [2] developed a theoretical understanding of IR transmission in both metallic and dielectric cylindrical HWs. Their effort on metallic WGs was motivated by the fact that the reflecting metal cannot be described as a conductor in the IR, as it can be at microwave frequencies. They began describing the material using the complex refractive index which takes into account the large dielectric constant at optical frequencies. MS found that the large dielectric constants made the metallic WGs much more able to withstand bending without significant transmission loss.

II.B.1. MS Theory for Straight Loss

MS began with two assumptions to simplify the calculations and more realistically describe the transmission behavior.

The first assumption is:

$$ka = 2\pi a / \lambda \gg (v)(U_{nm}) \quad (\text{II.1})$$

where k = free-space dielectric constant $= 2\pi / \lambda$

a = inner radius of waveguide

v = complex index of refraction of the metallic reflector (has the form, $n - j\kappa$)

$U_{nm} = m^{\text{th}}$ root of the Bessel function $J_{n-1}(U_{nm}) = 0$

This expression ensures the wavelength is much smaller than the internal radius of the tube and therefore essentially all of the propagating energy is contained within the tube and strikes the walls at grazing angles so that there is minimal reflection loss. This approximation is not realistic because the absolute value of the complex index is actually quite large since commonly used metals have large extinction coefficients.[1] MS found dielectric HWs, which do not have such large complex indices, were not as promising for transmission over long distances.

The second assumption is:

$$|(\gamma/k)-1| \ll 1 \quad (\text{II.2})$$

where γ = the axial propagation constant of the mode being considered.

$$\gamma = k \left[1 - \frac{1}{2} \left(\frac{U_{nm} \lambda}{2\pi a} \right)^2 \left(1 - \frac{i v_n \lambda}{\pi a} \right) \right] \quad (\text{II.2a})$$

This expression ensures only low loss modes, which have propagation constants approximately equal to that of the free space propagation constant, k , are considered.

It is accepted that all modes (transverse electric (TE), transverse magnetic (TM), hybrid modes) can be propagated within the WG. A schematic of a waveguide with all of the pertinent parameters is shown in Figure II.1.

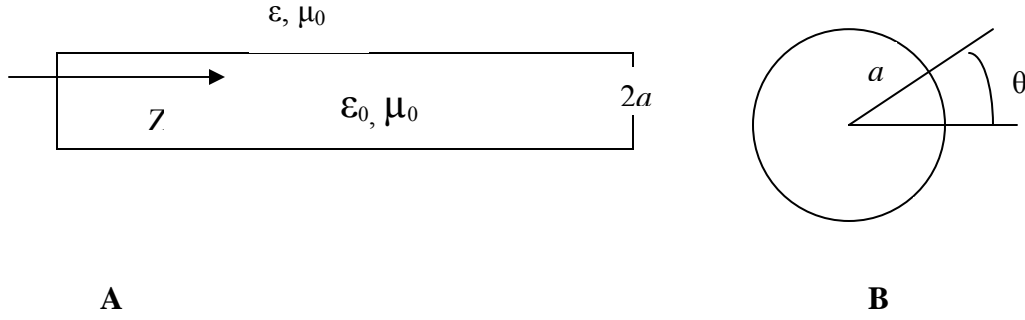


Figure II.1 A) The planar view of a hollow waveguide of diameter $2a$ and B) the cross sectional view. In (B), the z direction is coming out of the plan of the paper. The radiation propagates along the optical axis of the waveguide, or in the z direction.

The complex propagation constant, γ , satisfies these relationships

$$k_i^2 = k^2 - \gamma^2 \quad (\text{II.3})$$

$$k_e^2 = v^2 k^2 - \gamma^2 \quad (\text{II.4})$$

The superscript i indicates the fields within the core of the waveguide. The superscript e indicates the external fields within the substrate tube of the waveguide. Both were considered by MS.

Simplified mathematical expressions for the electric and magnetic fields are given below. Only the expressions for the hybrid modes being transmitted in the WG are given. The internal ($r < a$) modes are the only ones considered because assumption 1 says the energy is confined to the core. HE_{11} (a hybrid mode) is the lowest loss mode for dielectric coated leaky type HGWs studied in this project. The field equations are included to clarify some of the relations used in the different stages of the derivation of the

expressions for the attenuation constant and to demonstrate the relationship between the different equations. Using substitutions for γ and neglecting (λ/a) terms of powers greater than one, the following equations are obtained:

Hybrid Modes ($n \neq 0$, there is some angular dependence)

$$E_{\theta nm}^i = - \sqrt{\frac{\mu_0}{\epsilon_0}} H_{rnm}^i = J_{n-1}(U_{nm} \frac{r}{a}) * \cos n\theta \quad (\text{II.5})$$

$$E_{rnm}^i = \sqrt{\frac{\mu_0}{\epsilon_0}} H_{\theta nm}^i = J_{n-1}(U_{nm} \frac{r}{a}) * \sin n\theta \quad (\text{II.6})$$

$$E_{znm}^i = -i \frac{U_{nm}}{ka} * J_n(k_r r) * \sin n(\theta + \theta_0) \quad (\text{II.7})$$

$$H_{\theta nm}^i = \sqrt{\frac{\epsilon_0}{\mu_0}} E_{rnm}^i \quad (\text{II.8})$$

$$H_{rnm}^i = - \sqrt{\frac{\epsilon_0}{\mu_0}} E_{\theta nm}^i \quad (\text{II.9})$$

$$H_{znm}^i = - \sqrt{\frac{\epsilon_0}{\mu_0}} E_{znm}^i \tan n(\theta + \theta_0)$$

(II.10)

In these expressions, n is the angular index, and m is the radial index.

To obtain the propagation constant of each mode, the characteristic equation for a general circular cylinder must be considered. The propagation constants are the roots to this equation. A simplified form of the characteristic equation is:

$$J_{n-1}(k_i a) = i v_n (k_i/k) * J_n(k_i a) \quad (\text{II.11})$$

$$\text{where } v_n = \frac{1}{2} \frac{(\nu^2 - 1)}{\sqrt{\nu^2 - 1}}, \text{ for hybrid modes } (n \neq 0) \quad (\text{II.12})$$

v_n is the complex index for a given mode. From this form of the characteristic equation, the propagation constant can be determined. The attenuation constant can be obtained once the propagation constant is known. The right side of the simplified characteristic equation is approximately zero when the expressions for k_e and k_i and the first assumption are taken into account. The $k_i a$ term can be approximated using only the first term from the perturbation technique with the following result:

$$k_i a \approx U_{nm} (1 - i v_n / k a). \quad (\text{II.13})$$

Hence

$$\gamma \approx k \left[1 - \frac{1}{2} \left(\frac{U_{nm} \lambda}{2 \pi a} \right)^2 \left(1 - \frac{i v_n \lambda}{\pi a} \right) \right] \quad (\text{II.14})$$

The phase constant of each mode is the real part of γ :

$$\beta_{nm} = \text{Re}(\gamma) = \frac{2\pi}{\lambda} \left\{ 1 - \frac{1}{2} \left(\frac{U_{nm} \lambda}{2 \pi a} \right)^2 * \left[1 + \text{Im} \left(\frac{v_n \lambda}{\pi a} \right) \right] \right\} \quad (\text{II.15})$$

The attenuation coefficient of each mode is the imaginary part of γ :

$$\alpha_{nm} = \text{Im}(\gamma) = \left(\frac{U_{nm}}{2\pi} \right)^2 \frac{\lambda^2}{a^3} \text{Re}(\nu_n). \quad (\text{II.16})$$

The next assumption in MS theory is that ν_n is usually real and independent of λ for dielectrics. The attenuation constant becomes:

$$\alpha_{nm} = \left(\frac{U_{nm}}{2\pi} \right)^2 \frac{\lambda^2}{a^3} * \frac{\frac{1}{2}(\nu^2 - 1)}{\sqrt{\nu^2 - 1}}, \text{ for HE}_{nm} \text{ modes (n} \neq 0) \quad (\text{II.17})$$

Power and intensity are the square of the fields so when converting from the calculated value, α_{nm} , to the measured value of straight loss α_{∞} with units of dB/m, the following conversion must be carried out:

$$\alpha = 2 * \alpha_{nm} \quad [\text{m}^{-1}] \quad (\text{II.18})$$

$$\alpha_{\infty} = 4.34 * \alpha \quad [\text{dB/m}] \quad (\text{II.19})$$

The value of α_{straight} is determined experimentally using the cutback method that is widely used for solid core fibers.

The first assumption mentioned at the beginning of the MS theory explanation was that the bore size is much greater than the wavelength. This would indicate that many modes

propagate in the waveguide. However, only a small number of modes actually propagate in a hollow waveguide. Many modes damp out because the loss is dependent on the square of the mode parameter, U_{nm} . Table II.1 gives the values of U_{nm} for some modes. It is clear from the table that U_{nm} increases rapidly for higher order modes (increasing values of n or m). Therefore, in practice, the HW does not propagate many higher order modes as calculated from MS theory. It can also be seen from Eq. II.2a that for a larger bore, more of the axial propagation constants of the modes traveling within the WG are closer in value to the free space propagation constant than for a smaller bore since the λ/a factor is smaller for larger bore sizes. As stated in the second assumption of MS theory (Eq. II.2), a small difference between the two propagation constant values means the modes will be low loss, and therefore, able to propagate down the WG.

Table II.1[1] Waveguide Mode Parameters, U_{nm}

U_{nm}	U_{n1}	U_{n2}	U_{n3}	U_{n4}
U_{1m}	2.405	5.52	8.654	11.796
$U_{(2 \text{ or } 0)m}$	3.832	7.016	10.173	13.324
U_{3m}	5.136	8.417	11.62	14.796
U_{4m}	6.380	9.761	13.015	16.223

Modes symmetries are shown below Figure II.2. Loss measurements with our leaky type dielectric coated WGs are made by propagating the HE_{11} mode. This mode is the lowest loss mode for these waveguides and it can be easily excited and strongly coupled to our WGS with our commercially available lasers.[1] Upon close inspection of Eq. II.12, it can be seen that the HE_{11} mode is the lowest loss mode when the complex index of refraction, $v < 2.02$. In general, 2.02 is a relatively low index for dielectrics, and having $v < 2.02$ is rare for an inorganic dielectric. Polymers have been studied for use in the single dielectric layer WGs because there are many that have indices less than 2.02. Low losses, comparable to those theoretically possible with single polymer layers, can also be achieved when higher index materials are used (in multilayers with low index materials to achieve high index contrast) and more layers are deposited.

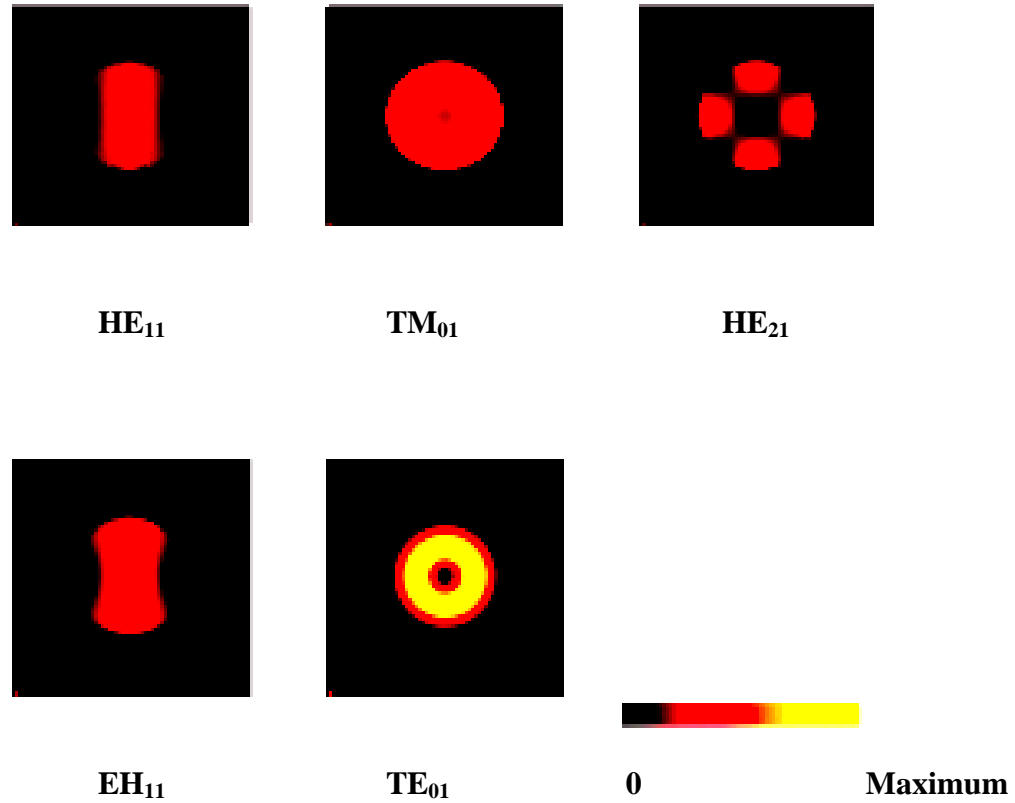


Figure II.2 [4] Electric field time average energy density for the first 5 modes as determined from a cross section of hollow waveguides. The color scale indicates intensity. Black indicates zero intensity and white indicates maximum intensity.

II.B.2. MS Theory for Bending Loss

MS considered the loss on bending in HWs that would be used for long distance transmission separately from the straight loss. Bending the WG makes the propagation different because the field configuration is changed from that in the straight WG. They determined that the loss on bending with a bending radius of 10 km would be double the straight loss. Thus the loss on bending would be so large that these devices were not viable options for long distance transmission.

Bending loss according to MS theory is given by:

$$\alpha_{nm}(R) = \alpha_{nm}(\infty) \left\{ \frac{4}{3} \left(\frac{2\pi a}{U_{nm} \lambda} \right)^4 \left(\frac{a}{R} \right)^2 * \left[1 - \frac{n(n-2)}{U_{nm}^2} + \frac{3}{4} \delta_n(\pm 1) \frac{\text{Re} \sqrt{v^2 - 1}}{\text{Re} \frac{v^2 - 1}{\sqrt{v^2 - 1}}} \cos 2\theta_0 \right] \right\} \quad (\text{II.20})$$

Their $1/R^2$ dependence is reproducible for the bending radii they tested. However most commonly, the waveguides are bent more tightly and a $1/R$ dependence is seen. To observe the $1/R$ dependence, the condition $R \gg a$ should not apply. This regime of operation is formally referred to as whispering gallery mode propagation. During whispering gallery propagation, the rays only make contact with one wall. The radii of curvature during bending loss measurements in this work are taken to be within the range of the whispering gallery propagation. Figure II.3 is a sketch of the two different types of propagation.

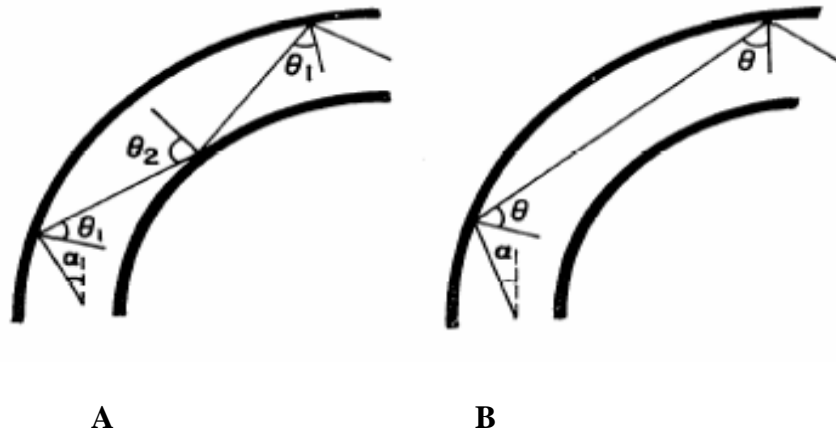


Figure II.3[5] The two types of ray paths and the angles: A) Normal propagation, and B) Whispering gallery mode propagation. Rays propagating down a straight waveguide bounce against both walls during normal propagation but only against one wall during whispering gallery propagation.

The wave optic approach used in MS theory develops from solving the characteristic equation. The attenuation coefficient calculated using MS theory is applied to straight loss exclusively since the bending loss calculations were made for very large radii of curvature that are not typical and the dependence on bending radius was found to be different for smaller, more practical radii.

II.C. Miyagi and Kawakami (MK) Theory

MK [3] discussed the loss behavior in terms of the surface impedance and admittance of the surface adjacent to the air core. According to MK, dielectrics materials are deposited

to change these values from those of the metallic layer. This approach is effective for deriving expressions for the loss and for the mode transitions seen in dielectric coated and uncoated metallic WGs.

II.C.1 MK Theory for Straight Loss

The basic assumptions in this derivation are the axial phase constant, β , can be approximated as $\beta \sim n_0 k_0$, and $n_0 k_0 a \gg 1$ for lower order modes. A planar view of a WG, with the axis of propagation labeled as z , and a cross sectional view are shown in Figure II.4.

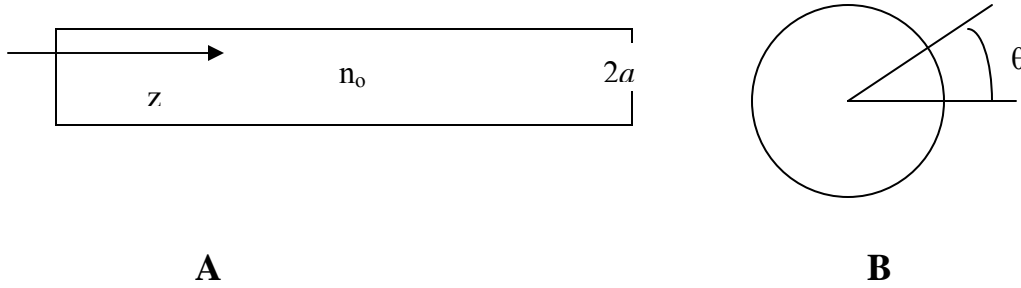


Figure II.4[3] A) The planar view of a hollow waveguide of diameter $2a$, and B) the cross sectional view.

MK have expressions for the electric and magnetic fields inside the walls of the WG (for $r \leq a$) and boundary conditions so that surface impedance, z_{TE} , and admittance, y_{TM} are defined by:

$$\left. \frac{E_\theta}{H_z} \right)_{r=R} = \frac{\omega \mu_0}{n_0 k_0} z_{TE} \quad (\text{II.21})$$

$$\left. \frac{H_\theta}{E_z} \right)_{r=R} = -\frac{n_0 k_0}{\omega \mu_0} y_{TM} \quad (\text{II.22})$$

where n_0 and k_0 are the refractive index of the waveguide and the free space propagation constant, respectively.

As in the MS theory section, the characteristic equation is shown. For the hybrid modes, in particular, the following form of the characteristic equation is the starting point for deriving the expression for the attenuation constant:

$$\frac{J_{n\mp 1}(u)}{u J_n(u)} = \mp j \frac{1}{2n_0 k_0 a} (z_{TE} + y_{TM}). \quad (\text{II.23})$$

Now this expression for the attenuation constant can be obtained:

$$\alpha_{\text{HEnm}} = \frac{1}{2} \frac{n_0 k_0 u_0^2}{(n_0 k_0 a)^3} \text{Re}(z_{TE} + y_{TM}) \quad \text{for } |y_{TM}| \ll y_0 \quad \text{and} \quad |z_{TE}| \ll z_0 \quad (\text{II.24})$$

II.C.2 MK Theory for minimizing attenuation of hybrid modes

To achieve the lowest possible loss for HE_{11} transmission, one or more dielectrics can be deposited on top of the metallic layer in order to make the admittance and impedance much smaller than that of the metal. A schematic of a multilayer is shown in Figure II.5. All of the conditions that MK theory sets forth (order of deposition, thickness of layers, thickness of the innermost layer, etc.) are shown in the schematic.

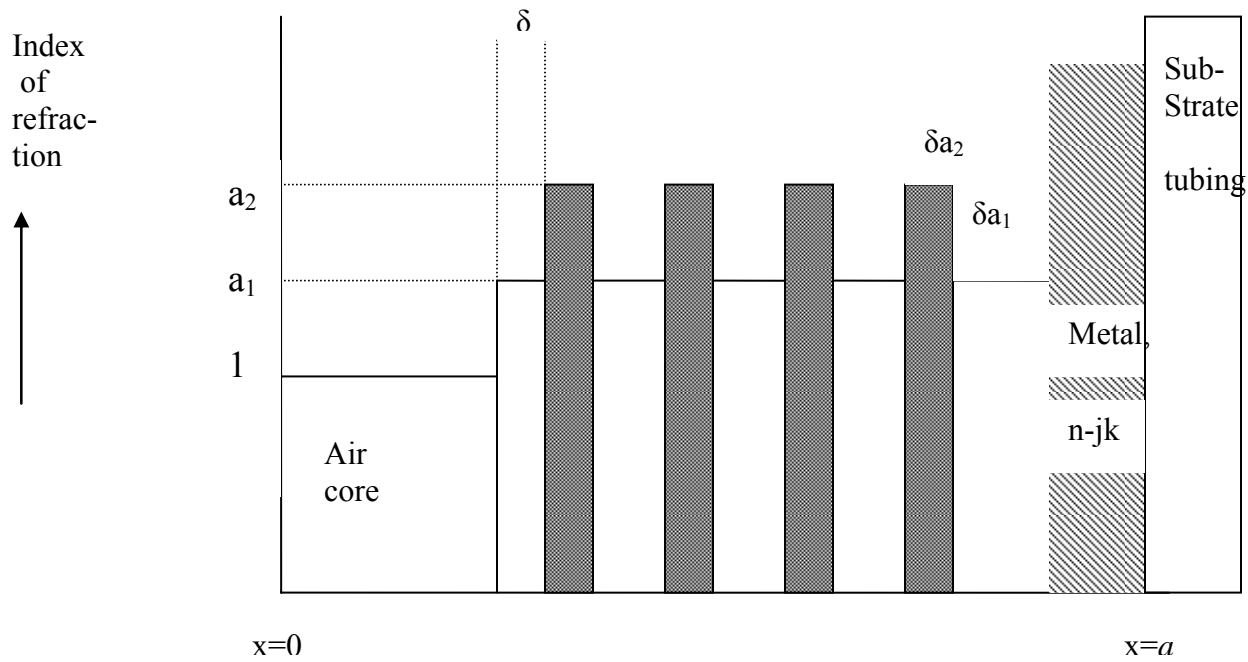


Figure II.5[3] A schematic of the waveguide structure from the centerline (at $x=0$) of the WG to the inner surface of the substrate tubing (at $x=a$). The inner radius of tubing is a . Since the physical dimension of the dielectric layer, $d=(\lambda*n)/4$, is dependent on the index of refraction of the material, the physical dimension differs for the two films as illustrated. Also, the layer adjacent to the air core is thinner than the other layers of the same material. The core is not to scale.

Equation II.24 can be expressed as:

$$\alpha_{\text{HEnm}} = \frac{n_0 k_0 u_0^2}{(n_0 k_0 a)^3} F, \quad (\text{II.25})$$

$$\text{where } F = \frac{1}{2} \text{Re}(z_{TE} + y_{TM}). \quad (\text{II.26})$$

F is called the figure of merit. When F is minimized it is denoted as F_{\min} .

Now the form of Equation II.25 that is commonly used to calculate straight loss will be obtained. If two non-absorbing ($\kappa < 10^{-2}$) dielectrics are deposited in alternating layers and have refractive indices, $a_i n_0$ ($i=1,2$), then the dielectric adjacent to the metal has an index of a_1 and it is the lower index material ($a_2 > a_1$). The thickness for each material is chosen so that this expression is satisfied:

$$(a_i^2 - 1)^{1/2} n_0 k_0 \delta_{ir} \equiv \delta_{iu_i} = \frac{\pi}{2}. \quad (\text{II.27})$$

Now the normalized impedance and admittance for each material can be expressed in terms of the index of refraction:

$$z_i = (a_i^2 - 1)^{-1/2} \quad (i=1,2) \quad (\text{II.28})$$

$$y_i = a_i^2 (a_i^2 - 1)^{-1/2} \quad (i=1,2) \quad (\text{II.29})$$

where we define C as:

$$C = (a_1^2 - 1) / (a_2^2 - 1) \quad (\text{II.30})$$

A guideline for choosing a suitable pair of dielectrics is the inequality,

$$C < 1 \quad (II.31)$$

The C term is included in the definition of the figure of merit, F (first seen in Eqs II.25 and 26), as shown in Eq. II.38b. Also from Eq. II.25, since the C term is part of the definition of F , it is also included in the final expression for the attenuation constant, α , when two dielectrics are included in the WG. The same expression is used whether the number of layers is even or odd. The goal of minimizing attenuation, and therefore C , is a basis for choosing a pair of dielectrics. The inequality in Equation II.31 must be true for the equation here to predict the WG performance. The quantity (a_2/a_1) will be called the index contrast for a pair of dielectrics in this dissertation.

When the total number of dielectric layers, m , is odd (given by $2m_p + 1$), the normalized impedance and admittance of the metal, $z_{TE}^{(0)}$ and $y_{TM}^{(0)}$, is changed. The new values are given by z_1 and y_1 and are defined at the new surface as follows:

$$z_1 = \left(\frac{z_2}{z_1} \right)^{2m_p} z_{TE}^{(0)} \approx \frac{n + j\kappa}{n^2 + \kappa^2} C^{m_p} \quad (II.32)$$

$$y_1 = \left(\frac{y_2}{y_1} \right)^{2m_p} y_{TM}^{(0)} \approx (n - j\kappa) \left(\frac{a_2}{a_1} \right)^{4m_p} C^{m_p} \quad (II.33)$$

where the original impedance ($z_{TE}^{(0)}$) and admittance ($y_{TM}^{(0)}$) of the metal, respectively are:

$$z_{TE}^{(0)} = [(n-j\kappa)^2 - 1]^{-1/2} \approx (n-j\kappa)^{-1} \quad (II.34)$$

$$y_{TM}^{(0)} = \{n-j\kappa\}^2 z_{TE}^{(0)} \approx n-j\kappa. \quad (II.35)$$

The attenuation coefficient of the hybrid modes for a dielectric coated WG has a minimum value when the dielectric layer thicknesses, $\delta_i r$, satisfy:

$$(a_1^2 - 1)^{1/2} n_0 k_0 \delta_i r = \pm \tan^{-1} \left[\frac{a_1}{(a_1^2 - 1)^{1/4}} \left(\frac{a_1}{a_2} \right)^{m_p} C^{-m_p / 2} \right]. \quad (II.36)$$

At these optimal thicknesses, the F term in Eq. II.25 is minimized and is expressed as:

$$F_{\min} = F_{\text{metal}} * 1/2 * C_p^{m_p} \left[1 + \frac{a_1^2}{(a_1^2 - 1)^{1/2}} \left(\frac{a_1}{a_2} \right)^{2m_p} C^{-m_p} \right]^2 \quad \text{for hybrid modes} \quad (II.37)$$

$$\text{where } F_{\text{metal}} = \frac{n_{Ag}}{n_{Ag}^2 + \kappa_{Ag}^2} \quad (II.38a)$$

$$F_{\text{film}} = 1/2 * C_p^{m_p} \left[1 + \frac{a_1^2}{(a_1^2 - 1)^{1/2}} \left(\frac{a_1}{a_2} \right)^{2m_p} C^{-m_p} \right]^2 \quad (II.38b)$$

The minimized F value, or F_{\min} , has two contributions: one from the metal and one from the one or more dielectric films. Eq. II.38a is the figure of merit for silver, F_{metal} , and is calculated using both the n and κ values of the metal reflector. The figure of merit for the dielectric film(s) is given in Equation II.38b, and is denoted by F_{film} . The F_{film} , and

subsequently F_{\min} values are entirely dependent on which two dielectrics are chosen. If only one dielectric layer is deposited, F_{film} becomes:

$$F_{\text{film}} = \frac{1}{2} \left(1 + \frac{n_d^2}{\sqrt{(n_d^2 - 1)}} \right)^2 \quad (\text{II.39})$$

The straight loss for $\text{HE}_{1\text{m}}$ modes is calculated for an Ag HGW coated with a single dielectric using:

$$\alpha_{1\text{m}} = \left(\frac{U_{nm}}{2\pi} \right)^2 \left(\frac{\lambda^2}{a^3} \right) \left(\frac{n_{\text{Ag}}}{n_{\text{Ag}}^2 + \kappa_{\text{Ag}}^2} \right) * \frac{1}{2} \left(1 + \frac{n_d^2}{\sqrt{(n_d^2 - 1)}} \right)^2 \quad (\text{II.40})$$

When an even number of layers is added ($2m_p+2$), the attenuation coefficient of the hybrid modes has a minimum value at:

$$(a_2^2 - 1)^{1/2} n_0 k_0 * \delta_{\text{ir}} = \pm \tan^{-1} \left[\frac{(a_1^2 - 1)^{1/2}}{(a_2^2 - 1)^{1/4} * a_1} \left(\frac{a_1}{a_2} \right)^{m_p} C^{m_p/2} \right] \quad (\text{II.41})$$

For an even number of layers, the impedance and admittance change again. These expressions are not included here. For an even number of layers, F_{film} is given by:

$$F_{\text{film}} = \frac{1}{2} * \left[\frac{a_1^4}{(a_1^2 - 1)} \left(\frac{a_1}{a_2} \right)^{4m_p} C^{-m_p} \right] * \left[1 + \frac{(a_1^2 - 1)}{(a_2^2 - 1)^{1/2} * a_1^2} \left(\frac{a_2}{a_1} \right)^{2m_p} C^{m_p} \right]^2 \quad (\text{II.42})$$

for hybrid modes

When there are no dielectric layers present,

$$\alpha_{\text{HEnm, metal}} = \frac{n_0 k_0 u_0^2}{(n_0 k_0 a)^3} F^{(0)} \quad (\text{II.43})$$

$$F^{(0)} = \frac{n}{2} \quad \text{for hybrid modes.} \quad (\text{II.44})$$

Figure II.6 shows the calculated reduction in the F_{film} term for three different dielectric pairs. The number of layers ranges from one to five for each pair of dielectric materials. F_{film} is the ratio between the attenuation of the total WG structure and the attenuation of the Ag only WG structure. The trend of this term was isolated in the chart to illustrate the significant effect coating with a dielectric film has on the attenuation of the WG.

Since single layer ($m_p=0$, $a_1=n_d$) waveguides are commonly used, the simplified form of Eq. II.36 (using the definition of k given in Eq. II.1 and $n_0=1$) for a single layer is restated:

$$\delta_{1r} = \frac{\lambda_{\text{opt}}}{2\pi\sqrt{(n_d^2 - 1)}} \tan^{-1} \left[\frac{n_d}{(n_d^2 - 1)^{1/4}} \right]. \quad (\text{II.45})$$

This equation allows the thickness of a single dielectric layer (δ_{1r}), with a refractive index of n_d , to be calculated for optimal propagation of radiation at a wavelength, λ_{opt} .

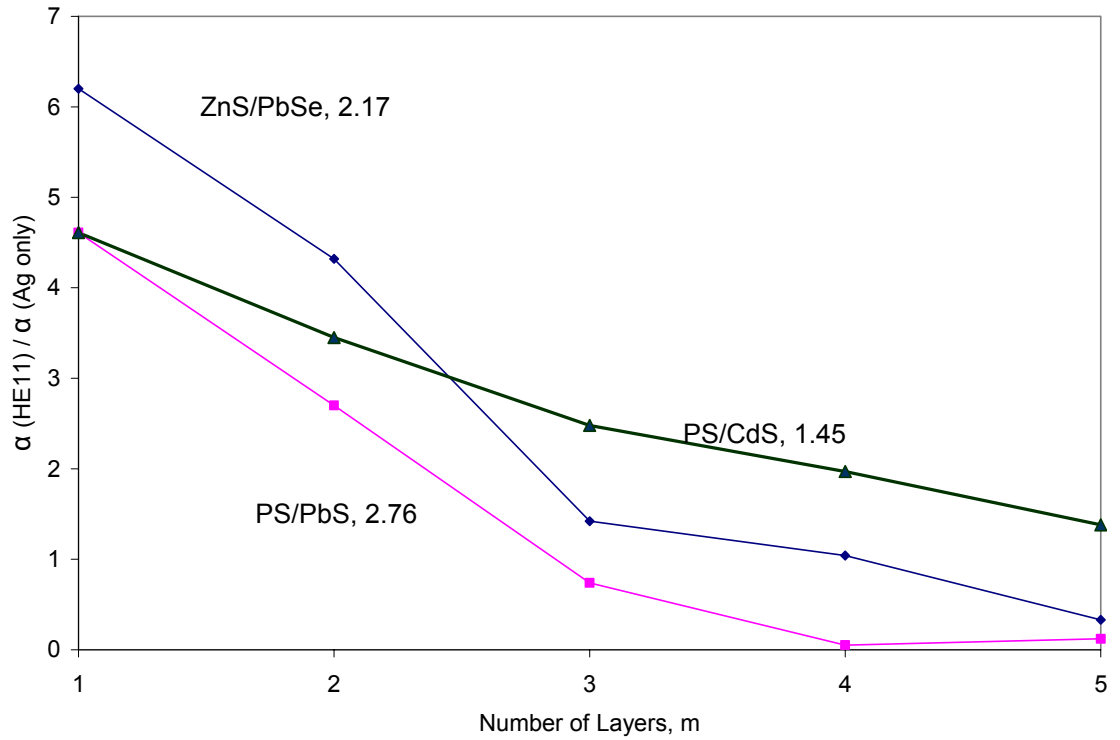


Figure II.6 Calculated reduction of the ratio: attenuation for HE_{11} mode/attenuation for Ag-only ratio for single layer and multilayer dielectric coatings in Ag coated HGWs at $2.94 \mu\text{m}$. For the single layer calculations, the low index material of the pair (PS or Zn) was used. For each line, the dielectric pair is listed, followed by the index contrast. It can be seen that for a larger index contrast, there is greater reduction in attenuation with each layer added. Since MK theory (the theory used to calculate theoretical loss values) does not include absorption values, the values were not included in these calculations.[3,6]

II.C.3. Other Contributors to Straight Loss

Other parameters that can potentially contribute to the straight loss are thickness variation and dielectric material absorption. In the above calculations, MK ignored these considerations by saying the thicknesses were exactly those calculated using the expressions they stated and that the dielectrics were absorption free. They did further calculations to see what impact the dielectric absorption and a thickness deviation of up to 40% would have on the theoretical loss. Dielectric absorption, in waveguides with several layers or less, was shown to not affect the loss until the extinction coefficients were greater than 10^{-2} . Hence, it is common, in practice, to refer to dielectrics with κ values less than 1×10^{-2} as transparent (or non-absorbing) and suitable for use in HWs. OmniGuide[®] has shown that an all-dielectric waveguide (containing no metallic layer) that includes materials with high extinction coefficients ($>10^{-2}$) can be made. These devices are alternatives to our WGs when many dielectric layers are included, approximately 10 for low loss hybrid mode propagation of a few meters rather than our typical 1 to 3 layers.[7] It has also been shown that the thickness deviation from the calculated value of up to 40% did not double the loss and a variation of 10% would not make a significant impact on the loss even with 10 layers deposited.[3,8]

II.C.4. MK Theory for Bending Loss

During the same year (1984) MK developed a theoretical understanding for straight losses seen in HW, MK with Harada developed a theoretical understanding for the loss on bending observed in HW.[9] They found a $1/R$, not $1/R^2$ dependence of the additional

loss on bending. Starting with Maxwell's equations and maintaining small surface impedance and admittance, the attenuation coefficient for the bend contribution becomes:

$$\alpha_{\text{bend}} = \alpha_{\text{straight}} * \left(\frac{1}{3} \left(\frac{n_0 k_0 a}{u_o} \right)^4 \left(\frac{a}{R} \right)^2 \right) * \left(\left[1 - \frac{4n(n \mp 2)}{u_0^2} \pm \frac{3}{8} \delta_{n1} \frac{\text{Re}(y_{TM} - z_{TE})}{\text{Re}(y_{TM} + z_{TE})} (u_0^2 - 2) \cos 2\theta_o \right] \right) \quad (\text{II.46})$$

where

$$z_{TE} = (v^2 - 1)^{-1/2} \text{ and} \quad (\text{II.47})$$

$$y_{TM} = v^2 (v^2 - 1)^{-1/2}. \quad (\text{II.48})$$

II.D. Additional Bending Loss Considerations

There are other effects that can contribute to the increase in loss on bending. First, the additional loss on bending is sometimes due to localized “hot spots” and mode mixing, that is the coupling between the lower loss launch mode and higher loss modes.[10]

Also, bending usually causes such a large angle of incidence. As will be discussed further in section II.F, larger angles of incidence decrease reflection, thereby increasing loss.

II.E. Coupling Radiation to Waveguides

Hollow core waveguides have the potential to allow many modes of radiation to propagate. Some modes are more lossy than others and when these modes couple to the

lower loss modes, higher losses are measured. Hence the loss values measured experimentally are extremely dependent on how efficiently the lowest loss modes are coupled into the waveguide and the higher loss modes are excluded.[11] It has also been observed that skew rays can result in loss values similar to meridional rays when the incident angle is small enough. The optimal launch conditions are discussed by Miyagi and Matsuura.[12, 13] Aside from the launch condition, the quality of the films deposited (appropriate materials choices and surface roughness) is another reason for the discrepancy between the theoretical and measured loss.

When a TEM₀₀ beam with a spot size of ω at the beam waist is launched into the waveguide on axis, the modes that will travel down the waveguide have power ratio given by Equation II.49. [11]. Within the HE_{1m} family of modes, HE₁₁ is the lowest loss mode, as seen in Figure II.7, and is most efficiently launched into the waveguide when the ratio ω/a is approximately 0.64 and which gives an efficiency, $\eta=0.981$, as seen in Figure II.8.[14] The optimal value for ω/a varies as can be seen in Figure II.9.[11] For dielectric coated metallic waveguides, smaller transmission losses are achieved and the optimal ω/a ratio is less than 0.64. In general, there is a broad range of spot sizes for achieving the lowest loss. For waveguides with no dielectric layer or longer lengths, 0.64 is appropriate. [3,5]

$$\eta_m = \frac{\left[\int_0^a \exp(-r^2 / \omega^2) J_0(u_m \frac{r}{a}) r dr \right]^2}{\int_0^\infty \exp(-2r^2 / \omega^2) r dr \int_0^a J_o^2(u_m \frac{r}{a}) r dr} \quad (\text{II.49})$$

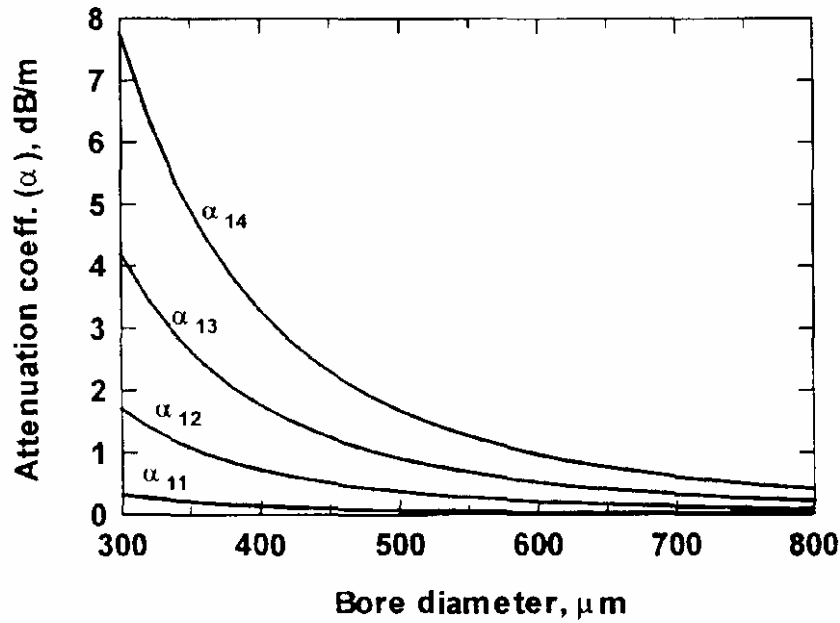


Figure II.7 The increase in attenuation with decreasing bore size for the lowest four hybrid modes at $\lambda=10.6 \mu\text{m}$. This plot shows high loss for the higher order modes, especially at bore sizes less than $500 \mu\text{m}$. This trend shows the higher order modes are essentially not propagated by smaller bore WGs. This is the reason the excellent mode profile from the smaller bore waveguides is often more desirable than that from larger bore sizes. Smaller bore waveguides are also more flexible. Thus, minimizing loss in smaller bore waveguides is a constant goal. [14]

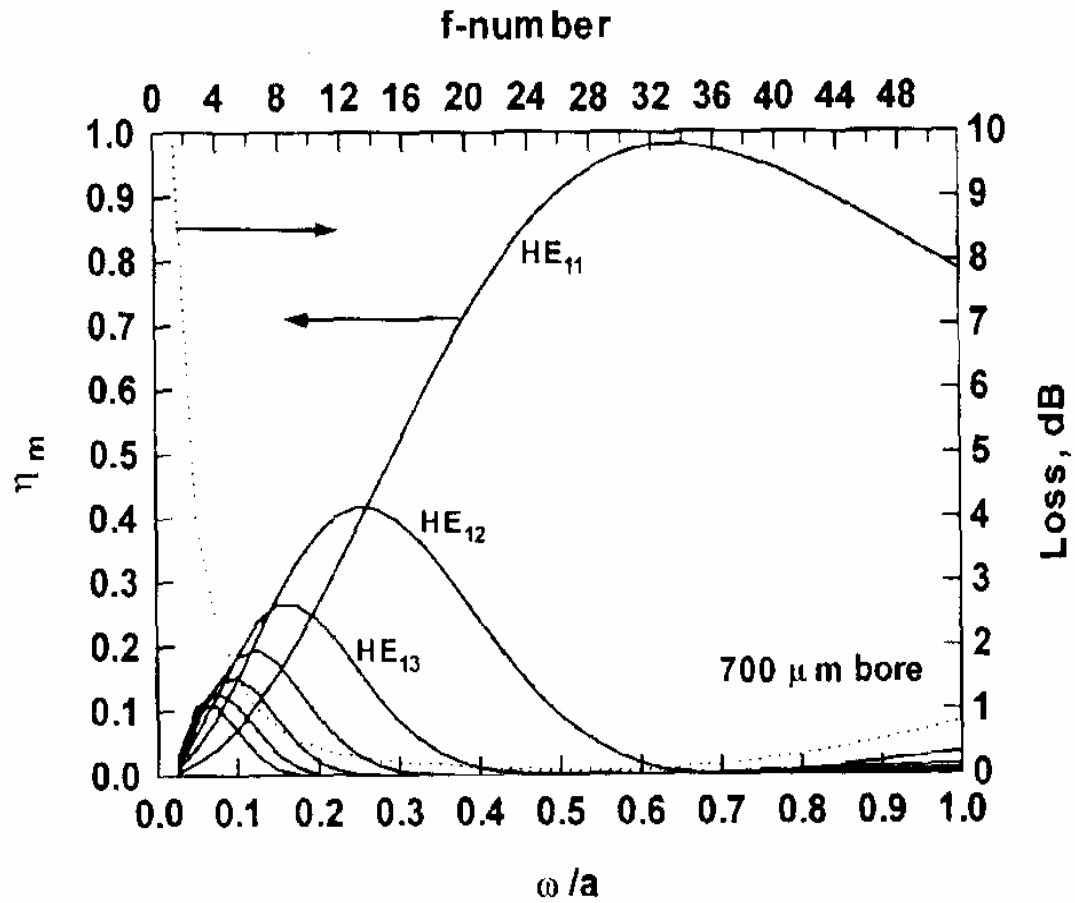


Figure II.8 Dependence of measured loss on the launch condition. This figure allows a more intuitive understanding of the dependence of measured loss on $f/\#$. If the launch conditions are not optimized, the coupling between the modes of lower and higher loss is significant and a higher loss value is measured. When the optimal launch condition for the HE_{11} mode is used most efficiently, the lowest loss is measured. These data were collected at $\lambda=10.6 \mu\text{m}$. [14]

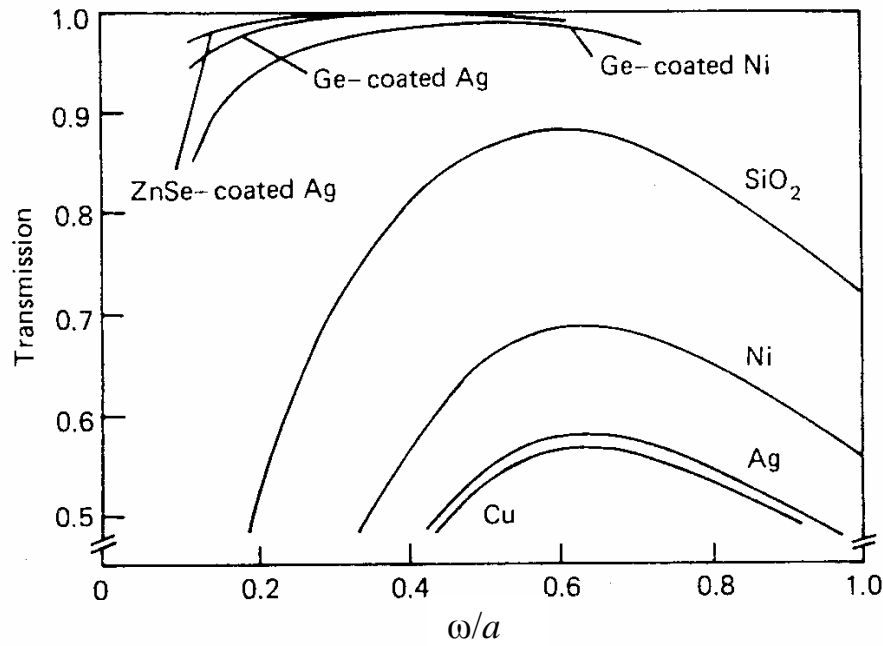


Figure II.9 The optimal value of ω/a varies. The specific metal and the presence of a dielectric coating determine the ratio that maximizes transmission. These ratios were calculated for $\lambda=10.6 \mu\text{m}$. [11]

The f-number ($f/\#$) is the parameter used to describe the launch condition in terms of the focal length of the lens used and the laser beam diameter. The value of the $f/\#$ is given by:

$$f/\# = f/D \quad (\text{II.50})$$

f is the focal length of the lens and D is the diameter of the laser beam.

This is a more practical measure of the launch conditions since the focal length of the lens is known and there are techniques to easily measure the beam diameter.[15] There is

an $f/\#$ that gives the highest efficiency of coupling to the HE_{11} mode. For $f/\#$ s higher than the optimal value, there is coupling of approximately 80% or greater efficiency coupling of the mode to the WG with no coupling to higher loss modes. This trend can also be seen in Figure II.8.

II.F. Surface Roughness

Surface roughness can be easily understood using the ray optics approach. For a perfectly smooth inner surface, in a WG of radius a , the attenuation due to scattering is given by [16]:

$$2 \alpha(\theta) = 1 - R(\theta) / (2 * a * \cot(\theta)). \quad (II.51)$$

$R(\theta)$ is the average (of the two polarizations) power reflection coefficient of light, θ is the angle of incidence with respect to the normal of the wall. If there is surface roughness, there is a new reflection coefficient. The change in the amount of reflected intensity is due to the increase (or decrease) in the incident angle, see Figure II.10. When the angle is larger, the amount of reflection is decreased. The new reflection coefficient is [17,18]:

$$R'(\theta) = R(\theta) \exp[-(4\pi n_i \sigma * \sin\theta/\lambda)^2]. \quad (II.52)$$

In the equation, σ is the root mean square (RMS) surface roughness and n_i is the index of refraction of the material adjacent to the air core – i.e., the material surface that interacts with the radiation.

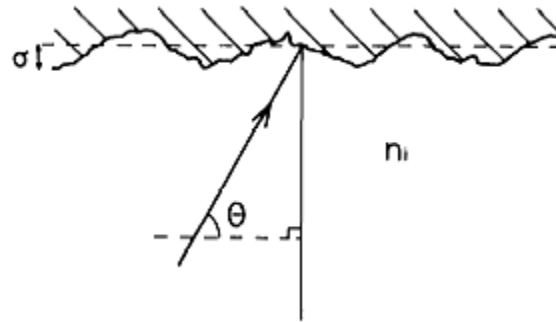


Figure II.10 A rough surface, with RMS roughness of σ , is shown here. The roughness either increases or decreases the incident angle, θ . [13]

Equation II.52 has large error when θ is small. It should also be noted that a dielectric with a smaller index of refraction means less scattering and, thus, would allow $R'(\theta)$ to more closely approach $R(\theta)$ than a higher index dielectric. In addition, the new reflection coefficient decreases more quickly than the coefficient in Eq. II.51 because of its $1/\lambda^2$ dependence. Figure II.11 shows how absorbance at the shorter wavelengths increases with increasing Ag deposition time. For the DLDP process, an increase in deposition time means an increase in surface roughness.[13] Roughness increases the loss by reduction the amount of light that can be reflected because it is scattered instead. [19]

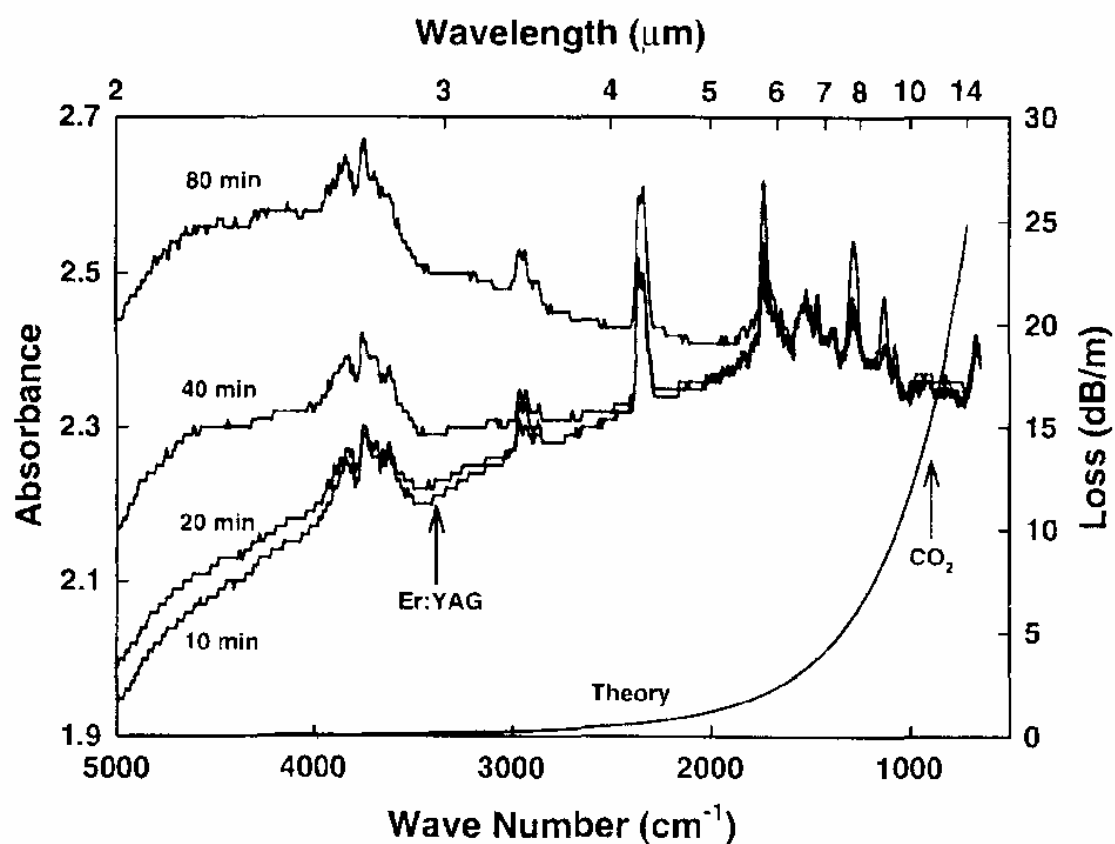


Figure II.11 The increase in roughness of the silver layer with longer deposition times for the DLDP process, as evidenced by an increase in absorption. The effect of time on roughness is significant up to 6 μm . Since the metal sulfides have the same nucleation and growth process, the same roughness increase with deposition time occurs. [18]

II.G. Polymer Characteristics

Polymers are used in HWs for IR transmission for several reasons. One, they have very attractive indices of refraction. That is, the indices are low, lower than most commonly used inorganic dielectrics. This means that they, along with a high index material, could result in a very high index contrast pairing which would reduce the number of layers necessary to obtain low attenuation. Also, the indices are in the range of 1.414, where there is minimum waveguide loss. For a single dielectric layer HGW, Eq. II.38b indicates that when the index of the dielectric material is 1.414, the F_{film} term is minimized. The trend is shown in Figure II.12.[3] PS has an index of 1.57 (at 2.94 μm) and κ of approximately 0.005 in the near IR. [20, 21]

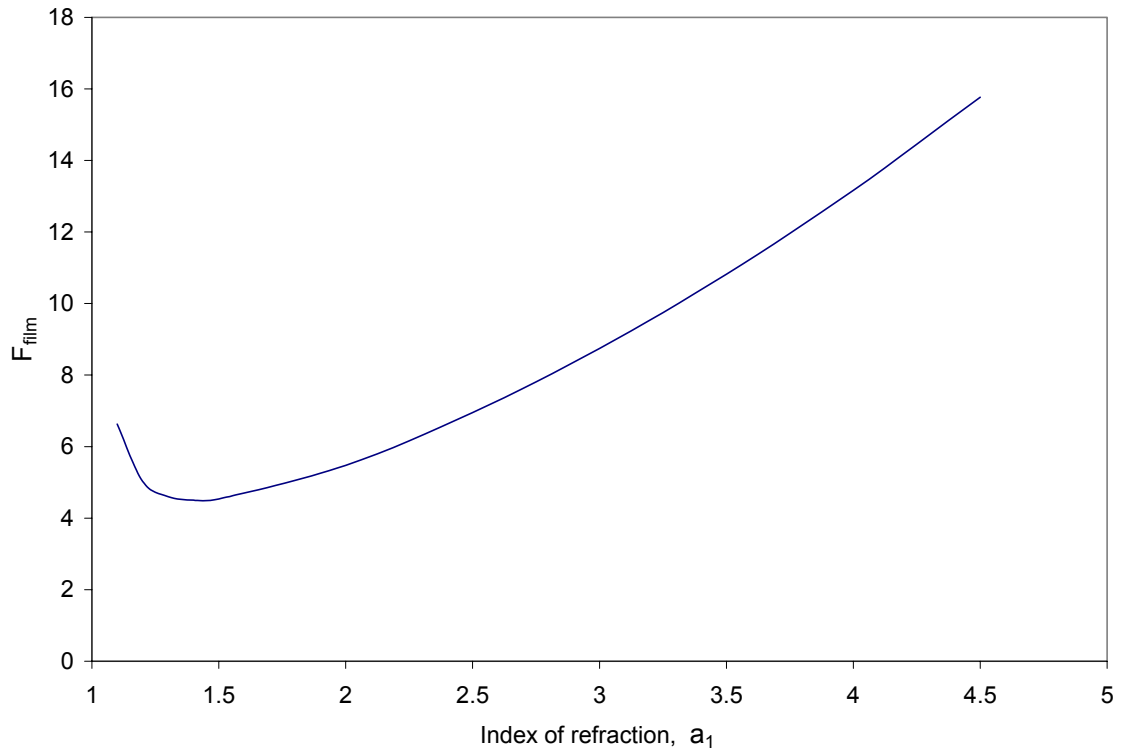


Figure II.12 A plot showing how F_{film} varies with a_1 , the index of the material coating the metal. This trend indicates 1.414 is the index for lowest loss. This trend is for a single dielectric waveguide. [3]

Polymer films are easy to deposit. This is important for our DLPD process because the polymer will wet and coat the substrate surface, and be wetted and coated by the solutions of next dielectric material. For medical applications, there are many polymers that are nontoxic to the body. For the two wavelengths mentioned throughout this work, 2.94 and 10.6 μm , there are many medical applications which make this an important consideration. Also, the layer thickness can be easily adjusted without increasing the surface roughness. The surface roughness in polymer film for HW has been shown to be strongly dependent on solvent evaporation rate, more than the surface roughness of the underlying layer or the rate of deposition.[22, 23] For this reason, controlled drying conditions and a solution in which the solvent evaporates more slowly is desirable. Finally, they have reasonably low intrinsic absorption at wavelengths of technological importance and in the visible range. In Figure II.13, PS is shown to have reasonably low absorbance at 2.94 μm , where the Er:YAG laser operates. In Figure II.14, cyclic olefin polymer (COP), another polymer commonly used in HWs for IR transmission, is shown to have reasonably low absorbance at the longer IR wavelengths.

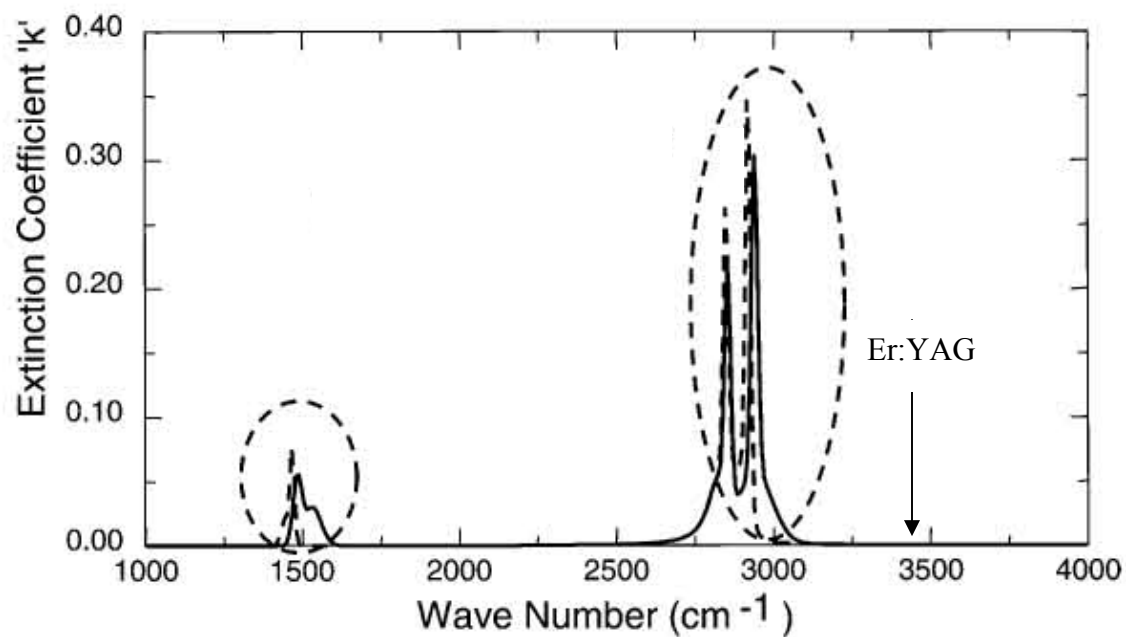


Figure II.13 A chart showing the value of the extinction coefficient of PS from 4000 cm^{-1} ($2.5 \mu\text{m}$) to 1000 cm^{-1} ($10 \mu\text{m}$). The intrinsic peaks of PS are circled. The peaks are due C-H bonds. For the two wavelengths considered in this work, $2.94 \mu\text{m}$ and $10.6 \mu\text{m}$, there is reasonably low intrinsic absorption to make this material an option. [25]

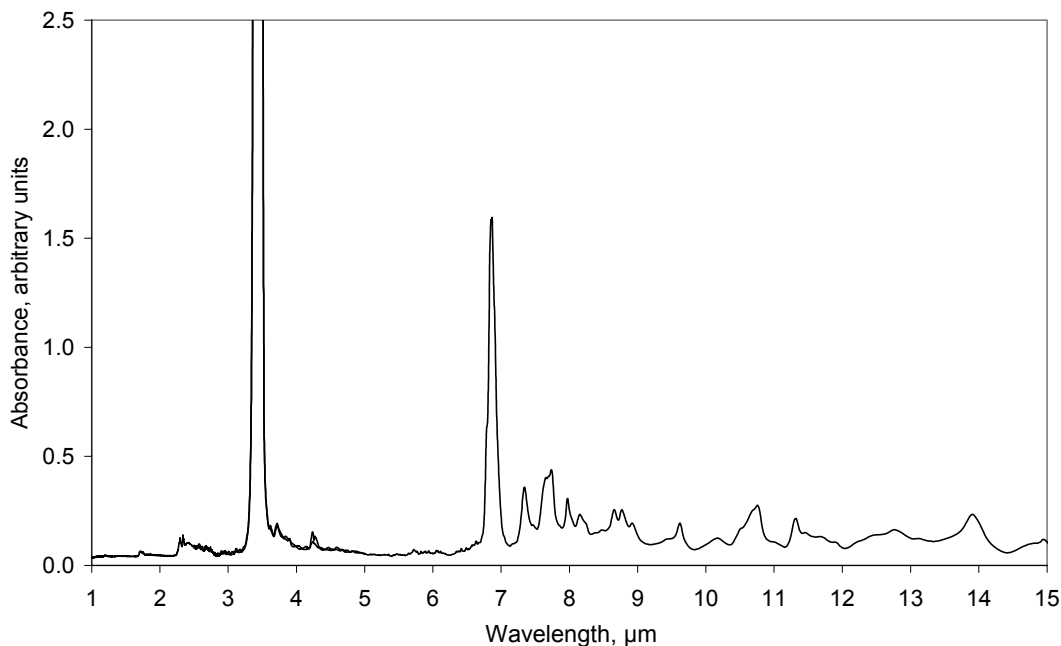


Figure II.14 An FTIR spectrum of a free-standing cyclic olefin polymer (COP) film.

The peaks around 3.2 and 7 μm are intrinsic to COP and are due to C-H bonds, similar to PS. As can be seen, there is low absorbance for many wavelengths in the IR. COP is commonly used. The index of refraction, n of COP is 1.53 (0.4-12 μm). [26, 27]

The low maximum power handling capability limits the use of polymers in the HWs.

They cannot be used in materials processing applications where high powers and small inner diameters are required. This limitation is due to the fact that the maximum working temperature must be below the polymer softening temperature. Typical values for softening temperatures are approximately 150 $^{\circ}\text{C}$. Polymers incorporated into HWs, also require applications in which there are soft curves or no bending. As mentioned earlier in

this chapter, hot spots can be formed which would damage the layer. In addition, higher angles of incidence occur when the WG has tighter bends. A temperature increase at the wall can occur when incident angles are close to 90° . [24]

REFERENCES

1. Edited by Sanghera, J.S. and Aggarwal, I.D., *Infrared Fiber Optics*, CRC Press, New York, 1998.
2. Marcatili, E.A.J., Schmeltzer, R.A., "Hollow metallic and dielectric waveguides for long distance optical transmission and lasers," *Bell System Technical Journal*, pp.1783-1809 (1964).
3. Miyagi, M., Kawakami, S., "Design theory of dielectric-coated circular metallic waveguides for infrared transmission," *J Lightwave Tech.* **LT-2**(2), pp.116-126 (1984).
4. Ibanescu, M., Johnson, S.G., Soljacic, M., et al., "Analysis of mode structure in hollow dielectric waveguide fibers," *Physical Review E* **67**, pp.0466081-8 (2003).
5. Croitoru, N., Dror, J., Gannot, I., "Characterization of hollow fibers for the transmission of infrared radiation," *Appl. Opt.* **29**(12), pp.1805-1809 (1990).
6. Edited by Palik, E.D., *Handbook of Optical Constants of Solids*, Academic Press, New York, 1985.
7. Johnson, S.G., Ibanescu, M., Skorobogatiy, M. et al., "Low-loss asymptotically single-mode propagation in large-core OmniGuide fibers," *Optics Express*, **9**(13), pp. 748-779 (2001).
8. Rabii, C.D., Harrington, J.A., "Measurement and control of thin film uniformity in hollow glass waveguides," *Opt. Eng.* **38**(12), pp. 2009-2015 (1999).
9. Miyagi, M., Harada, K., Kawakami, S., "Wave propagation and attenuation in the general class of circular hollow waveguides with uniform curvature," *IEEE Transactions on Microwave Theory and Techniques* **MTT-32**(5), pp.513-521 (1984).
10. Hill, C.A., Jenkins, R.M., Devereux, R.W.J., "Transmission of linearly polarized infrared light through curved hollow dielectric layers," *IEEE J Quantum Electronics* **24**(4), pp.618-624 (1988).
11. Hongo, A., Miyagi, M., Sakamoto, K., et al., "Excitation dependent losses and temperature increases in various hollow waveguides at 10.6 μm ," *Opt. and Laser Tech.* **19**(4), pp.214-216 (1987).
12. Miyagi, M., "Waveguide-loss evaluation in circular hollow waveguides and its ray-optical treatment," *J Lightwave Tech.* **LT-3**(2), pp.303-307 (1985).
13. Matsuura, Y., Saito, M., Miyagi, M., and Hongo, A., "Loss characteristics of circular hollow waveguides for incoherent infrared light," *J Opt. Soc. Am. A* **6**(3), pp.423-427 (1989).

14. Nubling, R.K., Harrington, J.A., "Launch conditions and mode coupling in hollow-glass waveguides," *Opt. Eng.* **37**(9), pp.2454-2458 (1998).
15. Yoshida, A., Asakura, T., "A simple technique for quickly measuring the spot size of the Gaussian laser beams," *Optics and Laser Technology*, pp.273-274 (1976).
16. Alaluf, M., Dror, J., Dahan, R., Croitoru, N., "Plastic hollow fibers as a selective infrared radiation transmitting medium," *J Appl. Phys.* **72**(9), pp.3878-3883 (1992).
17. Harrington, J.A., *Infrared Fibers and Their Applications*, SPIE Press, Washington, 2004.
18. Rabii, C.D., Gibson, D.J., Harrington, J.A., "Processing and characterization of silver films used to fabricate hollow glass waveguides," *Appl. Opt.* **38**(21), pp.4486-4493 (1999).
19. Dahan, R., Dror, J., Inberg, A., Croitoru, N., "Scattering of IR and visible radiation from hollow waveguides," *Proc. SPIE* **2396**, pp.115-119 (1995).
20. Ma, X., Lu, Q., Brock, R.B., et al., "Determination of complex refractive index of polystyrene microspheres from 370 to 1610 nm," *Physics in Medicine Biology* **48**, pp.4165-4172 (2003).
21. Inagaki, T., Arakawa, E.T., Hamm, R.N., Williams, M.W., "Optical properties of polystyrene from the near-infrared to the x-ray region and convergence of optical sum rules," *Physical Review B* **15**(6), pp.3243-3253 (1977).
22. Gopal, Veena, *New Dielectric Coatings for Low-Loss Hollow Glass Waveguides and Bundles*, Rutgers University thesis, 2003.
23. Wang, Y., Hongo, A., Kato, Y., et al., "Thickness and uniformity of fluorocarbon polymer film dynamically coated inside silver hollow glass waveguides," *Appl. Opt.* **36**(13), pp.2886-2892 (1997).
24. Gannot, I., Schrunder, S., Dror, J., et al., "Flexible waveguides for Er-YAG Laser radiation delivery," *IEEE Transactions on Biomed. Eng.* **42**(10), pp. 967-972 (1995).
25. Woollam, J.A., Bungay, C., Hilfiker, J., Tiwald, T., "VUV and IR spectroellipsometric studies of polymer surfaces", *Nuclear Instruments and Methods in Physics Research B*, **208**, pp. 35-39 (2003).
26. Billmeyer, M., *Textbook of Polymer Science*, Wiley Interscience, New York, 1971.
27. Iwai, K., Shi, Y.-W., Miyagi, M., et al., "Hollow infrared fiber with an inorganic inner coating layer with high durability", *Proc. SPIE* **6433**, pp. 64330L1-7 (2007).

Chapter III. Lead Sulfide

III.A. Introduction

Lead sulfide (PbS) is a well known and common material for use in infrared detection and solar energy absorptions.[1-8] Other applications include temperature and humidity sensing, photography, and diode lasers.[1] PbS, alone and as part of a cadmium sulfide (CdS)/ lead sulfide (PbS) bilayer system has been used as a selective coating for window glass for buildings to regulate indoor temperature and reduce costs.[2,9]

Much like the other dielectric materials discussed in this work, PbS thin films can be deposited by several different techniques. Techniques include atomic layer epitaxy [10] and low pressure CVD [11]. More recently, chemical bath deposition (CBD) has been a common technique.[1-9,12] Cyclic electrodeposition has also been recently demonstrated. [13]

In this project, the Ag/PbS deposition process was optimized. The goal was to make an Ag/PbS single dielectric layer HGW capable of efficient delivery of high power CO₂ laser radiation. The performance at longer wavelengths is the focus for this dielectric because absorption is high at wavelengths less than 3.5 μm . The Ag/PbS system could be an alternative to the Ag/AgI system for efficient transmission of the kilowatts of power used for welding and cutting applications. [14]

The deposition solutions used here have minimal reaction with the underlying Ag layer. Further modification of the solutions could reduce the formation of particles and other

reaction byproducts. One of the major attributes of the DLPD process is that continuous pumping also minimizes the inclusion of particles and byproducts in the film. Clearly this deposition process has the potential to produce Ag/PbS WGs with a performance that is comparable to Ag/AgI WGs, another system that is capable of efficient CO₂ transmission. This latter system has been shown to achieve the theoretical losses for tens of watts of power at 10.6 μm . [14]

According to Eq. I.5, materials with higher indices require thinner layers for optimal transmission at 10.6 μm . For comparison, at 10.6 μm , the optimal PbS layer thickness would be 0.48 μm , for AgI it would be 0.91 μm . AgI has an index of 2.1 while PbS has an index of 4.01. This thinner layer should be smoother than a thicker layer, based on previous results from the DLPD process, which show an increase in surface roughness with an increase in deposition rate. [15] In addition, since metals processing applications require smaller bore sizes, this reduced thickness is especially advantageous because it is easier to deposit.

In the early part of this project, PbS as a single layer degraded the Ag layer before the required PbS thickness could be achieved. This degradation was obvious because the Ag layer showed some brown specks through the WG wall. The goal was to modify the deposition process so that PbS deposition for any thickness would be successful.

III.B. Properties and Processing of PbS

PbS is a stable compound that can maintain its properties for years in an uncontrolled storage environment. The melting point for PbS is 1113°C and the optical constants are given in given Figure III.1.[16]

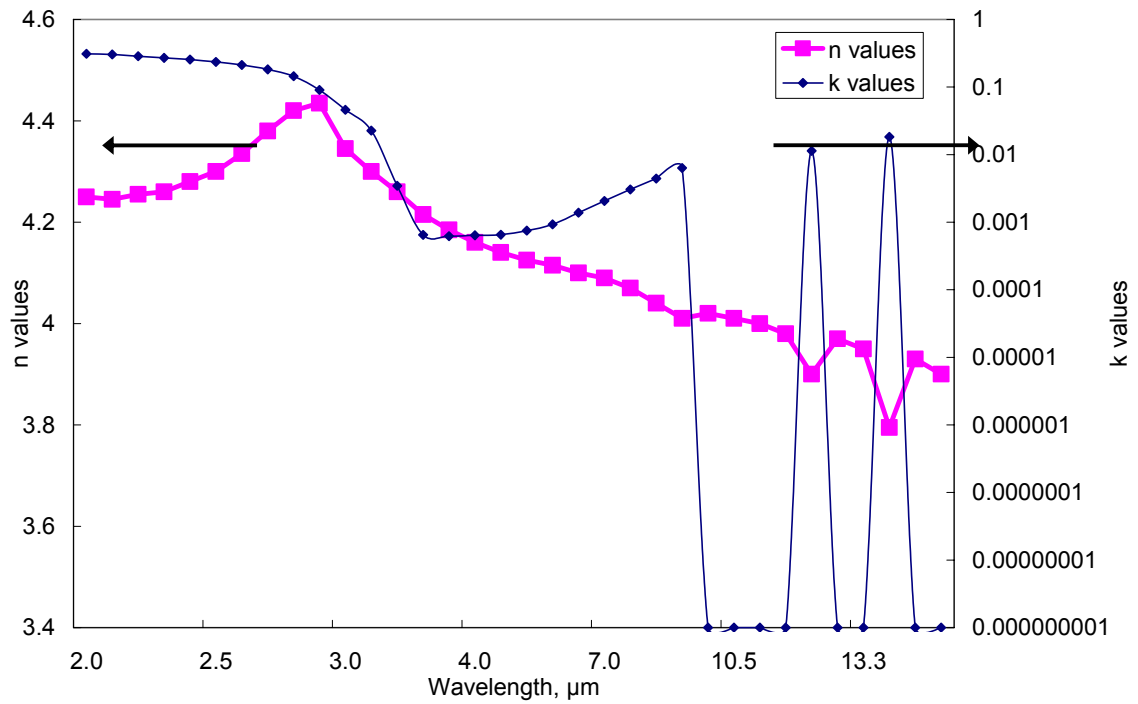
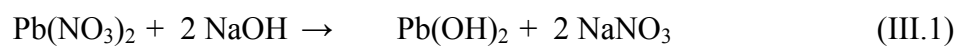


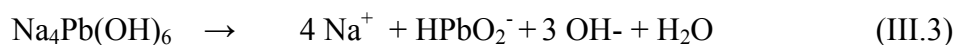
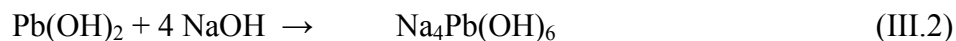
Figure III.1 Optical constants, n and κ , for PbS. [17]

The solution compositions used in this study did not damage the underlying Ag layer. The lead precursor was lead nitrate, $\text{Pb}(\text{NO}_3)_2$ and the sulfur precursor was thiourea, $\text{SC}(\text{NH}_2)_2$. Sodium hydroxide, NaOH , was both the complexing agent for the lead ions (Pb^{2+}) and the pH level adjuster. This reaction is carried out in basic conditions at room temperature. The concentrations used in this deposition were:

2 g $\text{Pb}(\text{NO}_3)_2$ / 750 mL H_2O ,	Solution 1
3 g NaOH / 250 mL H_2O ,	Solution 2
3 g $\text{SC}(\text{NH}_2)_2$ / 1000 mL H_2O .	Solution 3

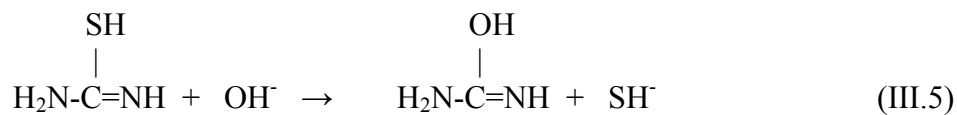
Distilled and deionized water was used to prepare the solutions. Solution 1 was mixed until all of the $\text{Pb}(\text{NO}_3)_2$ dissolved. Solution 2 was then added to Solution 1 to make a total solution of 1000 mL. The thiourea was similarly dissolved alone in 1000 mL of water. These concentrations differ slightly from those previously used.[18,19] Flow conditions varied greatly for the different bore sizes. For 1,000 μm bore samples, the flow rate was 6 mL/min and for 320 μm bore samples, 5.6 mL/min. The film growth rate was 0.0043 to 0.00648 $\mu\text{m}/\text{min}$ with these solution compositions. This is the same growth rate range as with the previous solution compositions.[18,19] The chemical reactions that occur to form PbS from lead nitrate and sodium hydroxide and thiourea are given in the literature.[3,18] The reactions occurring in the mixture of solutions 1 and 2 are:



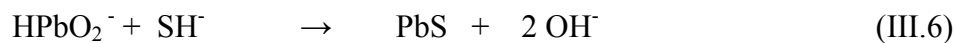


$\text{Na}_4\text{Pb(OH)}_6$ is the complex formed between NaOH and Pb. Once the complex dissociates (i.e., separates into one or more ionic species), HPbO_2^- is formed as in Eq.

III.3. HPbO_2^- is the important product from these three reactions because it will be used in a later reaction. While these three reactions are occurring in one solution the breakdown of thiourea occurs in the other solution:



When the mixture solution (containing solutions 1 and 2) and the thiourea solution are mixed, the following reactions occur to form PbS:



III.C. Experimental results for PbS in a single dielectric layer HGW

PbS was deposited on Ag with thicknesses that were optimized for 10.6 μm for different bore sizes. Figures III.2 and III.3 are FTIR spectra for 320 and 1,000 μm bore size samples. The interference peaks are sharp and clearly visible. In addition, the width and spacing of the peaks indicates a layer of uniform, optimal thickness has been deposited. The peak at the longest wavelength is the primary peak. The next peak should be at a wavelength that is half of the primary wavelength, the following peak at one-third, etc, as a result of Equation I.7. This spacing trend is an estimate of the quality of the film and the ideal spacing is approximately achieved for these samples.

The deposition of films that adhered well and did not react with the underlying Ag layer was achieved by lowering the concentration of the complexing agent and pH level modifier, NaOH. Previous formulations of Solution 2 contained up to four times (12 g NaOH/ 250 mL water) the NaOH concentration used in this project.[19] This was a problem because the excess NaOH was reacting with the Ag substrate layer which caused the speckling of the Ag layer. Delamination of the Ag/PbS bilayer was also observed in earlier work with the higher concentrations of NaOH.[19] The speckling is due to a reaction between the oxygen in NaOH and the Ag producing the insoluble brown silver oxide, Ag_2O [20]. Ag_2O can account for the change in appearance and eventual loss of adhesion of the silver layer.

The NaOH concentration was gradually reduced and even at 6 g NaOH / 250 mL water, speckling was seen through the wall. It was an interesting to note that a speckled sample

and an unspeckled sample have very similar FTIR spectra (compare Figures III.2 and III.4). The location of primary peak and peak spacing is very similar in the two spectra. It seems from the FTIR spectra of the speckled samples that the PbS film was close in composition and thickness to the films of the unspeckled samples. If there were a significant amount of simultaneous reactions were occurring or if the NaOH were somehow incorporated into the film, there would be more peaks present in the FTIR spectrum for the speckled sample that are not seen in the unspeckled spectrum. Many chemical species that contain at least one bond, such as the hydroxyl group OH-, have at least one very sharp absorption peak in the 1 to 15 μm range that can be used to identify an individual specie. Instead, the differences between Figure III.2 and III.4 are due to a difference in film thickness. The film quality of the speckled sample is also likely worse because the speckled films eventually delaminate completely whereas the unspeckled samples do not.[19] The slight increase in absorbance in the FTIR spectra of the unspeckled samples at longer wavelengths is likely due to slight non-uniformity in the thickness of the PbS film. This increase is seen in all of our DLPD samples.

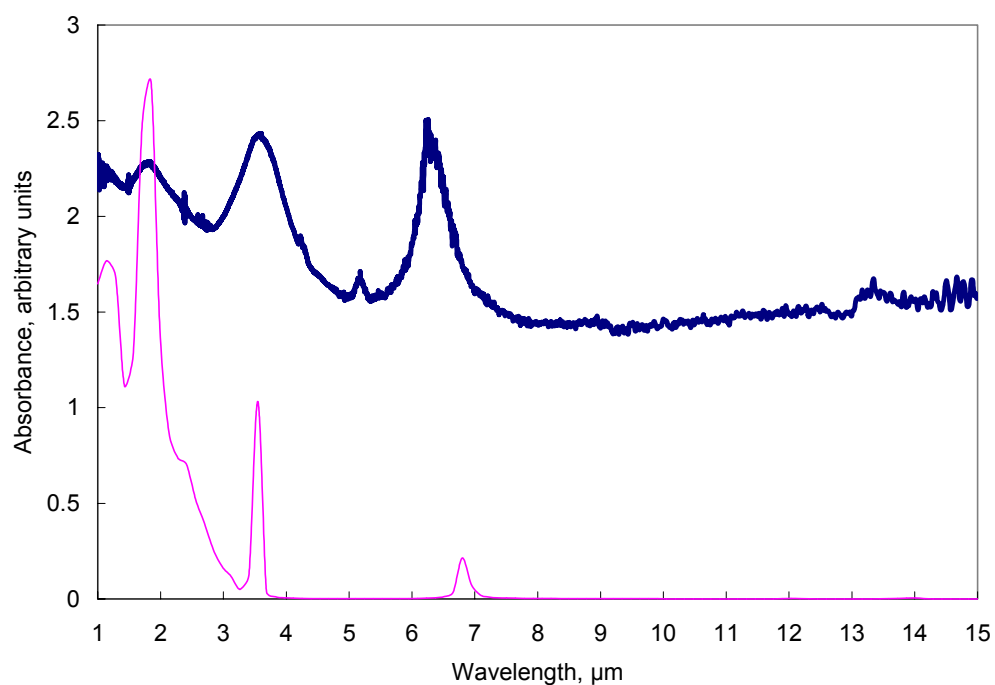


Figure III.2 Modeled and experimental FTIR absorbance spectra of a 320 μm bore Ag/PbS sample optimized for transmission at 10.6 μm , modeled data (thinner line) and experimental data (thicker line). The primary peak in the FTIR curve is at 6.26 μm , giving a thickness of 0.404 μm for the PbS layer.

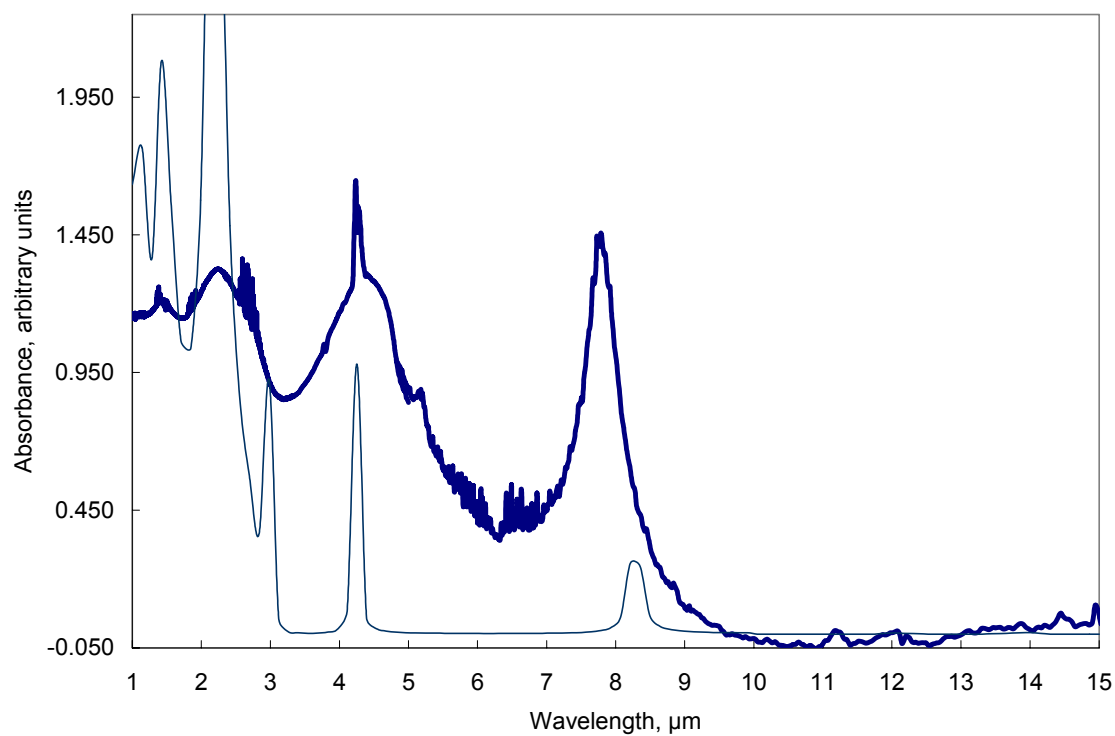


Figure III.3 Modeled and experimental FTIR absorbance spectra of a 1,000 μm bore Ag/PbS sample optimized for transmission at 10.6 μm , modeled data (thinner line) and experimental data (thicker line). The primary peak is at 7.73 μm , giving a thickness of 0.499 μm for the PbS layer.

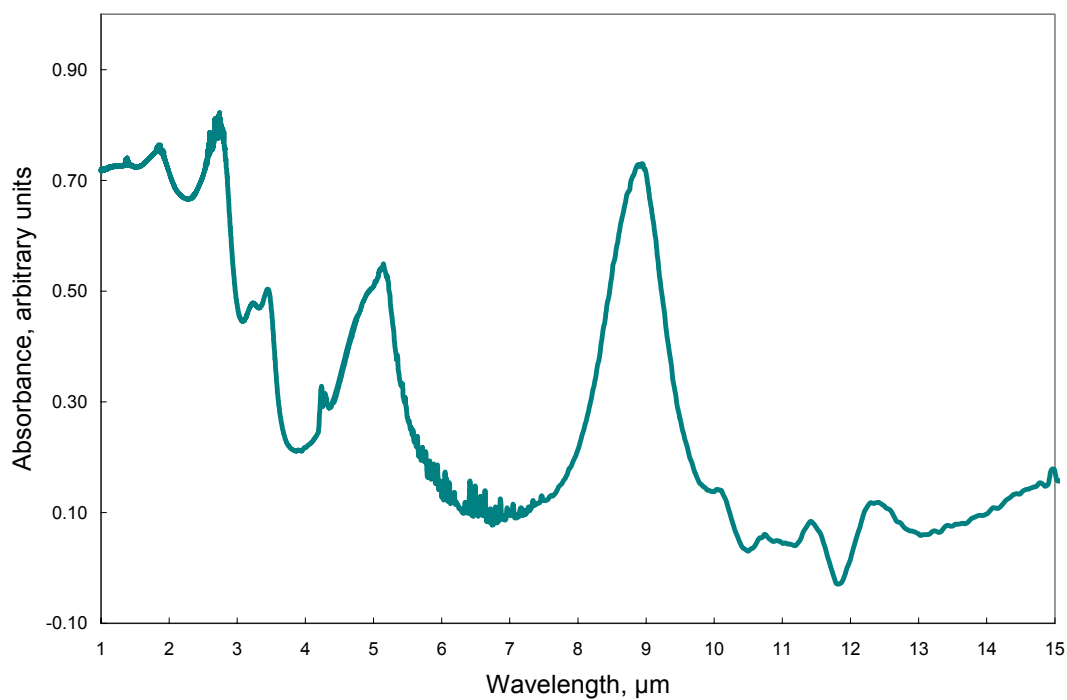


Figure III.4 FTIR spectrum of a 1,000 μm bore speckled Ag/PbS sample. Although the Ag layer had brown specks, the interference pattern here has sharp, well spaced peaks.

III.C.1. CO₂ laser loss measurements – Straight Loss

The losses were measured by the cutback method using an MPB cw CO₂ laser with a maximum power of approximately 18 W. The light was launched into the HGW using ZnSe lenses of different focal lengths. The power launched into the waveguides was less than 5 W for these measurements. The cutback lengths for each of the samples are given in Table III.1.

The low losses given in Table III.2 and Figure III.5 were obtained because high quality films were deposited, as seen in the FTIR spectra in Figures III.2 and III.3. The losses are also compared to previous results from this group for the Ag/PbS system and for Ag/AgI in Table III.2. The losses measured are the lowest ever achieved in this group for Ag/PbS. There is still some discrepancy between theoretical loss values (calculated using Eq. II.40) and measured values, however. There are a couple of possible sources of the discrepancy. One, surface roughness of the PbS film. There is always some roughness associated with each layer. The deposition of additional layers on Ag compounds the roughness. Two, some small amount of particles and reaction byproducts may be included in the film. Some particles would be present because it is not possible to avoid homogeneous nucleation entirely when using the DLPD process to form compound dielectrics. The particles would degrade the optical performance of the WG because they would make the surface rougher and increase scattering. The inclusion of byproduct is undesirable because it changes the composition of the film from pure material to some other composition. Of the two possibilities, it is difficult to say which one is the more significant contributor to the increase in loss.

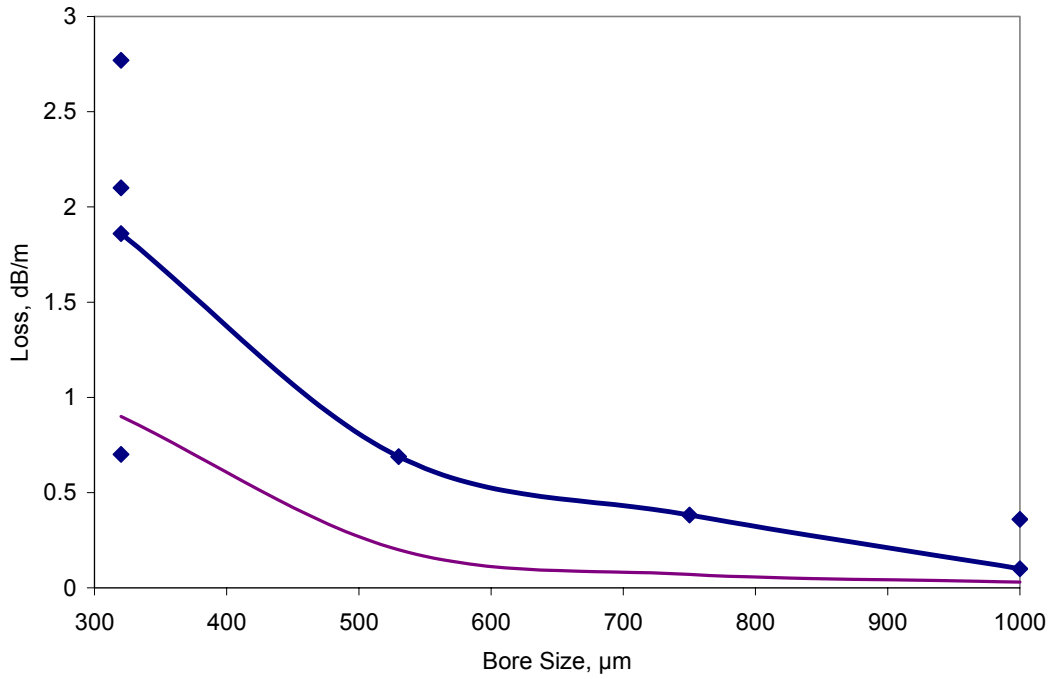


Figure III.5 A comparison of the calculated (thinner line) and the cutback (thicker line) loss for Ag/PbS samples of different inner diameters at 10.6 μm . The exact values are given in Table III.2. The closeness of the calculated and experimental values can be seen clearly in the Table III.2. Table III.1 gives the cutback lengths used for each measurement for each bore size.

Table III.1 Cutback lengths of Ag/PbS samples

Bore size (μm)	Cutback Lengths (m)
1000	0.7, 0.42
750	0.875
530	0.485
320	0.85, 0.775, 0.715

Table III.2 Calculated and measured loss values for Ag/PbS at 10.6 μm and previously measured loss values for Ag/AgI for comparison

Bore size (μm)	Theoretical Loss (dB/m)	Experimental Loss (dB/m)	Pedersen Results [21]	Ag/AgI [14]
1000	0.03	0.1	0.3	N/A
750	0.07	0.38	0.5	0.128(at 700 bore)
530	0.2	0.689	1.75	0.206
320	0.9	1.86	N/A	1.1

III.C.2. CO₂ laser loss measurements – Bending Loss

Bending loss was also measured for this Ag/PbS system. The total WG loss is the sum of the straight loss and the bending loss. The common technique of maintaining a constant length under bend and decreasing the bend to measure loss was performed here. The smallest bending diameter was 57 cm.

The bending losses were measured using the same cw CO₂ laser as used for the straight loss measurements. The light was polarized perpendicular to the plane of bending to obtain the lowest loss values. In this case, only the 1,000 μm bore size was tested because of the low output powers from the smaller bore samples. It was not possible to bend this larger bore sample to tight radii of curvature because of the inherent stiffness of larger bore sizes.

The slope of bending loss versus $1/R$ curve, Figure III.6, is m . In considering the performance on bending, the m value is the parameter that is compared between WGs; although these comparisons do not allow definite conclusions to be drawn. The m value is assumed to be dependent on the wavelength of measurement, the bore size of the sample and other factors. The range for m is generally found to be 0.13-0.60 dB. Generally samples with lower straight loss have lower m values.

The m value for a 1,000 μm bore sample is 0.45 as seen in Figure III.6 which clearly shows a linear increase in loss with a $1/R$ dependence. Haan obtained an m value of 0.15 for a 530 μm Ag/AgI sample with a straight loss of 0.5 dB/m.[22]

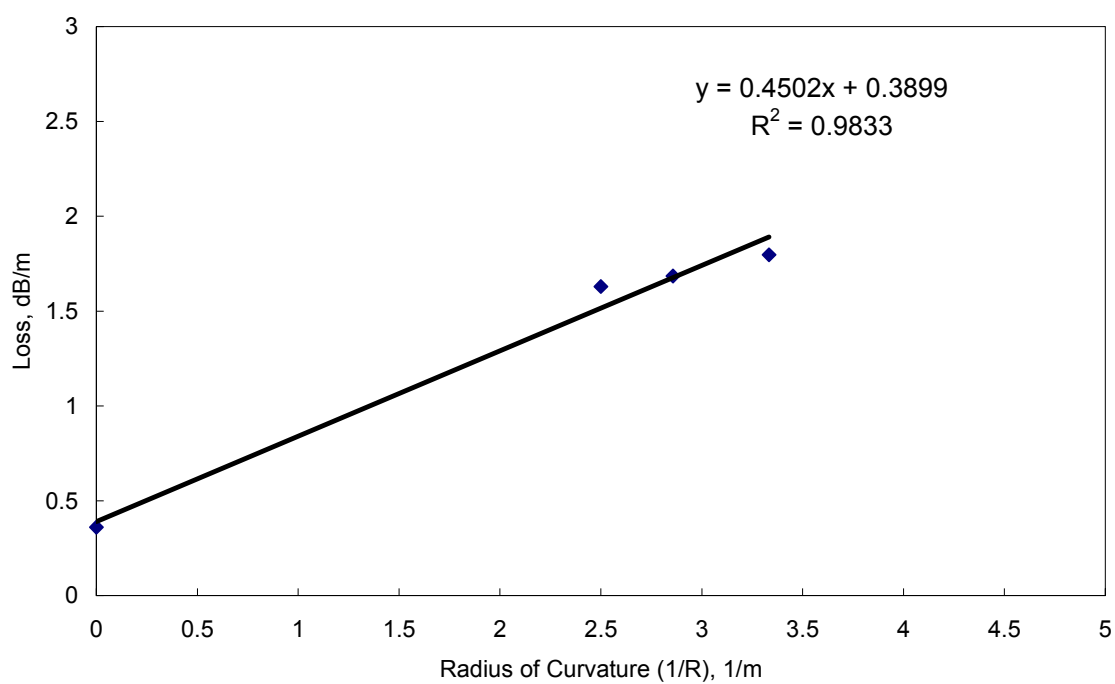


Figure III.6 Bending loss for a 1 m long 1,000 μm bore Ag/PbS sample. The smallest bending diameter was 57 cm.

III.D. Conclusions

The solutions developed in this project produce films that adhere to and do not react with the underlying Ag layer. There is no longer any delamination or discoloration when these solution compositions are used. Furthermore, the straight losses measured in this project are lower than the losses previously measured with other Ag/PbS samples made by this group. The solution compositions are slight modifications of previous compositions. The marked improvement in performance clearly shows the significance of the composition of the deposition solutions for the DLPD process. These results show that solution composition is much more significant factor in this process than flow rate when the temperature is kept constant.

Ag/PbS samples can definitely be developed to high efficiency for low, middle and high power IR transmission. The promise of efficient transmission at shorter IR wavelengths ($< 5 \mu\text{m}$) is not as great since both the index of refraction and the extinction coefficient of this material are so high (see Figure III.1). In addition, it is not feasible to produce layers of the required thickness when the index dictates that the layer would be very thin ($0.135 \mu\text{m}$) because the deposition time would be too short (the required deposition time would be 0.12 minute). The problem of such a shorter deposition could be circumvented if more dilute deposition solutions were developed. In either case, however, the uniformity of the layer would likely be difficult to maintain.

REFERENCES

1. Seghaier, S., Kamoun, N., Brini, R., Amara, A.B., "Structural and optical properties deposited by chemical bath deposition," *Materials Chem. and Phys.* **97**, pp.71-80 (2006).
2. Orozco-Teran, R.A., Sotelo-Lerma, M., Ramirez-Bon, R., et al., "PbS-CdS bilayers prepared by the chemical bath deposition technique at different reaction temperatures," *Thin Solid Films* **343-344**, pp.587-590 (1999).
3. Salim, S.M., Hamid, O., "Growth and characterization of lead sulfide films deposited on glass substrates," *Renewable Energy* **24**, pp.575-580 (2001).
4. Fernandez-Lima, F.A., Gonzalez-Alfaro, Y., Larramendi, E.M., et al., "Structural characterization of chemically deposited PbS thin films," *Mat Sci and Eng B* **136**, pp. 187-192 (2007).
5. Rempel, A.A., Kozhevnikova, N.S., Leenaers, A.J.G., van den Berghe, S., "Towards particle size regulation of chemically deposited lead sulfide (PbS)," *J Cryst. Growth* **280**, pp. 300-308 (2005).
6. Pentia, E., Pintilie, L., Matei, I., et al., "Combined chemical-physical methods for enhancing IR photoconductive properties of PbS thin films," *Infrared Phys. & Tech.* **44**, pp. 207-211 (2003).
7. Larramendi, E.M., Calzadilla, O., Gonzalez-Arias, A., "Effect of surface structure on photosensitivity in chemically deposited PbS thin films," *Thin Solid Films* **389**, pp. 301-306 (2001).
8. Najdoski, M., Minceva-Sukarova, B., Drake, A., "Optical properties of thin solid films of lead sulfide," *J Molecular Structure* **349**, pp.85-88 (1995).
9. Nair, P.K., Ocampo, M., Fernandez, A., Nair, M.T.S., "Solar control characteristics of chemically deposited lead sulfide coatings," *Solar Energy Materials* **20(3)**, pp. 235-243 (1990).
10. Leskela, M., Niinisto, L., Niemela, P., et al., "Preparation of lead sulfide thin films by atomic layer epitaxy process," *Vacuum* **41(4-6)**, pp.1457-1459 (1990).
11. Fainer, N.I., Kosinova, M.L., Rumyantsev, Y.M., et al., "Growth of PbS and CdS thin films by low-pressure chemical vapour deposition using dithiocarbamates," *Thin Solid Films* **280**, pp. 16-19 (1996).
12. Gadave, K.M., Jodgudri, S.A., Lokhande, C.D., "Chemical deposition of PbS from an acidic bath," *Thin Solid Films* **245(1-2)**, pp.7-9 (1994).

13. Saloniemi, H., Kemell, M., Ritala, M., Leskela, M., "Electrochemical quartz crystal microbalance study on cyclic electrodeposition of PbS thin-films," *Thin Solid Films* **386**, pp. 32-40 (2001).
14. Matsuura, Y., Abel, T., Harrington, J.A., "Optical Properties of small-bore hollow glass waveguides," *Appl. Opt.* **34**(30), pp.6842-6847 (1995).
15. George, R., New dielectric thin film coatings for Ag and Cu coated hollow infrared waveguides, Rutgers University thesis, 2004.
16. Lide, David E., *Handbook of Chemistry and Physics*, CRC Press, 2002-2003.
17. Edited by Palik, E.D., *Handbook of Optical Constants of Solids*, Academic Press, New York, 1985.
18. Gopal, V., New Dielectric Coatings for Low-Loss Hollow Glass Waveguides and Bundles, Rutgers University thesis, 2003.
19. Private communication with Pal Pedersen.
20. Schweig, Bruno, *Mirrors: A guide to the manufacture of mirrors and reflecting surfaces*, Pelham Books, London 1973.
21. Pedersen, P.O., Harrington, J.A., "Characterization of Metal-Sulfide Coated Hollow Glass Waveguides", *Proc. SPIE* **5317**, pp.53-61 (2004).
22. Haan, D.J., Harrington, J.A., "Hollow waveguides for gas sensing and near-IR applications," *Proc. SPIE* **3596**, pp.43-49 (1999).

Chapter IV. Polystyrene: Properties and Processing of an Optical Material

IV.A.1 General Introduction

The optical properties of polymers in the infrared have been studied for many years.[1-4] Polymers have been used in HWs for over 10 years as dielectric coatings and substrate tubing material. Several different polymers such as fluorocarbon polymer (FCP)[5], polyimide (PI)[6,7], cyclic olefin polymer (COP)[8-10], silicone resin[11] and various other nonspecific polymers [12] have all been used as dielectric coatings in HGWs. This project adds polystyrene (PS) to the list of polymers for use in HGWs. In particular, these polymers have been used as coatings for WGs optimized for Er:YAG and CO₂ wavelengths and for pilot beam (beam of visible light that indicates location of invisible IR beam) guiding. They are attractive options for dielectric coatings because good solvents are readily available so that electroless liquid phase deposition can be easily accomplished. One other polymer that has been incorporated in HWs, as substrate tube material, is polycarbonate (PC).[10] PC is desirable as a support tube material because large bore (greater than 1 mm) HWs can be made with a reasonable amount of flexibility.[13] PC is also lightweight, strong and inert.[13] One drawback of polymer substrate tubing is the inner surface is not as smooth as that of glass which limits the possibilities of using it for waveguides that will transmit shorter wavelengths and pilot beams.[10] Typical roughness values for the inner surface of glass substrate tubing fall within the 0.1 to 0.5 nm whereas for polymer substrate tubing, the inner wall roughness is in the 0.1 to 1.0 μm range.[14] The slightly greater roughness is not a significant

hindrance because PC tubing is primarily used in application in which larger bore samples, for sensor applications.

Polymer deposition is less complicated than the deposition of the metal sulfide and metal selenide compounds used as dielectrics in this project because there is no chemical reaction occurring during the deposition. Therefore, solution compositions and deposition conditions do not have to be tailored to account for the kinetics of compound formation. Polymers are known to form layers of uniform thickness as well as for demonstrating good adhesion to the substrate. In addition the lack of scattering particles, common in films made of compound materials, makes polymers even more attractive as a dielectric coating.[15] There are other considerations besides a lack of particles that dictate the success of polymer deposition. The three most important factors are: (1) wettability of a polar surface by a non-polar polymer, (2) rate of solvent evaporation and (3) starting viscosity of the polymer solution used in coating.[1,15,16] It is interesting to note that polymer deposition is routinely achieved without any sensitization for the silver surface.[1,2,5,11,12] These considerations, and others, will be discussed in this chapter in the context of the processing and properties of single and multilayer Ag/PS HGWs. The use of polymers in HWs is limited by the typically high absorbance at longer wavelength and low laser damage threshold.

The indices of refraction of a few polymers that are used in HW technology are given in Table IV.1. Polymers are of interest because they have indices that are relatively close to 1.414; most values are within the range from 1.5 to 1.6. The 1.414 value is the index

needed to achieve the lowest loss for transmission of the HE_{11} mode in a single dielectric layer HGW because it minimizes the FOM for the dielectric film, F_{film} (as determined by Eq. II.38b and seen in Figure II.12). They are, in general, moderately absorbing materials in the near IR. There is also the potential to have a large index contrast when polymers are used as the low index material in a multilayer structure. CdS and PbS were used as high index materials in this project.

Table IV.1 Indices of refraction of polymers used in HW technology [8, 17, 18]

Material	Index of refraction, n (wavelength of measurement)
PI	1.59 (2-12 μm)
PC	1.585 (589.3 nm)
FCP	1.35 (2-12 μm)
PS	1.58 (1.064 μm)

The leaky type WGs made in this project, with a metallic layer, require significantly fewer layers than the Omniguide® WG. The Omniguide® is an all-dielectric WG that incorporates one polymer and an IR glass as an all-dielectric WG without a metallic layer. There is a high index contrast between the two dielectrics and tens of layers are deposited. A large index contrast would further reduce the number of layers in both waveguides.

IV.A.2 Introduction to Polystyrene

Polystyrene is a common, well characterized material that is used in various optical applications.[3,13, 16,19-21] The molecular structure of the monomer, styrene, is shown below in Figure IV.1. The PS used in the project was a product of the BASF Corporation (now INEOS Styrenics). The product code was 148G K21 and it was one of the high-heat, medium flow, general-purpose crystal resin set.[22] Table IV.2 lists some of its properties. As a single layer, PS would be most efficient in the wavelength ranges from of 1 to 3 μm and from 3.6 to 5.1 μm , as can be seen in the spectrographic data in Figures II.12 and IV.2. Er:YAG (2.94 μm) and Nd:YAG (1.06 μm) are two widely used infrared sources in the 1 to 3 μm wavelength range, where PS seems most promising. The FTIR spectrum of a free standing PS film (see Figure IV.2) shows high absorbance at some longer wavelengths.

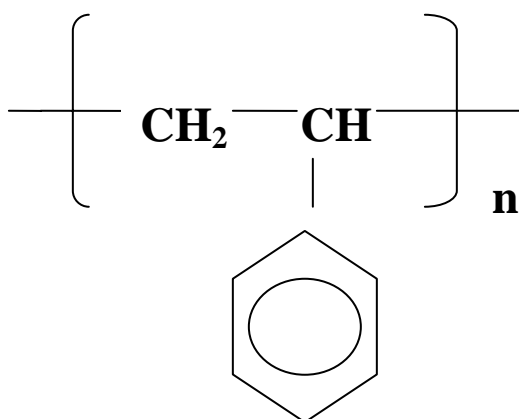


Figure IV.1 [4] The molecular structure of the monomer, styrene.

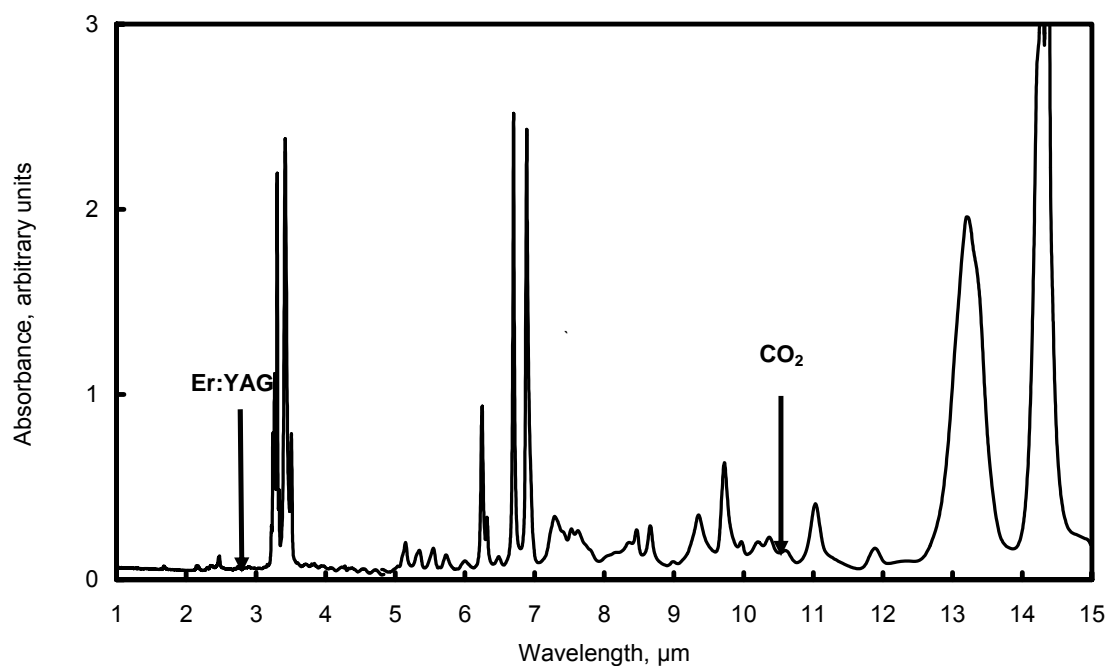


Figure IV.2 An FTIR spectrum of a free-standing PS reference sample (1.5 mm thick) was measured in this laboratory. For the two wavelengths considered in this work, 2.94 μm and 10.6 μm , there is reasonably low intrinsic absorption to make this material an option.

Table IV.2 Properties of Polystyrene 148G K21.[22]

Nominal flow rate (Condition G of ASTM D1238)	6
Specific Gravity at 73° F	1.04
Vicat Softening temp.	109° C
Water Adsorption	<0.1%

One characteristic that makes PS an attractive material option is the number of choices of suitable solvents. The goodness is determined by the difference between the solvent solubility parameter and the polymer solubility parameter. Polymer-solvent pairs with the smallest differences between the solubility parameters are the systems in which the polymer is well dissolved by the solvent. A more intuitive approach to determining whether a solvent is good is whether the polymer chain dimensions (and separation between chains) are increased or decreased when in contact with the solvent. If the chain dimensions increase, then the solvent is a good solvent and the polymer will be dissolved and phase separation will not occur. If the chain dimensions decrease, then the solvent is poor and phase separation is more likely to occur. Common solvents and their solubility parameters, and the solubility parameter of PS for comparison, are listed in Table IV.3. The goodness of a solvent can be changed by changing the temperature of the system and by introducing another solvent.[23] The solubility parameter of PS is closest to that of toluene.[1,24] This indicates toluene can thoroughly dissolve PS which is obviously necessary to form a uniform layer of PS.

The other characteristics, besides solubility parameter, are listed in Table IV.3 to clarify the process for choosing the most appropriate solvent for use in DLDP. First, surface roughness is considered because it is a significant contributor to the total WG loss for shorter wavelengths, such as 2.94 μm . Vapor pressure is a characteristic that directly determines solvent evaporation rate. A higher evaporation rate causes greater roughness. From Table IV.3, toluene is the best choice for solvent because it has, by far, the slowest evaporation rate; methyl acetate would be the worst choice if PS were to be used in a HW

designed to transmit Er:YAG radiation. The slower evaporation has been shown to produce less surface roughness in polymer thin films.[5] Finally, in depositing PS (nonpolar) on an Ag (polar) surface, wetting could be an issue. The dipole moment gives an indication of the degree of interaction possible between the solvent and a polar substrate. A larger dipole moment means there is more interaction between the solvent and the substrate. The dipole moment of toluene has proven to be sufficient to allow a PS/toluene solution to wet an Ag surface. In addition, the solvent with the highest dipole moment, methyl acetate, is not as attractive as toluene because of the difference between its solubility parameter and that of PS and its relatively high vapor pressure.

Table IV.3 Characteristics of 3 Common Solvents and PS [23,25]

Material	Solubility Parameter (MPa) ^{1/2}	Dipole Moment (debye)	Vapor Pressure (kPa)
Toluene	18.2	0.43	3.42
Benzene	18.8	0.00	11.30
Methyl Acetate	19.6	1.88	12.10
PS	17.5		

IV.B. Processing

The PS solutions were made by ultrasonically BASF PS pellets in toluene for 20 minutes at room temperature. Colorless, translucent solutions were formed at concentrations of 1 to 5 wt% PS in toluene. The solutions were made and stored in clear containers that were sealed to prevent solvent evaporation. The starting viscosity of PS/toluene solutions was measured for 1, 2, 3 and 5 wt% PS solutions. The results are shown in Figure IV.3. The data confirm that adding more PS to a toluene-based solution will increase the starting viscosity.[26] The increase in viscosity here is small because the increase in PS concentration is small. The molecular weight (MW) of PS also affects the viscosity of the polymer solution.[26] In this work only one MW of PS was used.

The deposition times of the Ag layer were chosen to optimize the WG for either the Er:YAG (20 minutes) and CO₂ (60 minutes) wavelengths. The Ag layer was thoroughly dried before the PS layer was deposited. The PS thin film was deposited by pumping the PS solution through the silvered tubing. The solutions were pumped vertically, from top to bottom, at a rate of either 1.6, 3.8, or 5.6 mL/min. The deposition process is very similar to the schematic shown in Figure I.1, except that only one flask, containing the polymer solution, would be used. As soon as the final drop of solution exited the waveguide, the drying process was started. Three different drying schemes were used to observe the effect of solvent evaporation rate on the thin film characteristics. One scheme was to hang the sample vertically and flow air through the hollow core for 1 minute and then allow the sample to dry with no flow while lying horizontally. The second scheme was to lay the sample horizontally in the ambient room environment with

no flow. The third scheme was to place the sample in an environment in which the direction of air flow was perpendicular to the axis of the WG. The WG axis was oriented perpendicularly to the direction of air flow to contrast the samples dried with the WG axis parallel to the direction of air flow.

IV.C. Experimental Results and Discussion

This work confirms many of the results previously observed during the deposition of another polymer, FCP, on a Ag coated HGW.[5] The significant factors affecting the characteristics of the polymer layer that had the same effect in our PS/toluene system and the FCP/perfluorochemical solution system were:

- starting viscosity of polymer solution,
- concentration of polymer in solution, and
- drying conditions (rate of solvent evaporation).

FTIR was used to characterize the resultant film during all of the parameter testing. As discussed in Chapter I, FTIR spectroscopy is a powerful tool for evaluating the ability to coat the underlying layer, thickness, thickness uniformity and to some extent the composition of the films deposited. The peak width is an indicator of the thickness uniformity in the axial direction of the waveguide. The peak spacing is an indicator of the thickness uniformity in the radial direction; the primary peak is used to calculate film thickness.

Polystyrene, as a single dielectric layer, can be successfully deposited from low concentrations of toluene solutions on silver as shown by the thin film interference patterns in the FTIR spectra seen in Figure IV.4 and Figures IV.6-8. There are clearly visible peaks, which are relatively narrow. In addition, the peaks are spaced close to the ideal spacing (as given by Eq. I.7). The number of peaks seen in the figures is determined by the thickness of the sample and the wavelength range. Thinner samples have more peaks at shorter wavelengths ($< 1 \mu\text{m}$).

IV.C.1. PS Deposition Results and Discussion

Many results, similar to those obtained here, have been reported for another system, FCP/perfluorochemical solution system.[5] The viscosity dependence on polymer concentration for the PS/toluene system is similar to that of the FCP/perfluorochemical solution system.[5] These data are shown Figure IV.3. Both the coefficient and the exponent are very similar for these two polymers.

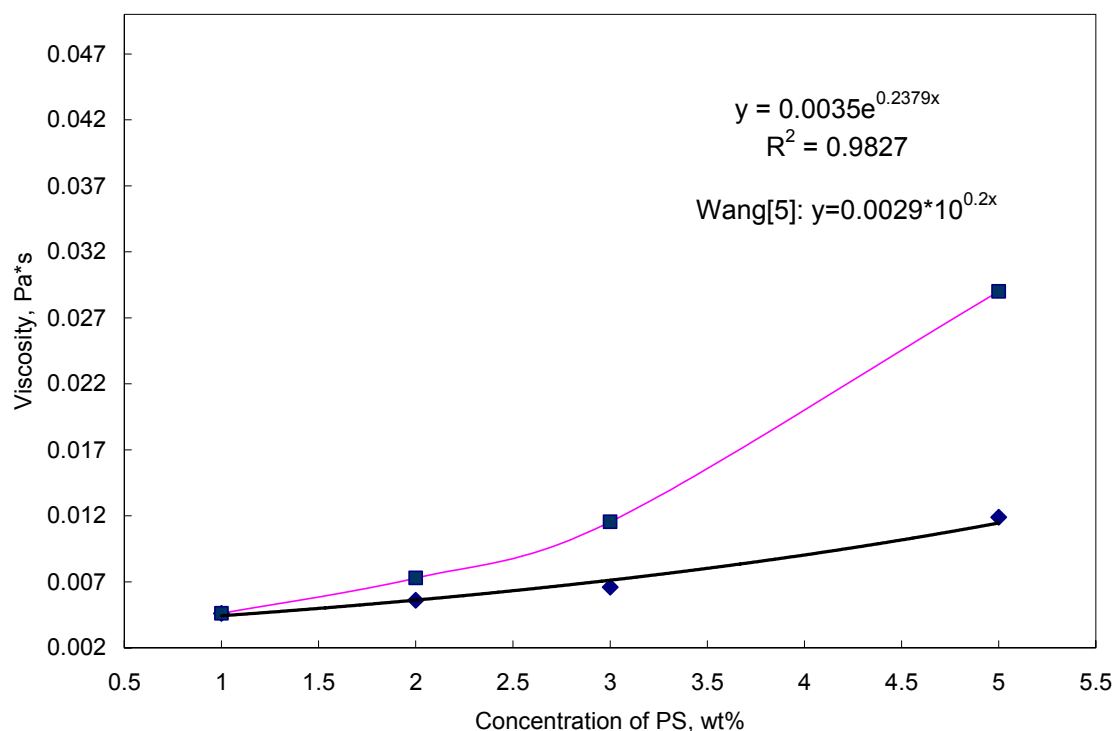


Figure IV.3[5] Viscosity data for PS/toluene solutions of different concentrations (diamonds). As expected, the viscosity increases with increased PS concentration. The viscosity dependence on concentration is similar to the dependence seen with the FCP/perfluorochemical solution (squares) for the 1 to 3 wt% PS range used in this project.

We also found, similar to the findings of the FCP/perfluorochemical solution system, that a higher PS concentration (i.e., a higher starting viscosity) in the PS/toluene solution resulted in a thicker layer. The trend of increasing layer thickness with increasing PS

concentration can be seen in Figure IV.4. The thicknesses were calculated using Eq. I.7 and are given in Table IV.4.

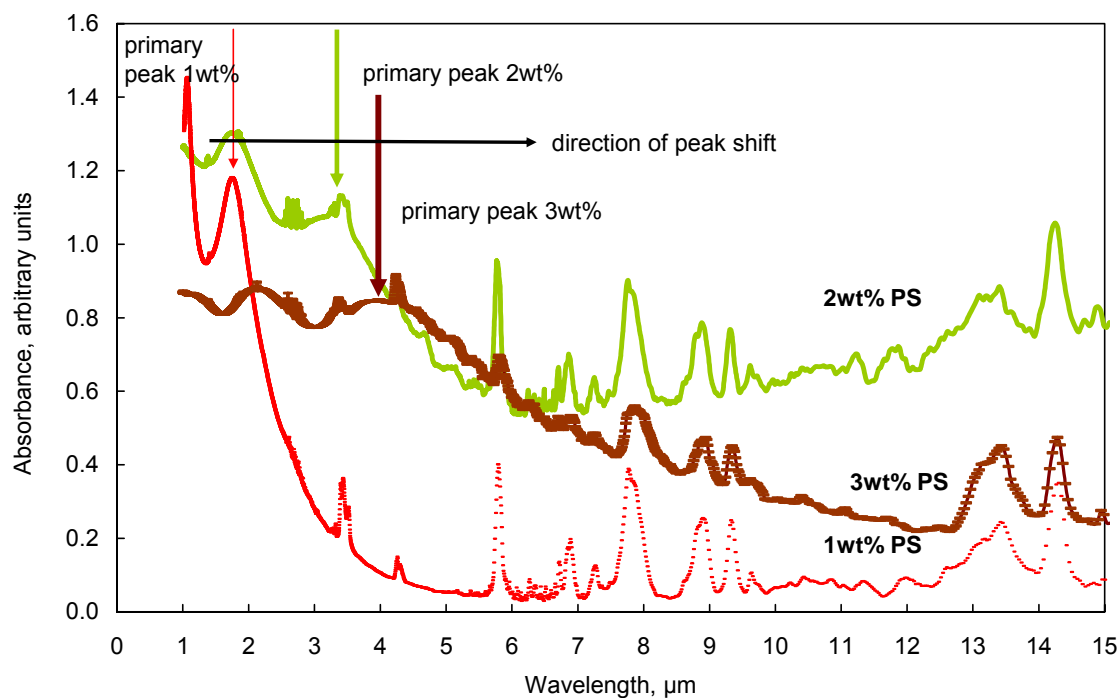


Figure IV.4 FTIR spectra of 3 Ag/PS samples made with different PS concentrations in the coating solutions. The curves are labeled as 1, 2, and 3 wt% PS. The flow rate was 5.6 mL/min and the samples were dried without air flow. As expected from the results from the FCP/perfluorochemical solution study, a higher polymer concentration results in a thicker film layer. The peaks located beyond 5 μm are intrinsic PS peaks also seen in Figure IV.2. The primary peaks are indicated by arrows.

Table IV.4 PS thickness for different PS/toluene solution concentrations (from Fig. IV.5)

Concentration (wt%)	Thickness (μm)
1	0.349
2	0.678
3	0.845

Increasing the polymer concentration increases the layer thickness because for higher concentrations, the polymer chains are closer together, even when a good solvent is used, as shown in Figure IV.5. The higher polymer/solvent ratio means there is less time for the polymer chains to reconfigure themselves before the viscosity rises to a level where no more movement is possible. The fact that the chains are closer at this point means they will be in a more voluminous configuration than they were in the initial wetting stage and there will be less contraction so that a substantial difference in the chain dimension is less likely.[24]



Figure IV.5 The left side (A) shows extended and well spaced chains as would be expected for a low concentration PS solution. The right side (B) shows more voluminous chain configurations as would be expected in a high concentration sample.[26]

Solutions were pumped through Ag-coated HGWs at different rates and the effect on film thickness is shown in Figure IV.6. The thickness values are given in Table IV.5. For these measurements, the PS concentration and the drying conditions were the same for all samples. The results from this work differ from those obtained in the FCP/perfluorochemical solution work.[5] While Wang et al. measured thicker layers for higher flow rates, we measured thinner layers. The difference is due to the fact that the polymer solution is being treated differently in each study. In this work, the PS solution was pushed down the HGW (see Figure I.1) while the FCP solution was pulled down the HGW as shown in Figure IV.9. The results shown here follow the same trend as when spin coating is used to coat a dissimilar surface with a polymer solution. Pushing the solution down the tubing using a pump is similar to the centrifugal force acting on the

solution during spin coating.[24,27] In addition, similar to spin coating, most of the solvent is likely consumed in interacting with the surface during deposition.[24]

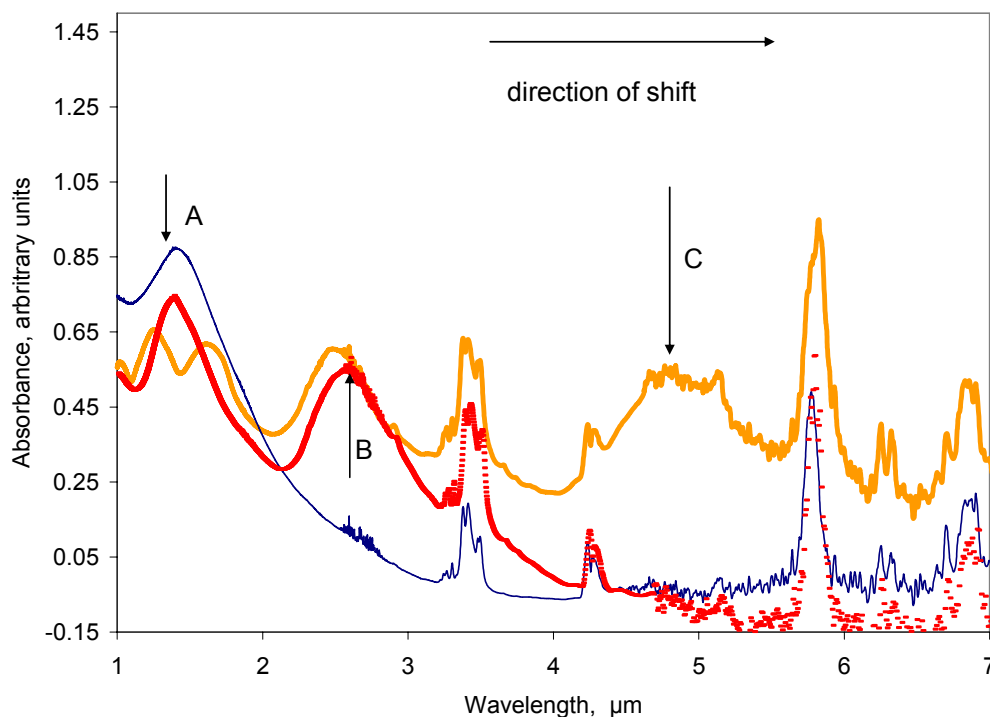


Figure IV.6 The primary peaks (indicated by arrows) shift to longer wavelengths for slower flow rates. The flow rates are A: 5.6 mL/min, B: 3.8 mL/min and C: 1.6 mL/min. The shift indicates thicker layers are deposited for slower flow rates and the same drying condition (flowing air, 1min then no flow dry, 2 hours). The samples here are Ag/1wt% PS, 1 mm bore. Thickness values are given in Table IV.5 for comparison.

Table IV.5 PS thickness for different flow rates (data from Figure IV.6)

Flow Rate (mL/min)	PS layer thickness (μm)
5.6 (A)	0.272
3.8 (B)	0.506
1.6 (C)	0.971

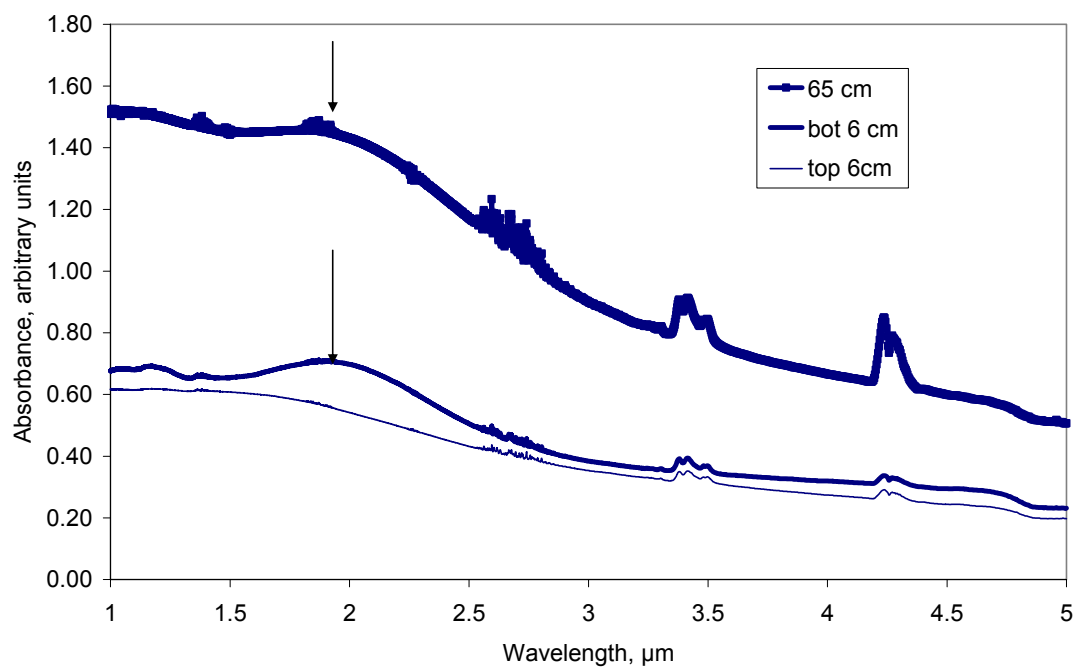


Figure IV.7 FTIR spectra from different points of an Ag/1 wt% PS, 750 μm bore sample show the variation in film thickness. The layer thickness at the top of the sample (the inlet end) is thicker than the longest, middle section of the sample and the bottom. The thickness variation between the bottom of the sample (the outlet end) and the longest, middle section of the sample is only 1%. The topmost portion of the sample is much thicker and would be trimmed before the sample was used.

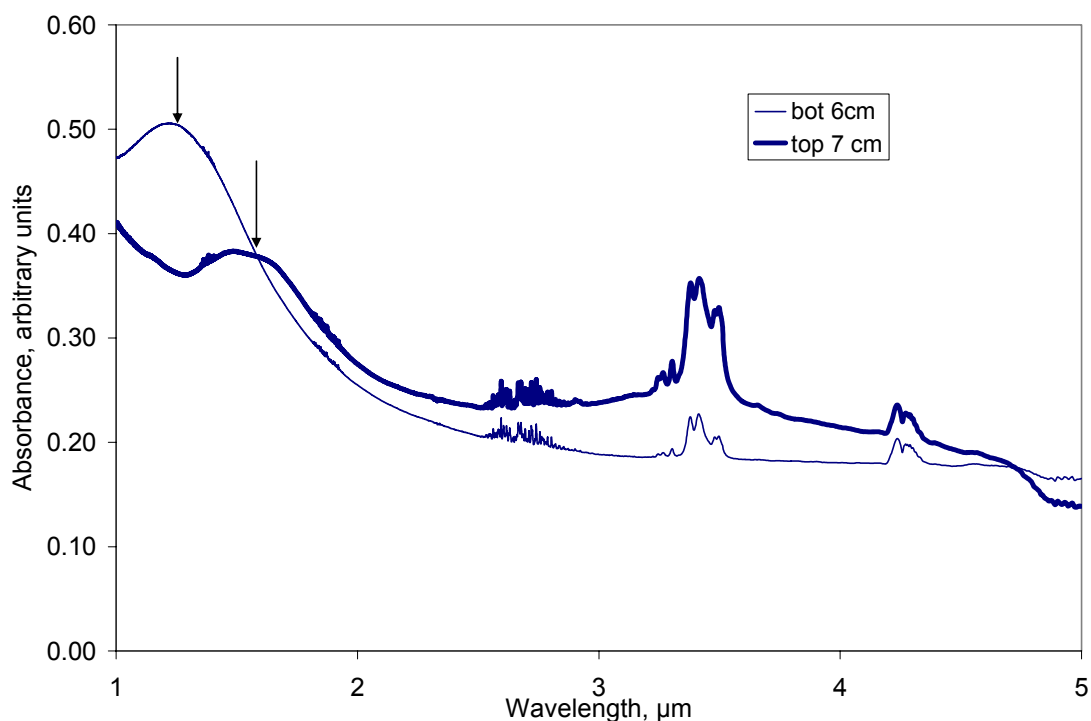


Figure IV.8 FTIR spectra from different points of an Ag/1 wt% PS, 1 mm bore sample showing the same trend in variation in film thickness as seen in the previous figure. The layer thickness at the top of the sample (the inlet end) is thicker than the bottom. The thickness at the bottom of the sample (the outlet end) was also very close to the thickness of the longest, middle section of the sample (not shown). The thickness variation from top to bottom for this sample is 28% which can be calculated from the data in the figure. At the top, the layer thickness is $0.307\ \mu\text{m}$ and at the bottom, the thickness is $0.240\ \mu\text{m}$.

Figures IV.7 and 8 show two important trends: (1) the polymer layer is thicker at the top end than at the bottom of samples, and (2) the polymer layer is approximately the same

thickness for approximately 90% of the length (the entire sample except for the top 10%).

In order to minimize the variation in thickness during loss measurements, several centimeters from the top end and a few centimeters from the bottom end were trimmed.

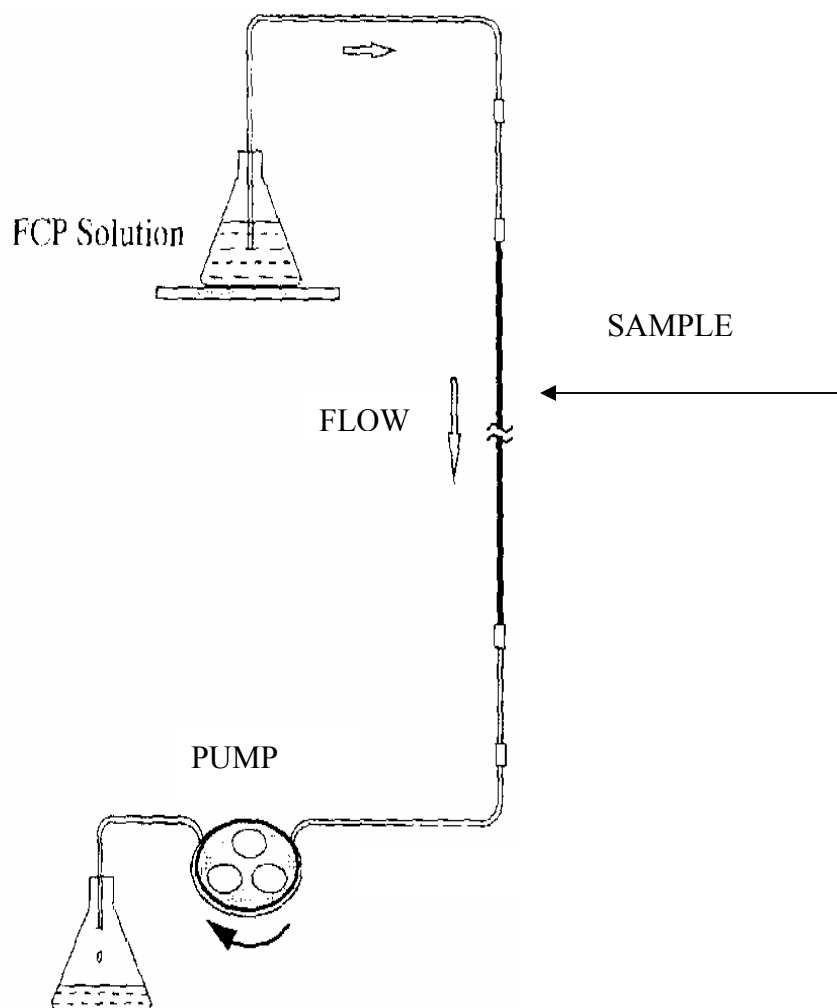


Figure IV.9[5] This is a schematic of the FCP deposition in which the solution is “pulled” through the WG. It is clear that the solution is “pulled” through the sample since the pump is position after the sample while the coating solution is before the sample. In the DLPD process, both the coating solution and the pump are positioned before the sample.

Solvent evaporation rate has a significant impact on the thickness of the layer and surface roughness. As the solvent evaporates, the polymer chains simultaneously contract until a

concomitant increase in viscosity makes further contraction impossible.[24] The extent of this contraction determines the film thickness and thickness uniformity. It has also been shown that the surface roughness increases when the rate of evaporation of the solvent is increased.[9,24] The rate of solvent evaporation is controlled by the atmosphere used during drying. The gas composition (typically N₂, air or solvent vapor), the flow rate of the gas through the sample, and the drying temperature can be chosen to produce a smooth, uniformly thick layer.[5] The usual drying procedure following the DLPD process is to flow air through the hollow core of the sample until the layer is dry at room temperature. The velocity of the air can be controlled with a flow controller. Obviously when there is flowing air, the solvent evaporation rate is higher than when there is no flow. The higher solvent evaporation rate results in the formation of a thinner layer because there is less time for contraction of the polymer chains into more voluminous configurations.[24] Therefore, the extended and well-spaced chains of lower concentration samples are the configuration that remains, resulting in a thinner film. Hence, the sample dried with air flowing resulted in a thinner layer than when there was no flow at all through the sample.

Figure IV.10 compares three different drying conditions for the same deposition solution. The samples were approximately 40 cm long and the bore size was 750 μm . One sample was dried horizontally on a countertop in the ambient room atmosphere with no air flowing. To ensure it was completely dry before characterization, it was allowed to dry overnight. The second sample had air flowing through it for one minute while hanging vertically, and then it was laid on a countertop to dry for two hours. The third sample

was hanging vertically while the air was flowing around the sample horizontally. It can be seen in Figure IV.10 that the layer formed in the sample in which air was flowing (at ambient atmosphere) for one minute was thinner than those in which no air was flowing down the WG axis. Of the two thicker samples, the WG with the air flow perpendicular to the axis was thicker than the other sample. This is probably due to the fact that the perpendicular flow made the release of solvent vapor from the sample more difficult. Thus the evaporation rate was slower. The thicknesses were calculated using Eq. I.7 and are given in Table IV.6.

One sample that was dried with no air flowing through it was also sectioned. The thickness of the sample was found to be uniform throughout the length, unlike the flowing air dried sample. This uniformity was seen in multiple samples dried in this way.

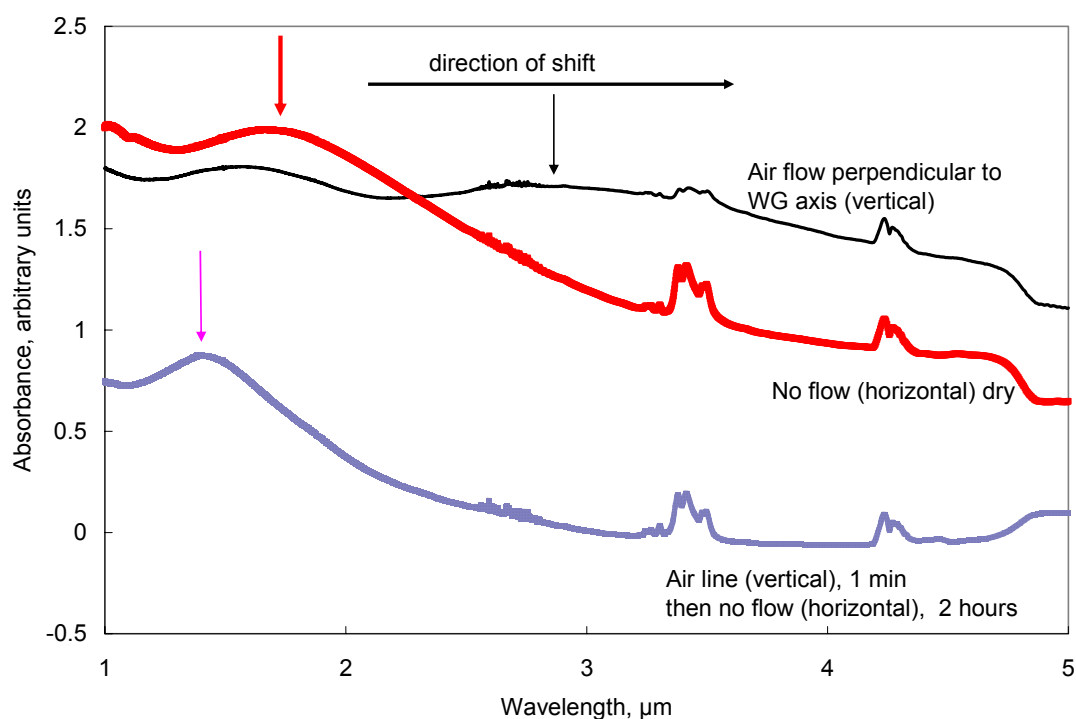


Figure IV.10 The change in thickness for drying conditions can be seen. Here the samples are Ag/1 wt% PS and 750 μm bore with a flow rate of 5.6 mL/min. The fact that the primary peak is at a shorter wavelength for the sample dried with air flowing for one minute than the other two samples indicates that the layer is thinnest. The sample of intermediate thickness was dried with no air flowing through the core. The sample was laid on a countertop in the lab and allowed to dry in the ambient atmosphere at room temperature. The sample with the thickest layer was dried in a chemical hood in which the air flow was perpendicular to the axis of the WG, the sample was vertical. The actual thicknesses are given in Table IV.6 for comparison.

Table IV.6 PS thickness for different drying conditions (data from Figure IV.10)

Drying Condition	Layer Thickness (μm)
Flowing Air, vertical – 1 minute No flow, horizontal	0.285
No flow, horizontal	0.347
Flowing air perpendicular to WG axis (chemical hood)	0.585

Profilometry was also performed on samples prepared on glass slides instead of tubing, to facilitate the measurement of film thickness since the equipment is better suited for measurements with films on planar substrates. The roughness slides coated with 1wt% PS alone, Ag/ 2 wt% PS and Ag/2 wt% PS/ CdS samples were measured. For Ag coated samples, the standard DLPD process was used (deposition time was 60 minutes) and the slide was placed in the stream of the mixed solutions to imitate the DLPD as much as possible. Dip coating was used to coat the samples with PS using either a 1 or 2 wt% PS solution. The slides were placed in a covered container so that the solvent evaporation rate could be controlled and in line with the approach used for HWs. To deposit CdS, the standard DLPD process was used (deposition time was 72 minutes) and the slide was placed in the stream of the mixed solutions.

The results are listed in Table IV.7. The roughness values are the arithmetic average of roughness measurements obtained as line profiles by a stylus over scan widths of 2 mm.

From the data in the table, a thicker PS layer is rougher than a thinner PS layer. The increase in roughness with increasing PS concentration in the deposition solution is likely due to the more closely spaced, more coiled chains creating narrower regions of solvent escape than in a less concentrated solution. The narrow regions may also be irregularly spaced. Thus, solutions of higher PS concentration produce rougher samples than lower PS concentration samples. Also, an underlying Ag layer further increases the roughness, as previously observed.[14] The deposition of a dielectric layer on the 2 wt% PS layer (CdS in this case) increased the roughness to three times the Ag/2 wt% PS value. This large increase in roughness may be caused by the interaction that the basic CdS deposition solution has with the nonpolar polymer substrate layer.

Table IV.7 Profilometry Results of PS alone and Ag/PS/CdS Samples (on glass slides)

Sample	Roughness (nm)
1 wt% PS alone	25
2 wt% PS alone	45
Ag/2 wt% PS	80
Ag/2wt% PS/CdS	240

IV.C.2. PS Loss Measurements and Discussion

The straight loss for the CO₂ and Er:YAG wavelengths were measured for single layer Ag/PS samples using the cutback method. The CO₂ results are shown in Figure IV.11. The CO₂ loss measurements were performed using an MPB cw CO₂ laser with a maximum power of approximately 18 W. Less than 0.5 W were used for these measurements. ZnSe lenses were used to focus the beam into the WG. The cutback lengths used in these measurements were 25 cm because of the high loss measured at this wavelength. The losses were approximately fifty times greater than the theoretical values for 10.6 μm . The PS layer absorption at this wavelength (shown in Figure IV.2) is significant. An exact value at 10.6 μm was not available because it is generally accepted that PS is more appropriate for use in the visible and near IR regions. Since the calculations made using equations presented in Chapter II do not include the material absorption (extinction coefficient), the calculated loss makes this material seem more promising than it actually is.

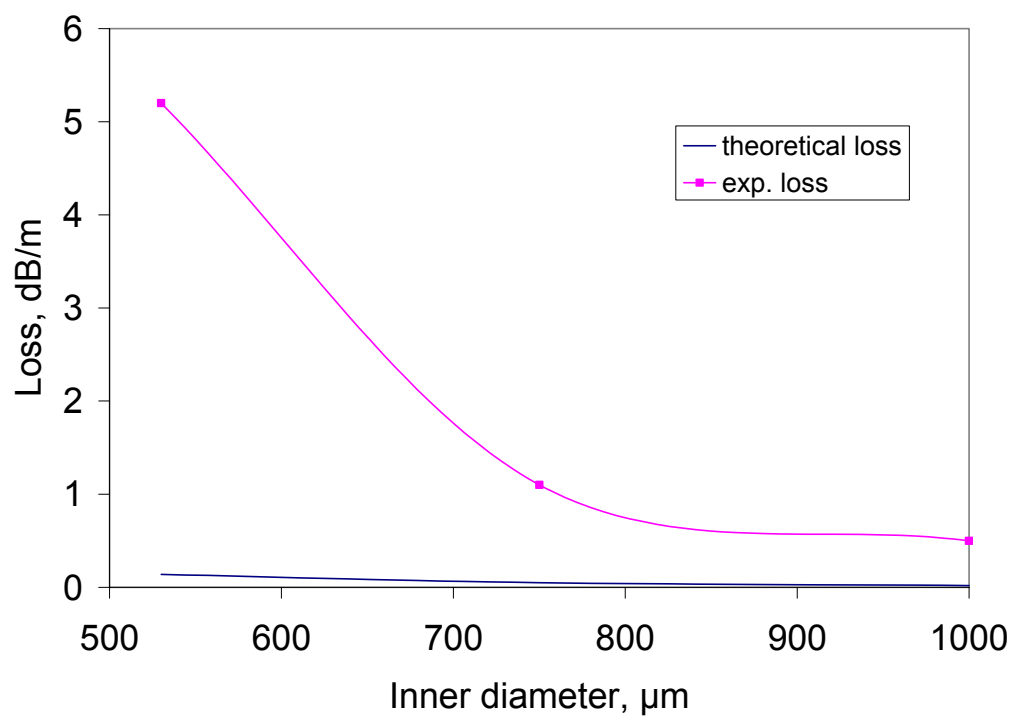


Figure IV.11 Cutback losses for Ag/1 wt% PS samples for three different bore sizes (530 μm, 750 μm, and 1,000 μm) using a cw CO₂ laser.

The Er:YAG loss measurements are shown in Figure IV.12. The loss at the Er:YAG wavelength was measured using two different sources. First, a multimode pulsed Er:YAG laser with a maximum power of 8 W was used as the source and either a 5.5” focal length CaF₂ lens or a 2.4” focal length CaF₂ lens was used to couple the light into the WG. The losses measured with the laser are very much higher than the theoretical values. The large difference between the theoretical values and the experimental values were surprising because the FTIR spectra indicated that the samples should be low loss at 2.94 μm . The power values were in the milliwatt range and the laser was later found to be in need of repair. This set of measurements is not accurate. The second set of loss measurements was done using an FTIR. The cutback method was used to calculate the loss at the Er:YAG wavelength from the spectra. Equation IV.1 shows the equation used to calculate the loss.

$$\alpha = (10/L) * (A_{\text{short}} - A_{\text{long}}) \quad (\text{IV.1})$$

Alpha, is the loss in dB/m, L is the difference in length between the short piece and the long piece and A is the absorbance value from the FTIR spectra.

These measurements yielded much lower loss values than the values from the laser. This improvement is likely due to the careful use of launch conditions for the HE₁₁ mode. Also, slightly shorter lengths (samples were approximately 0.5 m long) were used to measure the loss with the FTIR. The shorter length likely meant less thickness fluctuation than encountered by the laser beam.

The difference between calculated and measured values can be explained for this shorter wavelength by the greater impact surface roughness has on the loss.

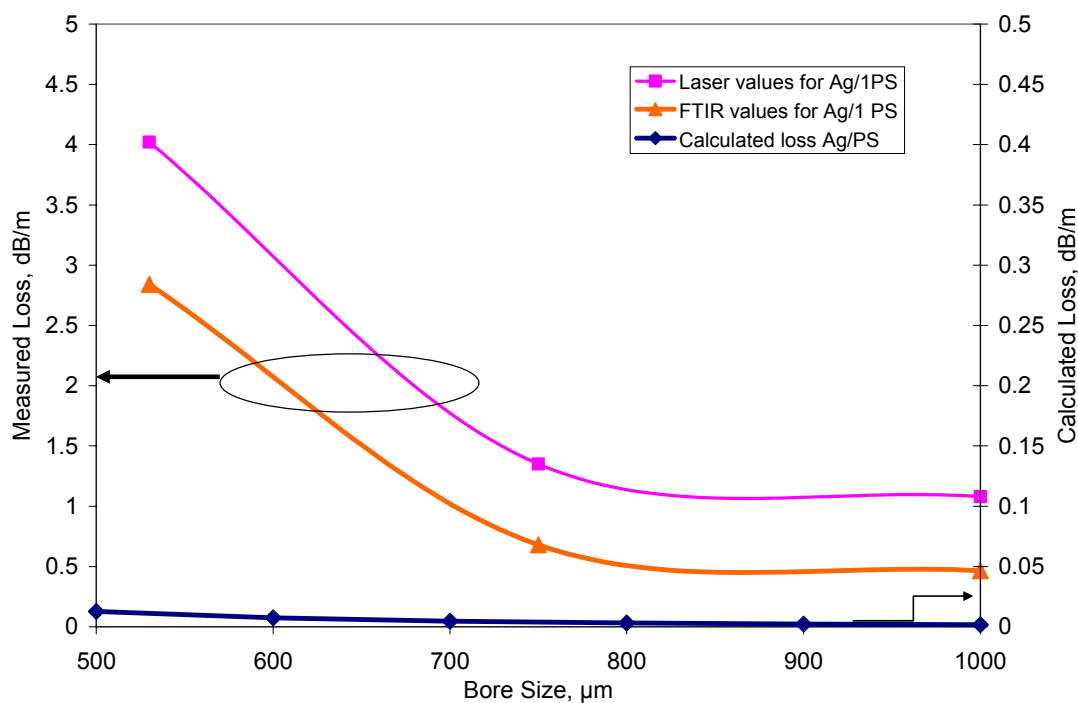


Figure IV.12 Loss values measured for the Er:YAG wavelength with a) a laser as a source and b) FTIR as a source for 530 μm , 750 μm , and 1,000 μm bore waveguides. The theoretical value is also included for comparison. The FTIR measurements were done using shorter samples (approximately 50 cm). The poor modal quality of the laser source was likely the reason for higher loss values, compared to the FTIR results.

To estimate the error in the FTIR loss measurements, the 28% thickness variation between the extreme ends of a 1mm bore sample in Figure IV.8 should be considered. The theory indicates that a dielectric layer thickness variation as high as 40% should not affect loss measurements when a laser is used to measure loss. However, for the loss measurements at $\lambda=2.94\text{ }\mu\text{m}$ made using the FTIR as a source, thickness variation is significant since it changes the position of the features in the spectra. If there is not sufficient trimming or there is excessive thickness variation throughout the sample, then these measurements would vary by 28% or more.

The length of the tubing during deposition and drying would also affect the loss values measured because the deposition and drying conditions would change. More specifically, the interaction time between the deposition solution and the Ag layer would be changed and the rate of solvent evaporation would be affected. The interaction time between the deposition solution and the Ag layer is important because the solvent is a critical component that dictates how well the Ag layer is wetted by the solution. If there is a longer length to be coated, a greater amount of the solvent would be consumed, which would change the deposition condition for the lower (closer to the bottom) portion of the sample. The drying condition would similarly be changed because more solvent vapor would need to be removed from the same size opening.

There are several factors to consider when reproducibility is considered. Since the factors are very much interdependent, exactly reproducing results from Ag/PS requires

each step of the process to be precisely followed. Very similar results can be obtained repeatedly reasonably easily.

IV.D. Conclusions

PS is not a particularly attractive material for use at longer wavelengths. There are many wavelengths of high absorption and there are many wavelengths of lower but still significant absorption as seen in the FTIR PS reference spectrum and as indicated by the loss measurements done here at 10.6 μm .

The loss values measured during this project at the Er:YAG wavelength indicate there is potential for PS at this wavelength. Table IV.8 compares the loss of a few polymers and AgI at the Er:YAG wavelength. This project produced Ag/PS samples with losses that are approximately 2.5 to 3 times greater than the more studied, widely used materials listed in the table. The most significant factor causing the higher loss is likely surface roughness. If the drying process could be modified to allow for more controlled evaporation, then there could be lower loss at 2.94 μm and other shorter wavelengths of technological importance such as 1.06 μm .

Table IV.8 Comparison of loss values for polymers at 2.94 μm (Er:YAG)

Polymer	Loss (dB/m)	Bore Size (μm)
PS	0.7(FTIR)	750
FCP [5]	2.8	700
PI [8]	0.3	700
COP [9]	0.2	700
AgI	0.33	700

One sample for each bore size was measured for Er:YAG loss values. These loss values are important because they are reference values for future samples. The reproducibility of the loss values for similar PS samples will depend greatly on the processing of the samples. Specifically, polymer batches that produce solutions with the same viscosities, similar ambient conditions (temperature, humidity, etc) and identical drying conditions will be needed to completely reproduce these results. Drying conditions that decrease the surface roughness will likely result in lower loss values.

REFERENCES

1. Graf, R.T., Koenig, J.L., Ishida, H., "Optical constant determination of thin polymer films in the infrared," *Appl. Spect.* **39**(3), pp. 405-408 (1985).
2. Inagaki, T., Arakawa, E.T., Hamm, R.N., et al., "Optical properties of polystyrene from the infrared to the x-ray region and convergence of optical sum rules," *Phys. Rev. B* **15**(6), pp.3243-3253 (1977).
3. Saito, M., Gojo, T., Kato, Y., et al., "Optical constants of polymer coatings in the infrared," *Infrared Physics and Tech.* **36**, pp.1125-1129 (1995).
4. Woollam, J.A., Bungay, C., Hilfiker, J., Tiwald, T., "VUV and IR spectroellipsometric studies of polymer surfaces", *Nuclear Instruments and Methods in Physics Research B*, **208**, pp. 35-39 (2003).
5. Wang, Y., Hongo, A., Kato, Y., et al., "Thickness and uniformity of Fluorocarbon polymer film dynamically coated inside silver hollow glass waveguides," *Appl. Opt.* **36**(13), pp.2886-2892 (1997).
6. Kato, Y., Osawa, M., Miyagi, M., "Transmission characteristics of polyimide-coated silver hollow glass-waveguides for medical applications," *Proc. SPIE* **2328**, pp.16-21 (1994).
7. Hongo, A., Miyagi, M., Kato, Y., et al., "Fabrication of dielectric-coated silver hollow glass waveguides for the infrared by liquid-flow coating method," *Proc. SPIE* **2677**, pp. 55-63 (1996).
8. Nemec, M., Jelinkova, H., Kornada, P., et al., "Medical application of 3 μ m delivery waveguide system," *Proc. SPIE* **6083**, pp.60830M1-9 (2006).
9. Shi, Y-W., Matsuura, Y., Iwai, K., et al., "Infrared hollow optical fibers and their applications in medicine," *Proc. SPIE* **5449**, pp.298-306 (2004).
10. Nakazawa, M., Shi, Y-W., Matsuura, Y., et al., "Hollow polycarbonate fiber for Er:YAG laser light delivery," *Opt. Lett.* **31**(10), pp.1373-1375 (2006).
11. Ho, W-D., Ma, C-C.M., "Mid-infrared reflectance of silicone resin coating on metal substrates:effect of polymeric binders' absorption," *Infrared Physics and Tech.* **38**, pp.123-131 (1997).
12. Iwai, K., Shi, Y.-W., Miyagi, M., et al., "Hollow infrared fiber with an inorganic inner coating layer with high durability," *Proc. SPIE* **6433**, pp.64330L1-7 (2007).
13. Alaluf, M., Dror, J., Dahan, R., Croitoru, N., "Plastic hollow fibers as a selective infrared radiation transmitting medium," *J Appl. Phys.* **72**(9), pp.3878-3883 (1992).

14. George, R., New dielectric thin film coatings for Ag and Cu coated hollow infrared waveguides, Rutgers University thesis, 2004.
15. Sharma, S.K., Sharma, V.K., and Tripathi, K.N., "Fabrication and Characterization of Multilayer Waveguide for Intergrated Optics," *J Nonlinear Optical Physics and Materials*, **11**(2), pp. 173-178 (2002).
16. Diop, M., Maurin, G., Tork, A., et al., "Novel processing technique to fabricate a three-dimensional silver-polystyrene photonic bandgap crystal," *Opt. Eng.* **41**(8), pp.1943-1946 (2002).
17. Jung, C., Rhee, B.K., "Simultaneous determination of thickness and optical constants of polymer thin film by analyzing transmittance," *Appl. Opt.* **41**(19), pp. 3861-3865 (2002).
18. Caudhill, S.E., Grubbs, W.T., "Interferometric measurements of refractive index dispersion in polymers over the visible and near-infrared spectral range," *J of Appl. Polymer Sci.* **100**, pp.65-72 (2006).
19. Parres, F., Sanchez, L., Balart, R., et al., "Determination of the photo-degradation level of high impact polystyrene (HIPS) using pyrolysis-gas chromatography-mass spectrometry," *J Anal. Appl. Pyrolysis* **78**,pp.250-256 (2007).
20. Nagamura, T., Sasaki, T., "All-optical parallel switching by the use of guided wave geometry composed of a thin silver film and a polymer think film containing organic dye," *Proc. SPIE* **3466**, pp.212-221 (1998).
21. Du, H., Xu., G.Q., Chin, W.S., et al., "Synthesis, characterization, and nonlinear optical properties hybridized CdS-polystyrene nanocomposites," *Chem. Mater.* **14**, pp.4473-4479 (2002).
22. BASF Product Information 2004 for BASF PS 148G and INEOS Styrenics Product Information for 147F.
23. Heimenz, P.C., *Polymer Chemistry*, Marcel Dekkel, New York, 1984.
24. Zhao, J., Jiang, S., Wang, Q., et al., "Effects of molecular weight, solvent and substrate on the dewetting morphology of polystyrene films," *Appl. Surf. Sci.* **236**, pp. 131-140 (2004).
25. Brandrup, J., Immergut, E.H., *Polymer Handbook*, Wiley Interscience, New York, 1989.
26. Poh, B.T., Ong, B.T., "Dependence of viscosity of polystyrene solutions on molecular weight and concentration," *Eur. Polymer J.* **20**(10), pp.975-978 (1984).

27. Gopal, V., New dielectric coatings for low-loss hollow glass waveguides and bundles, Rutgers University thesis, 2003.

Chapter V. PS in a Multilayer Dielectric HGWs

V.A. Introduction

As discussed in Chapter 2, increasing the number of dielectric layers on a metallic layer increases the reflection and thereby decreases the loss of a HGW. For this reason, the deposition of a second dielectric on the PS layer was attempted in this project. Modeling of the attenuation of single and multilayer systems using PS/CdS, and PS/PbS as dielectric pairs are shown in Figures V.1 and V.2. The optimal thickness for each layer for 1,2 and 3 dielectric layers, as determined by the modeling software, are shown in Table V.1.[1] Significant reduction in loss can be seen for the two and three-layer structures at the Er:YAG and CO₂ wavelengths. The greatest total reduction and reduction per added layer is obtained in the PbS/PS pairing. This is because there is a larger index contrast between PS/PbS than there is between PS/CdS.

The modeling software is used to predict the degree to which a multilayer coating will reduce the loss in a hollow waveguide. For this project, the software was used to indicate an approximate optimal thickness of each layer in a multilayer and to generate data that was used to create attenuation spectra like those in Figures V.1 and 2. The software is able to calculate the amount of reflection and optimal thickness by using the Fresnel equations for many iterations. These calculations are made possible by an accompanying database of optical constants for many metallic and dielectric materials that can be expanded by the user.[3]

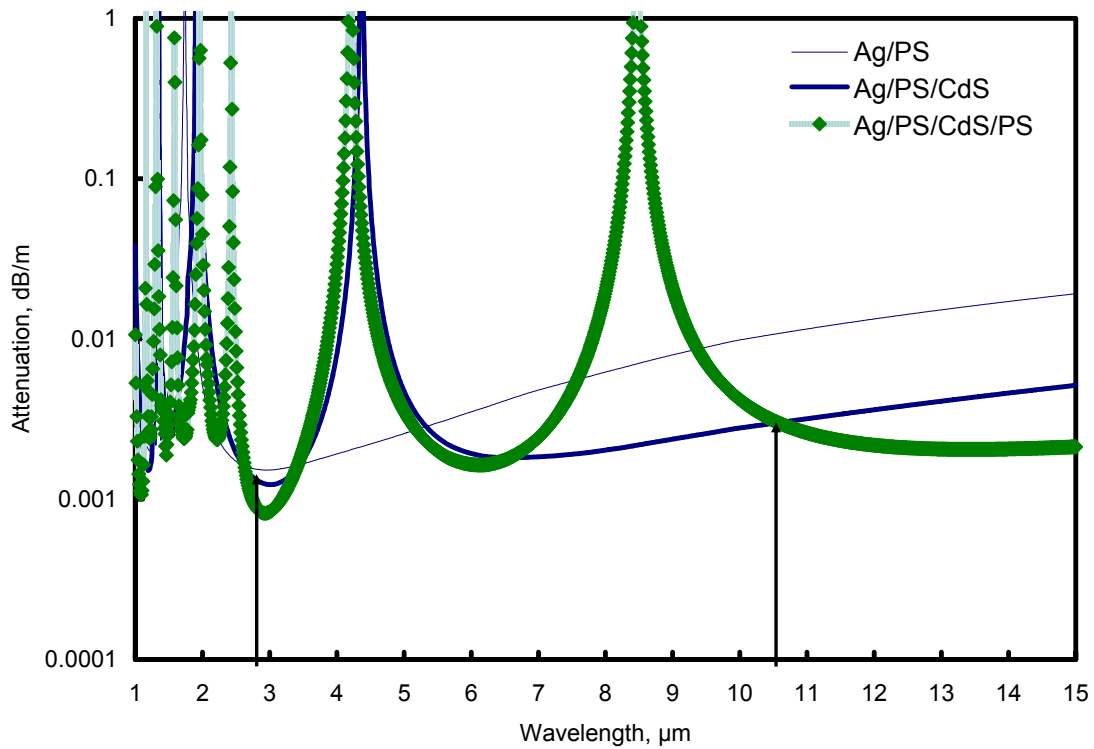


Figure V.1 [1] Modeling showing the decrease in attenuation from that of a single layer (Ag/PS) to that of a multilayer coating (Ag/PS/CdS and Ag/PS/CdS/PS) in a HGW at 2.94 μm and 10.6 μm. Both the Er:YAG (2.94 μm) and CO₂ (10.6 μm) wavelengths are indicated by the vertical lines.

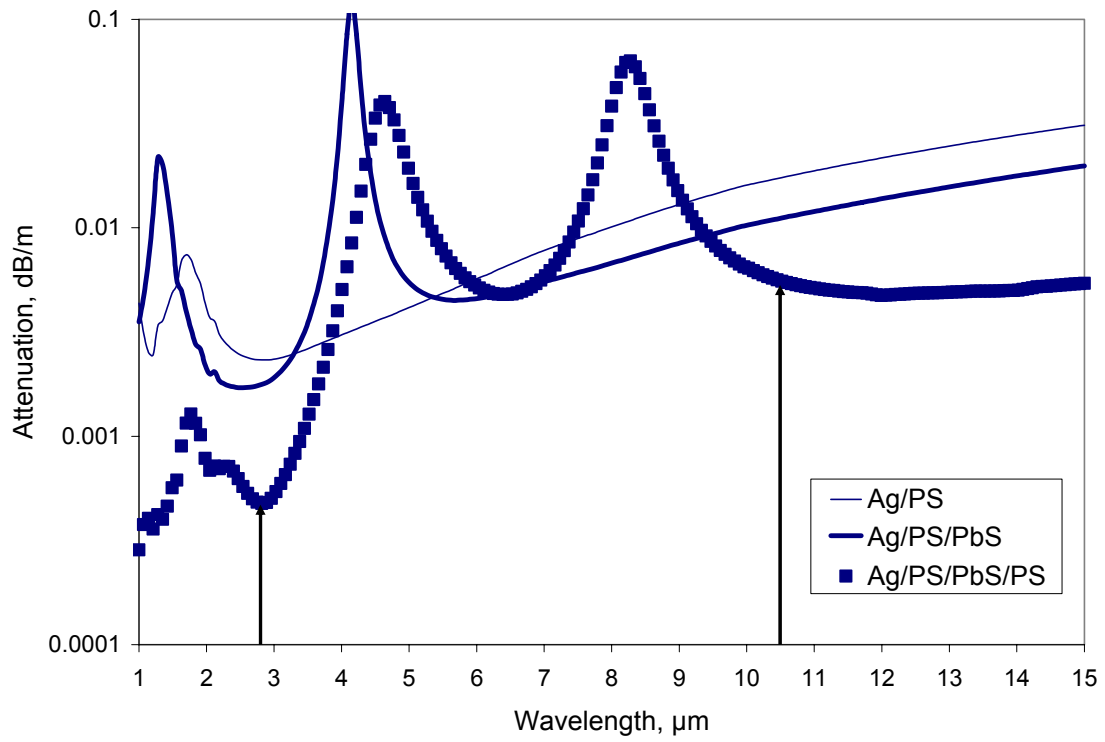


Figure V.2 [1] Modeling showing the decrease in attenuation from that of a single layer (Ag/PS) to that of a multilayer coating (Ag/PS/PbS and Ag/PS/PbS/PS) in a HGW at 2.94 μm and 10.6 μm .

Table V.1.[1] Calculated optimal thickness for 1,2 and 3 layer systems at 2.94 μm

Material Pair Index Contrast	Optimal Thickness(μm) 1 layer (Ag/PS)	Optimal Thickness(μm) 2 layers(Ag/PS/CdS or PbS)	Optimal Thickness(μm) 3 layers(Ag/PS/CdS or PbS/PS)
CdS/PS 1.45	0.332	0.607/ 0.099	0.607 / 0.357 / 0.383
PbS/PS 2.76	0.320	0.330/ 0.062	0.330 / 0.205 / 0.407

The metal sulfides were deposited on Ag/ 2 wt% PS samples because layers made from 2 wt% PS/toluene solutions were able to endure contact with the coating solutions for the required amount of time. When deposition of CdS was attempted on a layer formed from a 1wt% PS solution, the PS layer was dissolved and was replaced by a layer of CdS that eventually formed, as evidenced by FTIR spectra. The FTIR spectra for before and after CdS deposition on PS are shown in Figure V.3. This shift of the primary peak to a shorter wavelength after CdS deposition indicates some of the PS layer has been removed. The primary peak of the pre CdS deposition curve indicates a total PS film thickness of 0.518 μm . The primary peak of the post CdS deposition curve indicates a total film thickness of 0.107 μm . This is a significant decrease in thickness. The presence of CdS is confirmed by the lack of intrinsic PS absorption peaks. Based on the fact that the sample is pink (rather than the characteristic yellow of CdS) when light is

shone through it and that the total (PS and CdS) film thickness is $0.107\text{ }\mu\text{m}$ with some thickness due to the underlying PS layer, the CdS layer is thinner than what is expected based on the kinetics for CdS deposition on Ag. On an Ag layer, the film growth rate is $0.09\text{ }\mu\text{m/hour}$. [2]

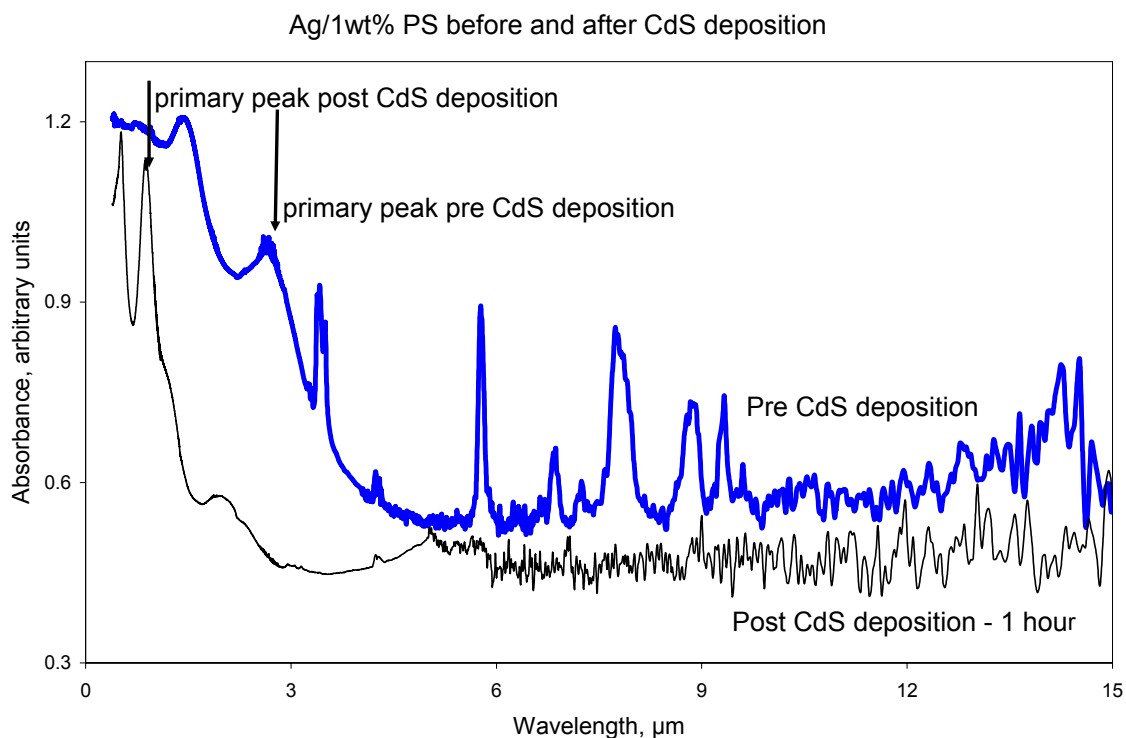


Figure V.3 FTIR spectra of a Ag/1 wt% PS sample before and after CdS deposition. The post-CdS deposition FTIR spectrum has a primary peak at shorter wavelength than the primary peak in the pre-CdS deposition spectrum. This shift of the primary peak to a shorter wavelength indicates some of the PS layer has been removed. The primary peak of the pre CdS deposition curve indicates a total film thickness of 0.518 μm . The primary peak of the post CdS deposition curve indicates a total film thickness of 0.107 μm .

V.B. Processing

To deposit either cadmium sulfide (CdS) or lead sulfide (PbS), the PS layer was first dried and then the appropriate solutions were pumped through a Ag/PS sample, similar to Figure I.1 (see Chapter 1).

The compositions of the solutions used for CdS deposition on PS were taken from Gopal.[2] For CdS deposition on a PS layer, the following solutions are vigorously mixed:

3.94 g cadmium nitrate - $\text{Cd}(\text{NO}_3)_2$ / 875 mL H_2O + Solution 1
125 mL ammonium hydroxide

6.34 g thiourea - $\text{SC}(\text{NH}_2)_2$ / 1000 mL H_2O . Solution 2

All water used in all depositions is distilled and deionized.

In making Solution 1, water and cadmium nitrate were mixed with a magnetic stir bar until all the cadmium nitrate dissolved. Then the ammonium hydroxide was added to complex the cadmium (Cd^{2+}) ions. The thiourea was similarly dissolved alone in 1000 mL of water. The pump rate was 7.3 mL/min for a 530 μm bore size sample.

The solutions for PbS deposition on PS have the same concentrations as the solutions used to coat silver to make a single layer dielectric HGW, described in Chapter III.

V.C. Experimental Results and Discussion

V.C.1. PS as the low index dielectric material in an additive stack with CdS

A thin layer of CdS forms using the solutions previously described with a growth rate shown in Figure V.4. The optical constants of CdS are shown in Figure V.5. The CdS growth rate shown is based on calculations using FTIR spectra for the layer thickness of the CdS film, deposited on Ag/2wt% PS, at different times. The initial delay in the growth rate is likely due to the wetting behavior of the basic, aqueous CdS solutions on the PS nonpolar polymer layer.

The CdS film thicknesses obtained, as shown in Figure V.4, are in the range of the required thickness for a two-layer Ag/PS/CdS sample optimized for Er:YAG transmission (for a 2 layer coating, the design thickness for the CdS layer is $0.099\text{ }\mu\text{m}$ from Table V.1), as determined by the modeling software. It is unlikely, based on the results obtained in this project, that the CdS design thickness for a three layer WG which is $0.357\text{ }\mu\text{m}$ from Table V.1 would be achievable. Still, this project has proven that PS/CdS multilayers can be fabricated if a starting solution with a concentration of 2wt% PS, rather than 1 wt% PS, is used.

The lack of reduction in loss at $10.6\text{ }\mu\text{m}$ when an additional (third) layer is deposited is shown in Figure V.1. This lack of loss reduction can be explained by (1) the high absorption of PS at that wavelength; and (2) the large surface roughness measured using Ag/PS/CdS samples, given in Table IV.7.

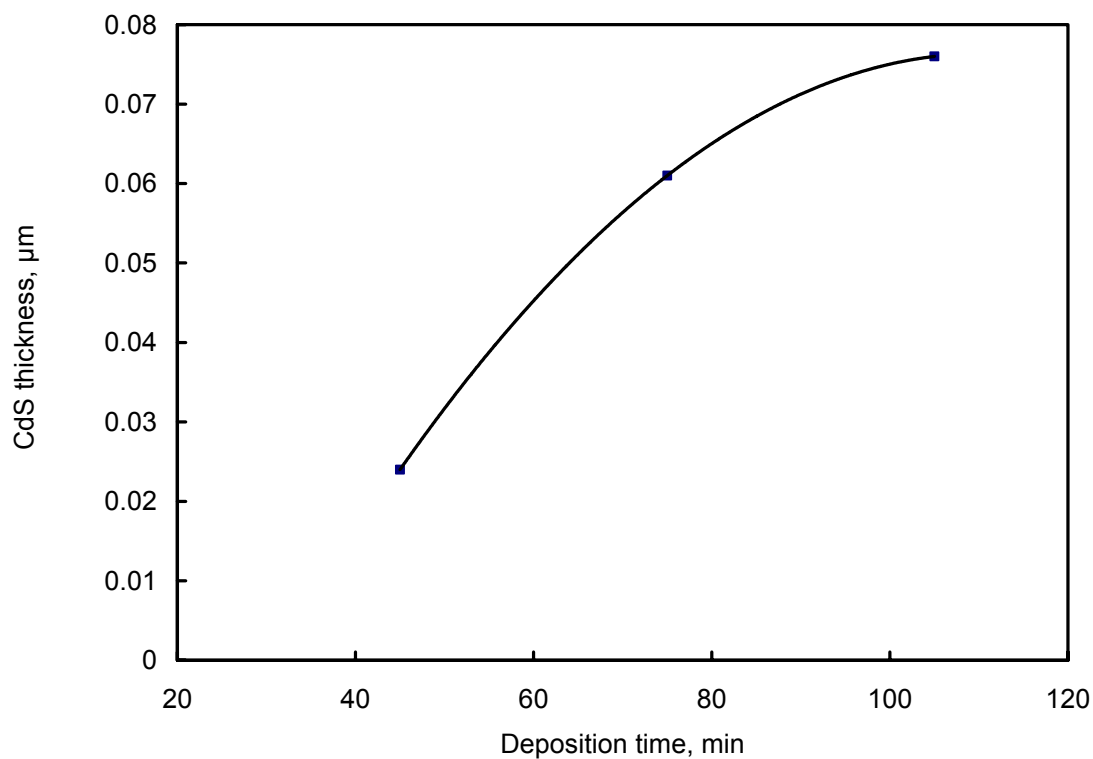


Figure V.4 The growth rate of CdS on a PS surface as a function of time at room temperature. These data were obtained by calculating the layer thickness based on FTIR spectra as described in Chapter 1. The required CdS thickness for a two layer coating (Ag/PS/CdS) is $0.099\ \mu\text{m}$ at $2.94\ \mu\text{m}$, as determined by the modeling software. This figure shows deposition of a CdS layer of approximately this thickness is feasible.

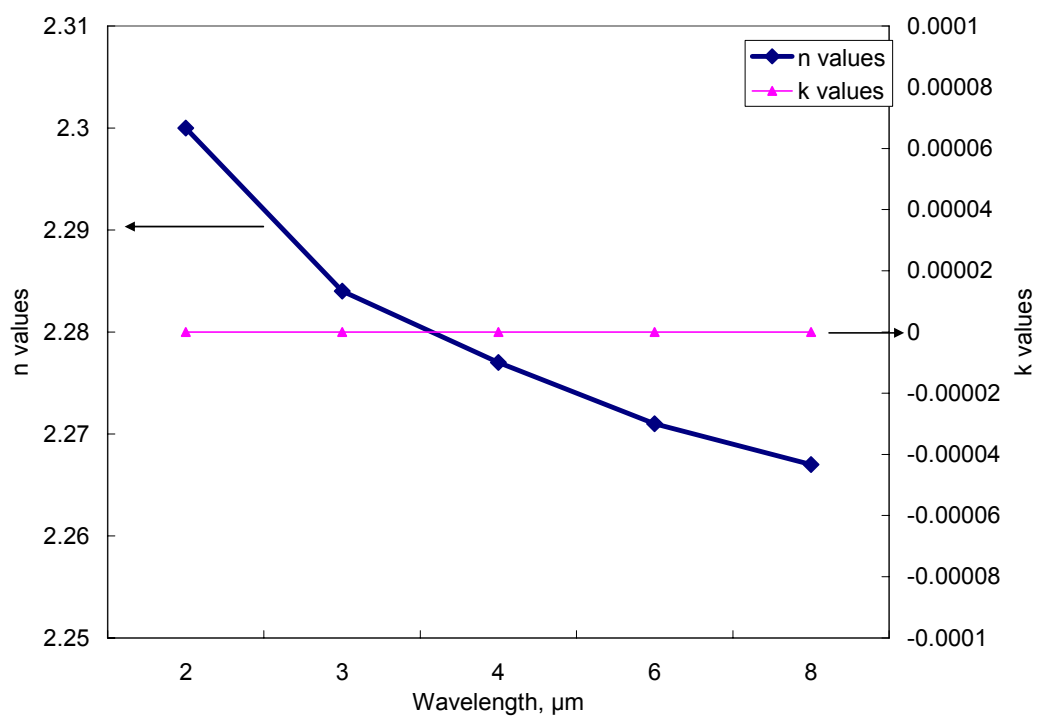


Figure V.5 Optical constants, n and κ , for CdS. [3]

V.C.2. PS as the low index dielectric material in an additive stack with PbS

A thin layer of PbS forms using the solutions previously described with a growth rate shown in Figure V.6. The PbS growth rate shown is based on calculations using FTIR spectra for the layer thickness of the PbS film, deposited on Ag/2 wt% PS samples, measured at different times during the deposition. The same initial delay in the growth rate is seen here as for the CdS deposition on the PS layer. The cause is the same: basic aqueous solutions are wetting a nonpolar polymer surface.

The optical constants of PbS are shown graphically in Figure III.1.

Unlike the CdS/PS pairing, the PbS/PS pairing has a high index contrast of 2.76. This contrast would compensate for the high PS absorption at 10.6 μm and would allow the pair to reduce the loss at both the Er:YAG and CO₂ wavelengths.

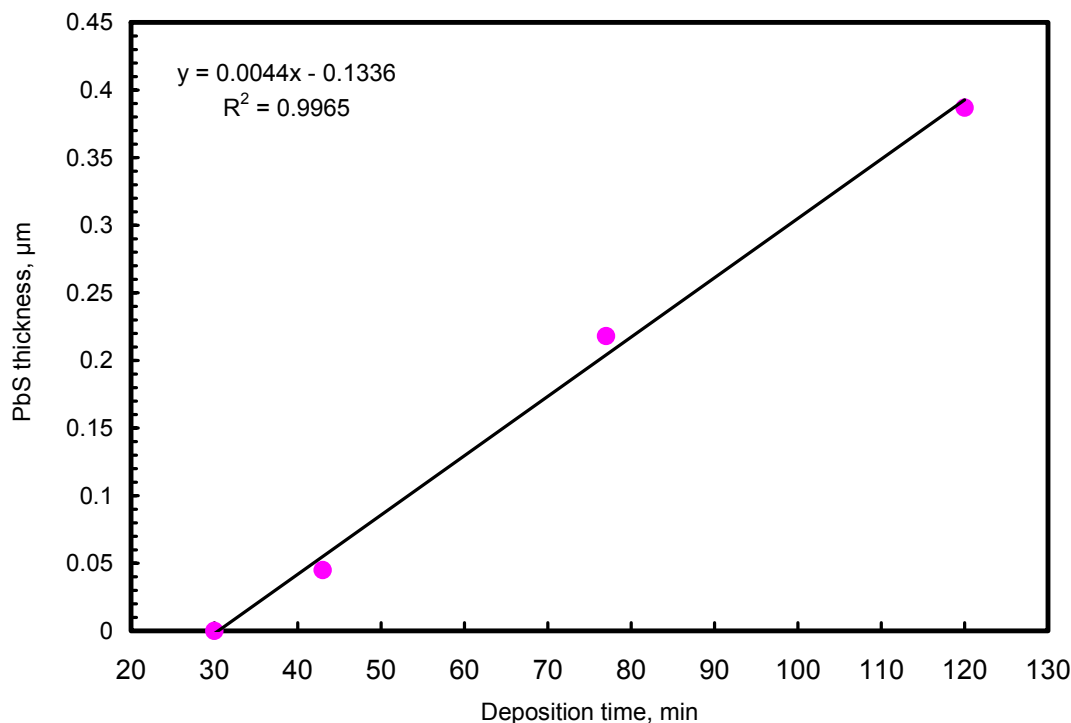


Figure V.6 The growth rate of PbS on a PS surface as a function of time at room temperature. The thickness values were calculated from FTIR spectra collected at different times during deposition. The required PbS thickness for a two layer coating (Ag/PS/PbS) is 0.062 μm at 2.94 μm, as determined by the modeling software. This figure shows deposition of a PbS layer of this thickness is feasible.

Also unlike the CdS/PS pairing, achieving the design thickness for PbS in both a two and three layer coating seems possible for PbS/PS. As seen in Table V.1, the design thickness for PbS in the two layer structure is 0.062 μm, and the design thickness for PbS in the three layer structure is 0.205 μm at 2.94 μm. It is easy to understand why such a thin layer is required for Er:YAG radiation when the absorption behavior of PbS is considered. As shown in Figure III.1, the absorption of PbS is high at 2.94 μm. Hence,

to lower loss at the Er:YAG with the PbS/PS pair, either one or three layers should be used.

The PS/PbS samples described here prove that deposition with this polymer/metal sulfide pairing is possible. These samples were only tests of the possibility of PbS deposition on PS and no loss measurements were made using either laser. Future work should include making a meter long sample and measuring the loss at either 2.94 μm or 10.6 μm or both.

REFERENCES

1. Reflection calculations performed using IMD software by David L. Windt, <http://cletus.phys.columbia.edu/~windt/idl/imd/index.html>.
2. Gopal,V., New Dielectric Coatings for Low-Loss Hollow Glass Waveguides and Bundles, Rutgers University thesis, 2003.
3. Edited by Palik, E.D., *Handbook of Optical Constants of Solids*, Academic Press, New York, 1985.

Chapter VI. Potential Dielectric Materials by DLPD: ZnS/ZnSe and Gold

VI.A ZnS/ZnSe Introduction

Zinc selenide (ZnSe) and zinc sulfide (ZnS) have been successfully deposited using sputtering[1], electron beam[1] and CVD[2] techniques and especially chemical bath deposition (CBD).[1, 3-13] The goal here was to deposit one or both materials using DLPD. Both materials can be deposited as thin films for low absorbance at the Er:YAG, CO and CO₂ wavelengths. Ag/ZnS and Ag/ZnSe waveguides have shown that a high power single mode output beam, appropriate for materials processing, is possible even upon bending.[14-16] ZnS is an attractive candidate for use in HWs. ZnS is non-toxic whereas ZnSe and CdS are toxic.[4,15] Therefore, ZnS is good for medical applications that employ the Er:YAG and CO₂ lasers. ZnS is also harder and stronger than ZnSe.[15] In addition ZnS and ZnSe are oxidation resistant in moist environments. The bending loss of Ag/ZnS samples has also been measured on samples made by sputtering and the losses were lower than for Ag/ZnSe and Ag/Ge samples.[14,15] Although the bending losses for Ag/ZnSe HWs are higher than for Ag/ZnS, they are lower than the Ag/Ge loss. Therefore, successfully making either an Ag/ZnS or an Ag/ZnSe waveguide is desirable. The DLPD process would be an efficient, more cost effective way of making these samples than the usual techniques.

The deposition of ZnS and ZnSe as dielectric layers using the DLPD process was attempted because there is great potential for these materials given their excellent optical properties. The optical constants for ZnSe and ZnS from 2 to 20 μm are shown in Figure

VI.1 and Figure VI.2, respectively.[17] ZnS has an extinction coefficient on the order of 10^{-3} for wavelengths up to $13.8\text{ }\mu\text{m}$, while ZnSe has an extinction coefficient on the order of 10^{-4} up to $16\text{ }\mu\text{m}$. Since the usual techniques for making ZnS and ZnSe thin films (CVD and electro-deposition) routinely produce smooth, highly reflective thin films with characteristics similar to the films made using the DLPD process, we attempted to make high quality ZnSe or ZnS films using this latter process. [18-21]

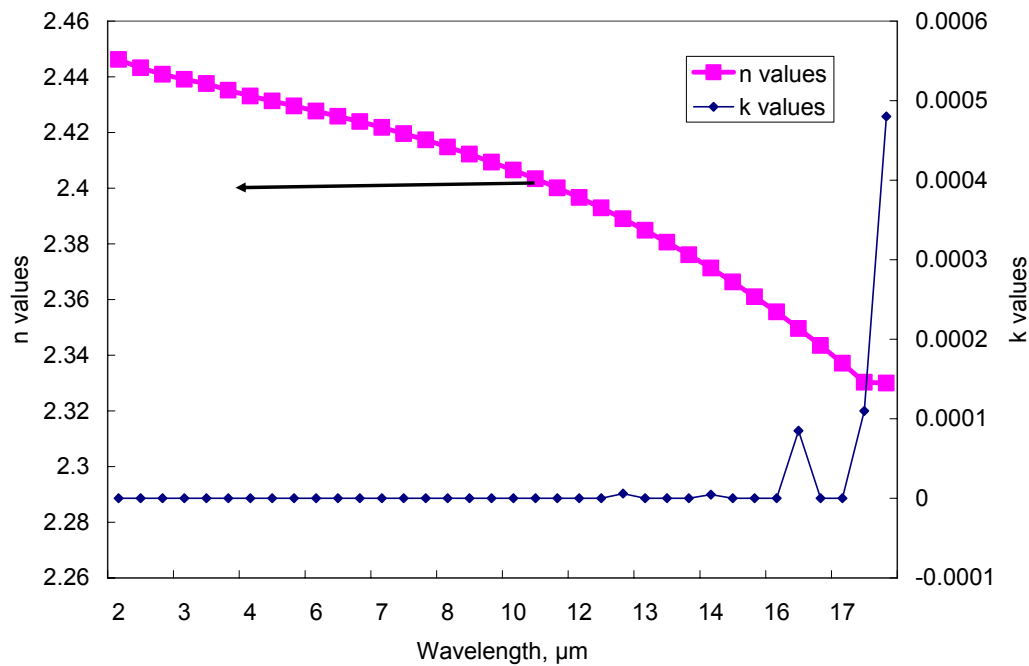


Figure VI.1 Optical constants, n and κ for ZnSe.[17]

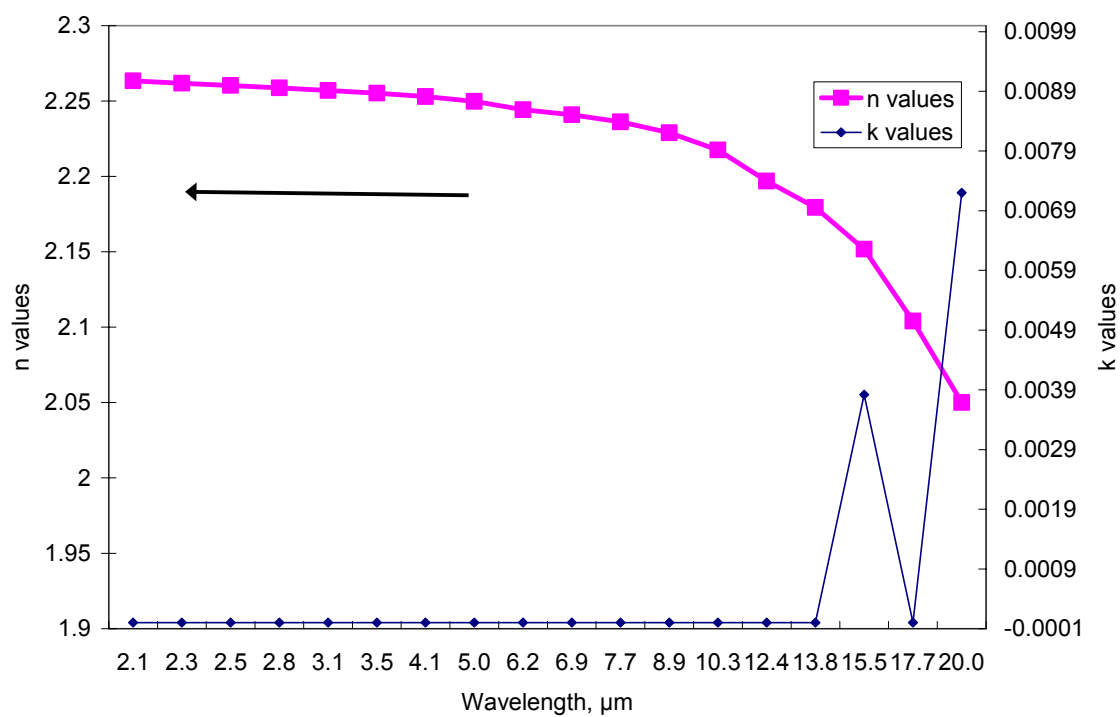


Figure VI.2 Optical constants, n and κ for ZnS.[17]

These new dielectrics may also be more chemically compatible with the high index, non-absorbing PbSe. As can be see in Figure VI.3, PbSe has an index greater than 4.5 for both the Er:YAG and CO₂ wavelengths. The low absorbance at the Er:YAG wavelength allows PbSe to be used an a top layer (most adjacent to the air core) in a WG with an even number of dielectric layers. If PbSe could be deposited successfully with either CdS, ZnS, or ZnSe as the low index material, the index contrast would be still very large (see Table VI.1).

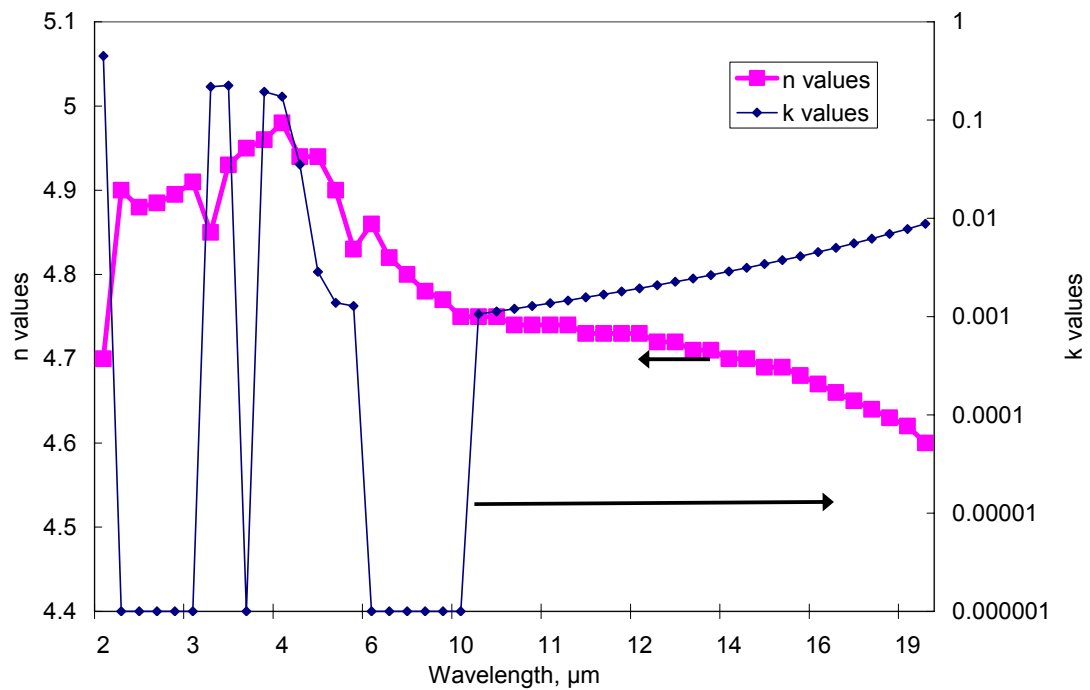


Figure VI.3 Optical constants, n and κ for PbSe.[17]

Table VI.1 Index Contrast between 3 Potential DLPD Low Index Materials and PbSe

[17]

Dielectric Pair	Contrast
ZnS/PbSe	1.99
CdS/PbSe	1.97
ZnSe/PbSe	1.84

VI.B. ZnS/ZnSe Processing

VI.B.1. ZnS/ZnSe Processing – Literature Review

It is much more difficult to deposit optical quality films composed of entirely ZnSe or ZnS using the DLPD process than to deposit CdS.[1,5] In the literature, only a small number of ZnSe films have been produced and these have low purity and poor quality.

The cause of the difficulty is a greater overlap of conditions favorable to the simultaneous formation of ZnS and Zn(OH)_2 than there is for CdS and Cd(OH)_2 . [1] In addition, the deposition parameters are not well understood.[4-6,19] Figure VI.4 shows the conditions of formation of ZnS/ Zn(OH)_2 in contrast to CdS/ Cd(OH)_2 . The availability of the Zn ions in solution can be controlled by complexing agents. The availability of the sulfide ions becomes the determining factor. At lower pH levels, where higher concentration of free Zn ions can be tolerated, hydrolysis of the sulfur source occurs more slowly and more sulfur precursor is needed. Under more basic conditions, the rate of hydrolysis of the sulfur ion source is higher but Zn(OH)_2 is more likely to form, even at lower concentrations of Zn.

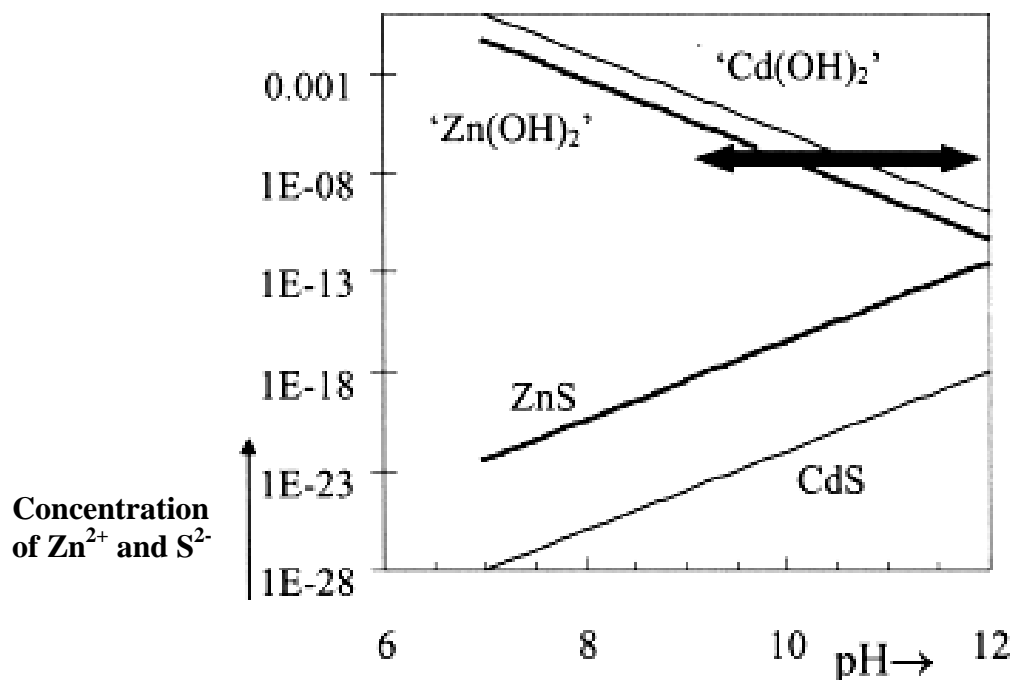


Figure VI.4 A comparison of conditions for which ZnS (and/or Zn(OH)_2) and CdS (and/or Cd(OH)_2) formation occurs. The lines indicate the minimum concentration and pH level at which the compound labeling the line will be formed (for $[\text{S}]$ lower line, for $[\text{Zn}]/[\text{Cd}]$ upper line). This chart shows that the concentration of S^{2-} ions should be $\sim 10^{-23}$ M and Zn concentration should be below .001 M under neutral conditions to form ZnS and not Zn(OH)_2 . The double arrow-headed line indicates the pH level at which successful CdS deposition is performed. This range is not appropriate for ZnS film deposition.[5]

One reason pure ZnSe films are difficult to form is because there is a parallel zinc oxide deposition during the early stages of growth of ZnSe. This results in the undesirable formation of ZnO particles. It has been found that the conductivity of the substrate affects the proportion of ZnO found in the ZnSe/ZnO film. Surfaces with higher conductivity have larger proportions of ZnO than surfaces with lower conductivity.[3] ZnO is not an optical material and its index and transparency are not well known.

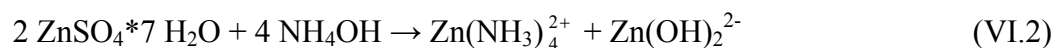
Metal selenides require a selenide ion (Se^{2-}) source. Sodium selenosulphate (Na_2SeSO_3) and selenourea are most common sources. Sodium selenosulphate is a compound that is usually made in the laboratory in small batches near the time the thin film is to be deposited. The chemical reaction occurring is given in Eq. VI.1. In a water bath that is maintained at 90°C , one molarity (1 M) of sodium sulfite (Na_2SO_3) is mixed with a stoichiometric amount of elemental selenium (Se) for one hour. The unreacted elemental Se is filtered off after one hour. An excess of sulfite (SO_3^{2-}) ions should be present in aqueous solutions of either selenourea or selenosulphate because selenium readily reacts with oxygen to form SeO_2 . SeO_2 is a red colloidal form of selenium that will not dissociate (separate into Se and O ions) to release the needed Se^{2-} ions into the solution. [22-24]



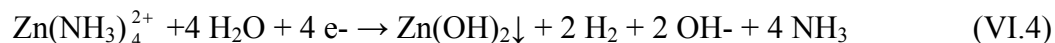
Although its role in ZnSe and ZnS deposition is not clearly understood, hydrazine (N_2H_4) is needed to produce adherent, uniform films whose compositions are predominantly ZnS

(or ZnSe) with minimal amounts of ZnO or Zn(OH)₂. Hydrazine is believed to be involved in both the speciation of Zn and the decomposition of the chalcogen (here S and Se) source which makes the chalcogenide ions more readily available. $[\text{Zn}(\text{NH}_3)_4]^{2+}$ is a complex which forms from a reaction between the zinc precursor, in this case zinc sulfate ($\text{ZnSO}_4 \cdot 7 \text{H}_2\text{O}$) and the pH level adjuster, ammonium hydroxide (NH_4OH), as shown in Eq.s VI.2. The addition of hydrazine affects this complex in two ways. First, hydrazine replaces the NH_3 groups as ligands to the Zn. This hydrazine ligand is less bulky so that the sulphide ion can approach the Zn ion more closely (in chemistry jargon, it presents less steric hindrance). The closer approach facilitates reaction between the ions. Second, with increasing concentration of hydrazine, less free Zn ions are present (which would result due to dissociation of the complex) and, therefore, less $\text{Zn}(\text{OH})_2$ and ZnO particles are formed (Eq.s VI.4 and 5). Hydrazine may also be a bridging ligand that facilitates adsorption of the complex onto the substrate surface. Since the growth rate dramatically increases upon addition of hydrazine, its other role seems to be expeditor of the decomposition of the thiourea or selenourea, making the Se^{2-} or the S^{2-} ions available for reaction.[3,5,12,23]

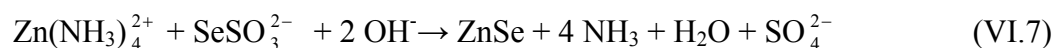
The initial stage of ZnSe film formation, during which both ZnSe and ZnO are deposited, the NH_4OH concentration is lowered and no hydrazine is present. The reaction is described by the following equations [3]:



However, Eq.VI.3 is unlikely to occur, however, due to the low concentration of dissolved oxygen in solution. In aqueous solutions, water is abundantly available and the following reaction is much more likely to occur [3]:



$\text{Zn}(\text{OH})_2\downarrow$ indicates a precipitate of zinc hydroxide is formed. Heterogeneous chemical film growth of mostly ZnSe composition is believed to occur after the initial stage. This second stage begins when a non-conducting surface has been established. The presence of a soluble selenium specie seems to dictate whether the deposition process will occur and to what extent. The reactions leading to ZnSe formation are given by [3]:

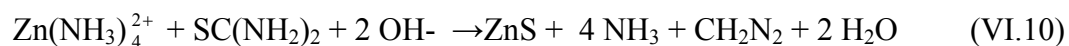
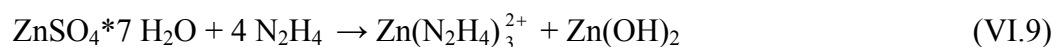
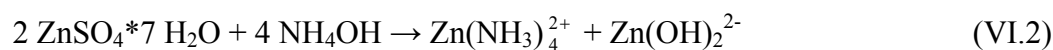


If the selenium ion source is selenourea, instead of sodium selenosulphate and there has been no prior exposure to sulfite ions, then ZnSe is formed by [2]:



The films formed during the second growth interval are less dense but have higher proportions of ZnSe than those made during the first interval in which there is much more ZnO incorporated and more basic conditions.

To form ZnS, solutions containing the zinc precursor, thiourea ($\text{SC}(\text{NH}_2)_2$, (as a sulfur ion source) and one or more complexing agents (ammonium sulfate, $(\text{NH}_4)_2\text{SO}_4$, and hydrazine are common) and a pH level controller (NH_4OH) are mixed. The chemical reaction is as follows [12]:



Since hydrazine is not environmentally-friendly, a non-toxic complexing agent was sought so that deposition of ZnS and the material itself would be non-toxic. In the search for a non-toxic complexing agent, tri-sodium citrate was found. This compound is able to produce ZnSe films that have no ZnO nor $\text{Zn}(\text{OH})_2$ peaks seen in the XRD pattern.[11]

The pH level is also a significant factor in both CBD and DLPD. Lokhande et al. [4,22] found that for $\text{pH} < 7.5$ and $\text{pH} > 13.5$ soluble Zn species (Zn^{2+} and ZnO_2^{2-}) were both present in solution. In the range, $7.5 < \text{pH} < 13.5$, insoluble white $\text{Zn}(\text{OH})_2$ particles were in solution and incorporated in the ZnSe film. Furthermore, $\text{Zn}(\text{OH})_2$ is unavoidable

due to the basic condition of all of the solutions used to date, and the concentration of this specie increases with solution temperature. Thus Zn(OH)_2 particles will likely be included in most of the films because the particles form rapidly in solution, before the solution containing the Se source is introduced so there no competition between the two reactions. These particles, once formed, settle on the substrate surface. They then interrupt film formation and result in a roughness surface of aggregated particles (see Figure VI.5).

Lokhande et al. also found a linear relation, of positive slope, between film thickness and solution temperature up to 70°C , then a negative slope. The negative slope indicates homogeneous nucleation is predominantly occurring, rather than heterogeneous nucleation (negative slope), at higher temperatures. Based on their results, room temperature deposition is appropriate since heterogeneous deposition occurs at lower temperatures.

VI.B.2. ZnS/ZnSe Processing – Experimental

There are many possible solution compositions to be investigated. Three compositions are given here because the resultant FTIR spectra had some features that potentially indicate that film formation may have occurred. The compositions given represent typical solution compositions. All recipes are aqueous solution and used distilled and deionized water.

First, two solutions of 1,000 mL total volume each were used for Recipe A (ZnSe deposition):

10.79 g zinc sulfate

Solution 1

0.495 g ammonium sulfate

8.1 mL hydrazine

Ammonium hydroxide was added until Solution 1 was clear.

0.5625 g selenourea

Solution 2

15 mL hydrazine

The solutions were pumped through the Ag coated silica tubing, using the same DLPD configuration shown in Figure I.1, at a rate of 9 mL/min for 26 minutes at room temperature.

Next, one solution of 500 mL total volume was used for Recipe B (ZnS deposition):

1.29 g zinc sulfate

Solution 1

1.65 g ammonium sulfate

8.1 mL hydrazine

55 mL 30% ammonium hydroxide were added

22 mL hydrazine

0.34 g thiourea are subsequently added.

This one solution was pumped through the Ag coated silica tubing at a rate of 9 mL/min for 69 minutes at room temperature.

Third, two solutions of 500 mL total volume each were used for Recipe C (ZnS deposition):

8.8 g zinc acetate / 500 mL H ₂ O	Solution 1
--	------------

0.75 g thioacetamide / 500 mL H ₂ O	Solution 2
--	------------

The solutions were pumped through the Ag coated silica tubing, as shown in Figure I.1, at a rate of 9 mL/min for 38 minutes at 62 °C. The higher temperature was used in an attempt to quicken the reaction rate.

VI.C. ZnS/ZnSe Experimental Results and Discussion

Figures VI.5-7 show the result of Recipe A, B and C, respectively, for the deposition conditions given. The peaks that can be seen in the FTIR spectra in Figures VI.5-7 indicate no continuous film has been deposited. Most of the peaks are broad and there is not a large difference between the peaks and the valleys. In addition, there is no regular spacing of the peaks. Thus the peaks formed are not interference peaks at all. The narrow peaks belong to an individual specie causing the peak at one wavelength. Two well known peaks that appear in all three spectra are that of CO₂ at 4.2 μm and H₂O at approximately 6.2 μm.

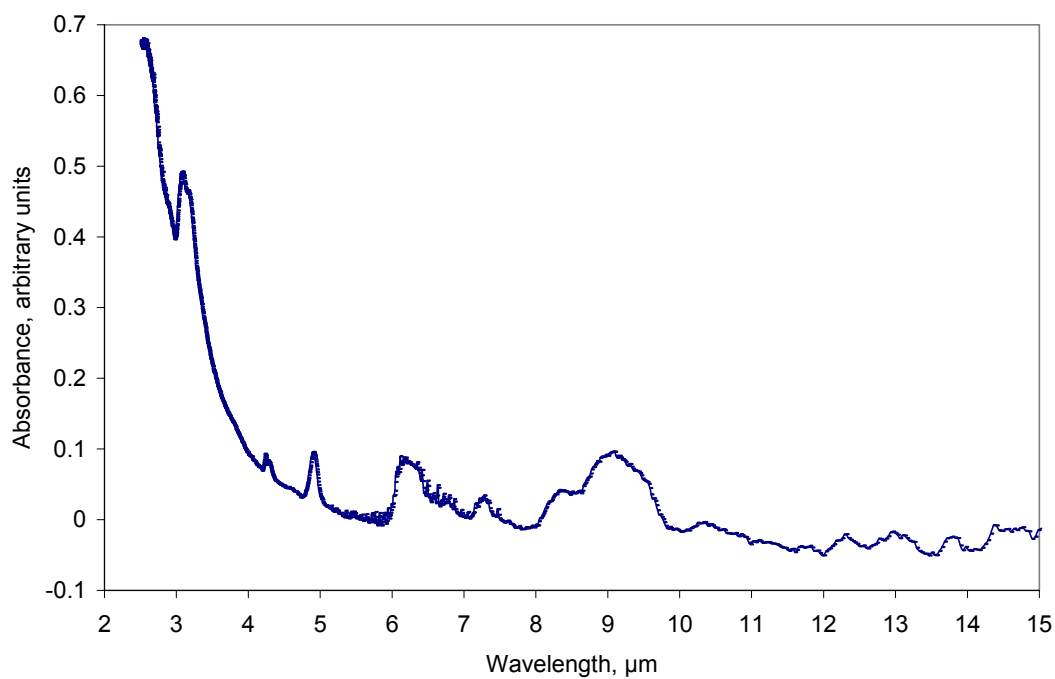


Figure VI.5 An FTIR spectrum of an Ag/ZnSe 2 mm bore size sample made using Recipe A (deposited with a flow rate of 9 mL/min for 26 minutes at room temperature).

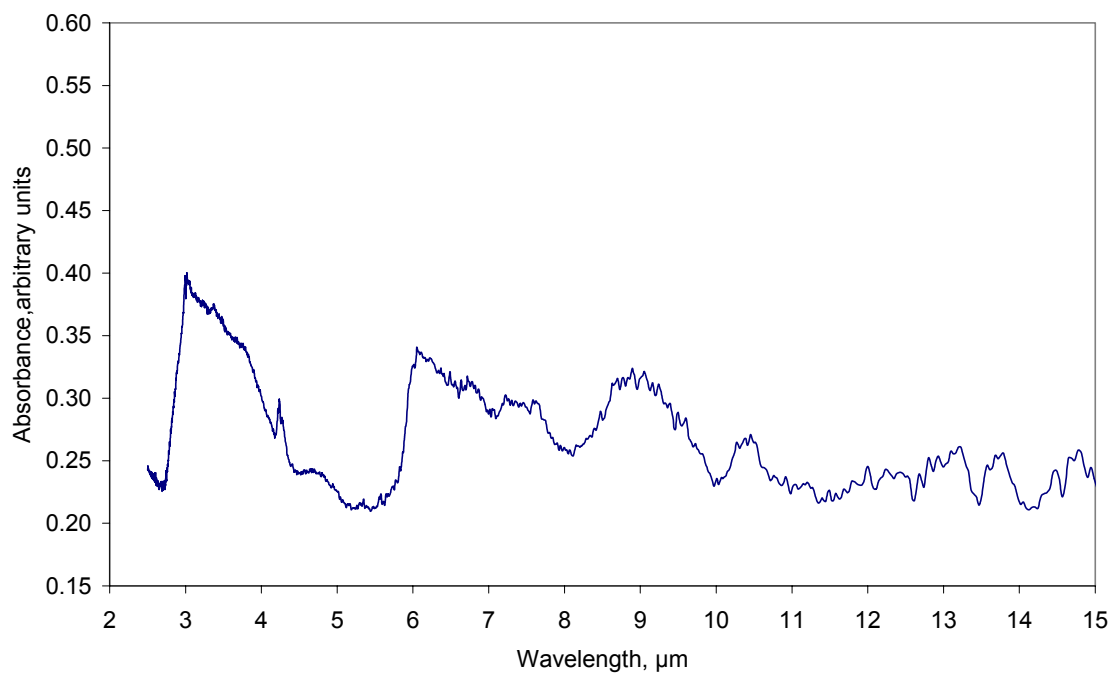


Figure VI.6 An FTIR spectrum of an Ag/ZnS 1 mm bore size sample, made using Recipe B (deposited with a flow rate of 9 mL/min for 69 minutes at room temperature).

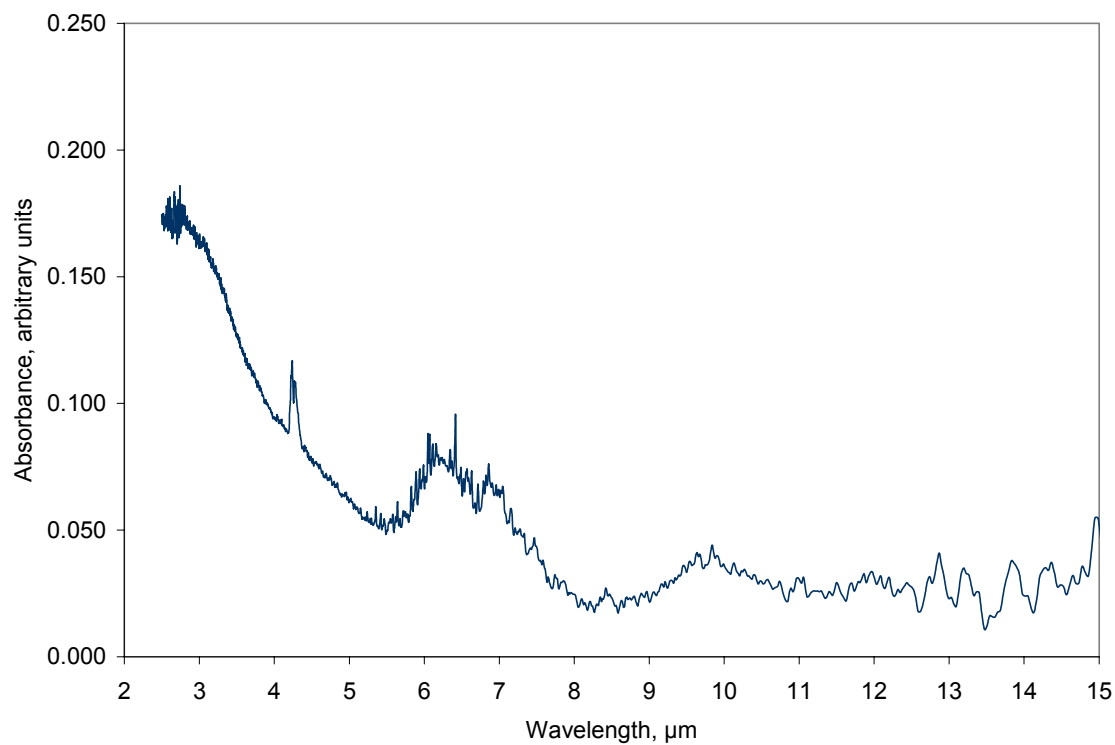


Figure VI.7 An FTIR spectrum of an Ag/ZnS 2mm bore size sample made, using Recipe C (deposited with a flow rate of 9 mL/min for 38 minutes at 62 °C). This sample differs from the other two samples since the deposition temperature was 62 °C, rather than room temperature as for the other two samples.

VI.D. ZnSe/ZnS Conclusions

The depositions here are not continuous optical quality films, with particles of Zn(OH)_2 and other reaction byproducts possibly present, as evidenced by the lack of well defined, narrow peaks in the FTIR spectra. Figure VI.4 indicates lowers concentrations of the S^{2-} ion source and more acidic conditions than used here would make the deposition of a continuous ZnS film of optical quality more likely.

In the future, the solution compositions should be changed to ensure solution stability for time periods on the order of hours. New solution compositions will primarily involve using different precursors and/or additives to allow depositions to be carried out at different pH levels. Acidic conditions have been successful for CBD deposition when zinc acetate was used as the precursor for Zn and thioacetamide for S.[1,3,6,8] Once Zn(OH)_2 and ZnO particle formation can be largely avoided, another important effort would be to determine the composition of these films. It may be beneficial to try to deposit Zn based films containing both Se and S from one solution. One solution may result in less Zn(OH)_2 formation with very little modification of the solution composition. Another situation would be two starting solutions with one solution containing the Zn ions and the other containing both S and Se ions. The presence of both anions may serve as impediments to Zn(OH)_2 particle formation and increase the total anion concentration. The higher concentration would make Se or S reaction with Zn more likely.

VI.E Gold (Au) Introduction

Au was studied because it can endure higher temperatures than Ag.[25] It is also extremely chemically inert and may be used as a substitute for silver in instances where minimal reactivity with the environment is required.[25] The inertness of Au and its high laser damage threshold make it a very attractive candidate for the metallic layer in HWs, especially ones with dielectric layers that are not chemically compatible with silver.

The deposition of Au is problematic because of poor adhesion to the glass substrate tubing. Often, after depositing for a mere 10 minutes or more the entire Au layer delaminated. There is also much pitting of the gold surface due to the incomplete coalescence of the isolated clusters that form in the initial nucleation stages and extreme solution instability. Some work has been done in the past in this group to develop a solution that reacts on a reasonable time scale to produce a gold layer. In the course of this project, a solution has been developed which does not require heating the substrate tubing and reacts more rapidly than previous solutions so that a more uniform gold layer can be produced in less time without significant pitting. A stable deposition solution was also developed so that there will not be such a great need for a significant increase in the rate of gold deposition.

VI.F Processing and Properties of Au

The first step in the deposition of Au is the deposition of a very thin film of silver on the glass tubing. This thin layer is called a flash of silver and it was deposited to form a layer upon which the gold can nucleate more evenly in an effort to increase the smoothness.

The most successful deposition was made with the following concentrations in 125mL of water, with a pH of 6.4 throughout the deposition. Many other solution compositions were tested. The composition of this solution is based largely on the bath in Ref.[26] of this chapter.

0.5 g gold (I) sodium thiosulfate - $\text{Na}_3\text{Au}(\text{S}_2\text{O}_3)_2 \cdot x\text{H}_2\text{O}$

1 g di-sodium hydrogen phosphate anhydrous - Na_2HPO_4

0.22 g L-ascorbic acid (Vitamin C) – $\text{C}_6\text{H}_8\text{O}_6$

All three precursors were mixed in one flask using a stir bar and then pumped through the sample and back to the flask, recirculating in this way for 30 minutes at a rate of 9 mL/min. This recirculation is not typical in this group and is a serious departure from the usual DLPD process used for all of the other depositions. The most notable advantage of the DLPD process over the CBD process is that unreacted solutions are continually pumped and mixed and brought into contact with the substrate surface while the solution that has had time to react and develop waste products is pumped away. The Au precursor is expensive and it was found that a possibly viable waveguide could be made with this recirculation. An Au sample, with an inner diameter of 500 μm was sent to Los Alamos for testing. No feedback was given. The optical constants for Au are given in Figure VI.8.

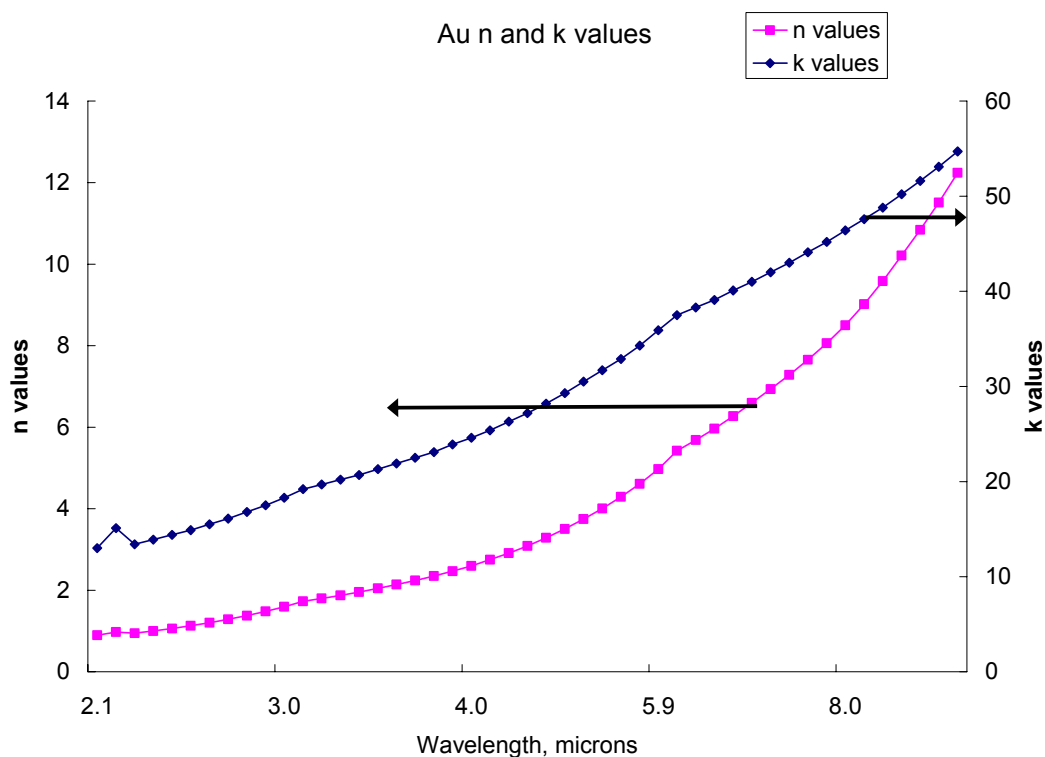


Figure VI.8 Optical constants for Au. [17]

VI.G Results and Discussion for Au

The Au depositions performed here resulted in an Au layer with a small amount of cracking and pitting and delamination visible through the WG wall. A picture of the outer surface of an Au coated tube, as viewed through an optical microscope, is shown in Figure VI.9. A picture of the inner surface of an Au coated tube, as viewed through an optical microscope is shown in Figure VI.10. While this layer is an improvement over previous results, further development would, ideally, result in a pit-free, crack-free layer, similar to the Ag layer that is routinely deposited.

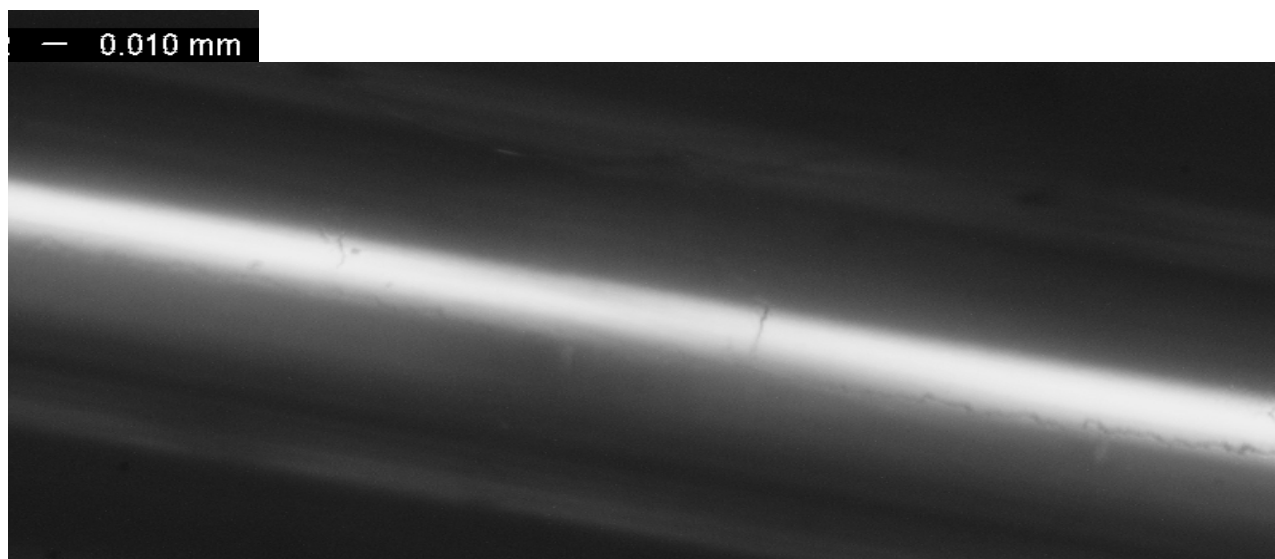


Figure VI.9 A picture of the outer surface of an Au coated tube, as viewed through an optical microscope. The solution composition is given above, the flow rate was 9 mL/min, deposition time was 15 minutes. Fine cracks, and a small area of delamination can be seen.

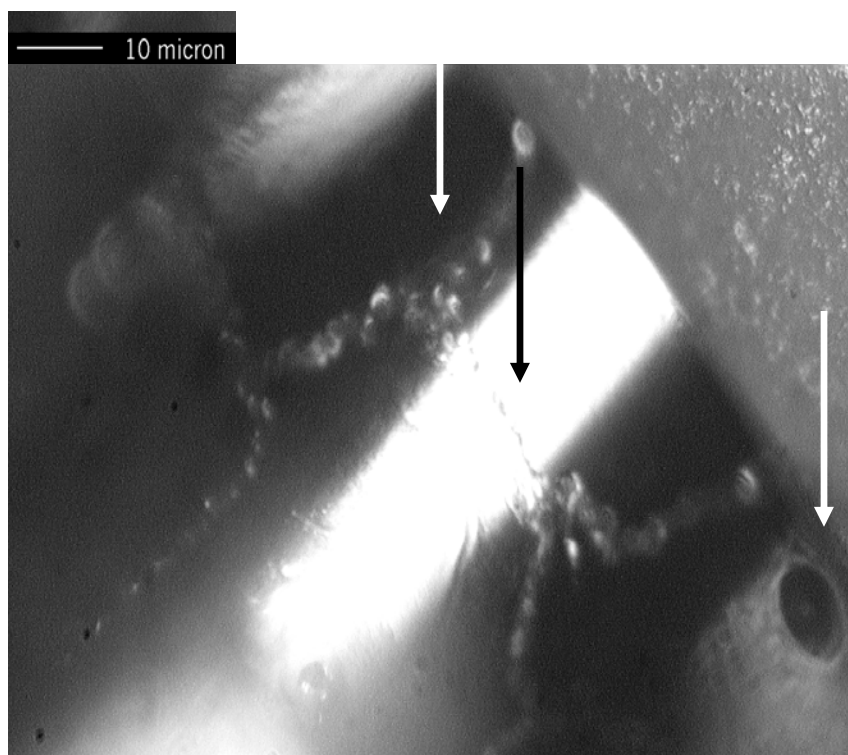


Figure VI.10 A picture of small area of the inner surface of an Au coated tube, as viewed through an optical microscope. The solution composition is given above, the flow rate was 9 mL/min and the deposition time was 20 minutes. Fine cracks (black arrow), and isolated areas of pitting (white arrows) can be seen.

Au, as an alternative to Ag, was also investigated by depositing ZnSe on an Au layer. As can be seen in Figure VI.11, the Au layer became severely blistered and the formation of Zn(OH)_2 particles dominated over ZnSe film formation. The deposition of Zn(OH)_2 particles is a significant issue in the ZnSe (and ZnS) deposition at this stage. This figure

Fig. VI.11) confirms the FTIR spectra in Figure VI.5 obtained from an Ag/ZnSe sample that optical quality ZnSe films are not forming.

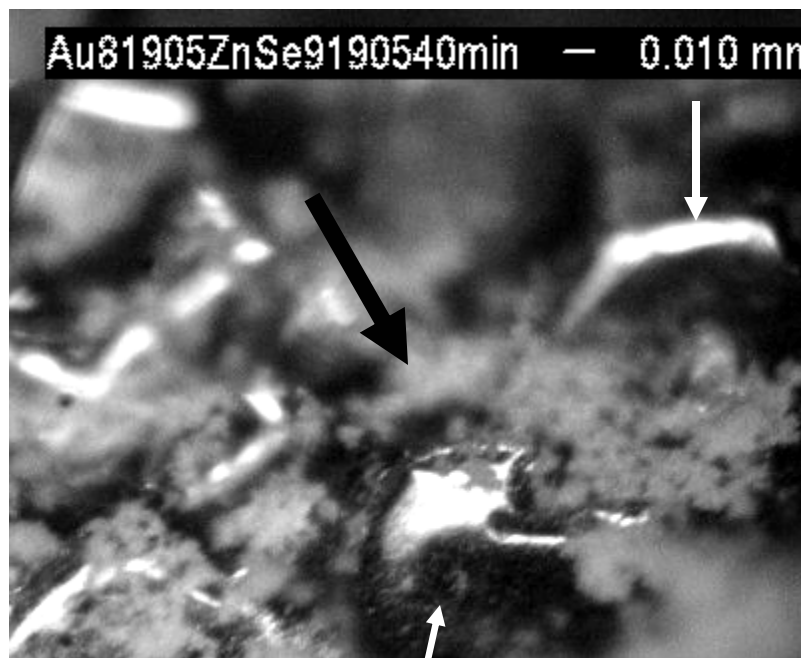


Figure VI.11 A picture taken from an optical microscope showing both the bubbling of the underlying Au layer (white arrows) and the particles (black arrow) formed during ZnSe deposition.

The single most significant impediment to successful deposition of optical quality Au films is bath stability. Most of the Au precursor is consumed in coating the container holding the solution rather than the substrate tubing. In addition, the reaction rate is so rapid that particles are formed in the bath. These particles are either imbedded or cause the pitting seen in Figure VI.10 during deposition when they are pumped through the

sample. Greater bath stability could also reduce the cracking that is typical for depositions lasting approximately 10 minutes or longer by ensuring that deposition conditions (especially solution composition and pH levels) are consistent throughout the deposition. Once bath stability has been established, the study of pretreatment of the glass surface to further eliminate cracking and possibly improve adhesion could be undertaken.

REFERENCES

1. Bayer, A., Boyle, D.S., O'Brien, P., "In situ kinetics studies of the chemical bath deposition of zinc sulfide from acidic solutions," *J Mater. Chem.* **12**, pp. 2940-2944 (2002).
2. Lewis, K.L., Cook, D.J., Roscoe, P.B., "The structure and optical properties of crystalline $\text{ZnS}_x\text{Se}_{1-x}$ prepared by chemical vapour deposition," *J of Crystal Growth* **56**, pp. 614-620 (1982).
3. Chaparro, A.M., Gutierrez, M.T., Herrero, J., "Quartz-crystal microbalance study of the growth of $\text{Zn}(\text{Se},\text{O})$ thin-films in a chemical bath. A sequential electroless-chemical process," *Electrochimica Acta* **47**, pp. 977-986 (2001).
4. Lokhande, C.D., Patil, P.S., Tributsch, H., Ennaoui, A., "ZnSe thin films by chemical bath deposition method," *Solar Energy Materials and Solar Cells* **55**, pp. 379-393 (1998).
5. O'Brien, P., Otway, D.J., Smyth-Boyle, D., "The importance of ternary complexes in defining basic conditions for the deposition of ZnS by aqueous chemical bath deposition," *Thin Solid Films* **361-362**, pp. 17-21 (2000).
6. Yamaguchi, K., Youshida, T., Lincot, D., Minoura, H., "Mechanistic study of chemical deposition of ZnS thin films from aqueous solutions containing zinc acetate and thioacetamide by comparison with homogeneous precipitation," *J Phys. Chem. B* **107**, pp. 387-397 (2003).
7. Johnston, D.A., Carletto, M.H., Reddy, K.T.R., et al., "Chemical bath deposition of zinc sulfide based buffer layers using low toxicity materials," *Thin Solid Films* **403-404**, pp. 102-106 (2002).
8. Makhova, L.V., Konovalov, I., Szargan, R., et al., "Composition and properties of ZnS thin films prepared by chemical bath deposition from acidic and basic solutions," *Phys. Stat. Sol.* **2(3)**, pp. 1206-1211 (2005).
9. Nasr, T.B., Kamoun, N., Guasch, C., "Structure, surface composition, and electronic properties of zinc sulphide thin films," *Materials Chemistry and Physics* **96**, pp. 84-89 (2006).
10. Antony, A., Murali, K.V., Manoj, R., Jayaraj, M.K., "The effect of the pH value on the growth and properties of chemical-bath-deposited ZnS thin films," *Materials Chemistry and Physics* **90**, pp. 106-110 (2005).
11. Cheng, J., Fan, D.B., Wang, H., et al., "Chemical bath deposition of crystalline ZnS thin films," *Semiconductor Science and Technology* **18**, pp. 676-679 (2003).

12. Oladeji, I.O., Chow, L., "A study of the effects of ammonium salts on chemical bath deposited zinc sulfide thin films," *Thin Solid Films* **339**, pp. 148-153 (1999).
13. Doña, J.M., Herrero, J., "Chemical bath codeposited CdS-ZnS film characterization," *Thin Solid Films* **268**, pp. 5-12 (1995).
14. Matsuura, Y., Miyagi, M., "Er:YAG, CO, and CO₂ laser delivery by ZnS-coated Ag hollow waveguides," *Appl. Opt.* **32**(33), pp. 6598-6601 (1993).
15. Matsuura, Y., Miyagi, M., "Low-loss metallic hollow waveguides coated with durable and nontoxic ZnS," *Appl. Phys. Lett.* **61**(14), pp. 1622-1623 (1992).
16. Matsuura, Y., Miyagi, M., "Bending losses and beam profiles of zinc selenide-coated silver waveguides for carbon dioxide laser light," *Appl. Opt.* **31**(30), pp. 6441-6445 (1992).
17. Edited by Palik, E.D., *Handbook of Optical Constants of Solids*, Academic Press, New York, 1985.
18. O'Brien, P., McAleese, J., "Developing an understanding of the processes controlling the chemical bath deposition of ZnS and CdS," *J. of Materials Chemistry* **8**(11), pp.2309-2314 (1998).
19. Ramaiah, K.S., Pilkington, R.D., Hill, A.E., et al., "Structural and optical investigations on CdS thin films grown by chemical bath technique," *Materials Chemistry and Physics* **68**, pp.22-30 (2001).
20. Kostoglou, M., Andritsos, N., Karabelas, A.J., "Progress towards modeling the CdS chemical bath deposition process," *Thin Solid Films* **387**, pp. 115-117 (2001).
21. Gopal, V., *New Dielectric Coatings for Low-Loss Hollow Glass Waveguides and Bundles*, Rutgers University thesis, 2003.
22. Doña, J.M., Herrero, J., "Chemical-bath deposition of ZnSe thin films," *J Electrochem Soc.*, **142**(3), pp. 764-770 (1995).
23. Pejova, B., Grozdanov, I., "Chemical deposition and characterization of Cu₂Se₂ and CuSe thin films," *J Solid State Chemistry* **158**, pp.49-54 (2001).
24. Grozdanov, I., Najdoski, M., Dey, S.K., "A simple solution growth technique for PbSe thin films," *Mat. Lett.* **38**, pp.28-32 (1999).
25. Matsuura, K., Matsuura, Y., Harrington, J.A., "Evaluation of gold, silver, and dielectric-coated hollow glass waveguides," *Opt. Eng.* **35**(12), pp.3418-3421 (1996).

26. Sullivan, A.M., Kohl, P.A., "The autocatalytic deposition of gold in nonalkaline, gold thiosulfate electroless bath," *J of the Electrochem. Soc.* **142**(7), pp.2250-2255 (1995).

Chapter VII. Conclusions and Future Work

Several different materials were investigated in the course of this work. The materials considered were PbS as a single dielectric layer, PS as a single dielectric layer and as part of a dielectric pair with PbS and CdS, ZnS, ZnSe and Au. The effort the ZnS and ZnSe depositions was exploratory and began the development of a deposition process for these dielectrics. Au was considered as a replacement for Ag because of its superior ability to withstand extreme heat and chemical attack.[2] PS was deposited by DLDP for the first time in the course of this work.[1]

The deposition of PS by DLDP is the greatest achievement in this project. A new dielectric material for HGWs was discovered. The potential to use this material with other high index inorganic dielectric materials has also been realized. The demonstrated ability to deposit a metal sulfide on the polymer surfaces from basic solutions with no pretreatment of the polymer surface is remarkable. The two dielectrics paired with PS may not be ideal candidates for use with PS, practically, in terms of fabrication. Attempts to deposit high index inorganic dielectrics on polymer surfaces should continue until a practical pair is found.

It is clear, based on the optical constants and absorption behavior presented in Chapter IV, that PS is best suited for use at shorter wavelengths ($< 3 \mu\text{m}$). If the optimal drying conditions are established and surface roughness can be minimized, transmission at shorter wavelengths would likely be more efficient. The Omniguide® is evidence that materials with high intrinsic losses can be used in multilayer HWs. If surface roughness

is not too great with ten or more layers then the low loss wavelength range of Ag/PS could be extended in Ag-coated HGWs to beyond 10 μm .

Ag/PbS HGWs with the lowest straight losses for 10.6 μm were made. A loss of 0.1 dB/m was achieved for a 1 mm bore sample. The experimental losses for the other bore sizes were consistently three times greater than the theoretical values. The higher loss is likely due to the surface roughness of the PbS layer, which compounded the effect of the Ag layer roughness.[3]

In the future, to determine if the comparison between Ag/AgI samples and Ag/PbS samples made here are reasonable, some study of the interface between the different pairs should be undertaken. The difference between the two materials in terms of composition in the Ag/AgI pair is not nearly as great as for the Ag/PbS pair. The interface between the two materials in the two pairs should be characterized so that more insightful comparisons between these two pairs, or between Ag/AgI and any other pair that does not include an Ag halide, can be made. Ag/AgI can be considered a reference material pair because the theoretical loss values at 10.6 μm have been measured experimentally.

Metal-only (Au) WGs were fabricated here with minimal cracking and no delamination. One sample was made for use with x-rays for an external user but no feedback was received. The depositions done in this project could be described as moderately successful. Since an Au layer that is totally pit-free and crack-free has not yet been deposited. Further efforts are needed on this material.

Au is a worthwhile material to continue to develop. Temperature measurement and chemical sensing and measuring are application arenas that require the unique properties of Au in order for HGWs to be viable options. There is also the potential to deposit a dielectric on this metal when deposition on Ag proves difficult or impossible. A comparative study of the strength of adhesion to the glass substrate of Ag and Au would also be informative.

There are several groups describing Au deposition at high temperatures.[4-6] The construction of an adiabatic chamber in which to perform Au depositions may be needed for optimal thin film quality. Another impediment to successful Au deposition is the lack of stable deposition solutions. Often, Au was coating the flask containing the solution instead of the glass tubing. Also, most of the depositions done in this work were done under acidic conditions. Neutral or basic pH levels may yield better results.

Deposition solutions containing different gold precursors (gold (I, III) chloride, gold sodium thiosulfate hydrate), complexing agents and pH adjusters (sodium sulfate, sodium sulfite, di-sodium hydrogen phosphate anhydrous) and reducers (formaldehyde and L-ascorbic acid) were studied. Depositions were also carried out at room temperature and higher temperature (62 °C) and under basic and slightly acidic conditions.

ZnS and ZnSe are well known optical materials used in lenses and filters. The deposition of these materials via DLPD is chemically challenging. The obvious technological

achievement would be fabrication of single dielectric layer HGWs that could transmit longer wavelengths ($> 10.6 \mu\text{m}$) of IR radiation. Based on the results obtained here and the review of the literature presented, deposition of optical quality thin films may be possible under more acidic conditions (pH levels less than 4). Also, since most of the work here was done using zinc sulfate and thiourea as precursors for zinc and sulfur, respectively, it is necessary to explore different precursors.

Single and multilayer dielectric coated HGWs have the potential to incorporate many materials to achieve low loss IR transmission. The wet chemistry electroless DLPD process requires complex chemistry to be understood and applied. Indeed the most appropriate solution compositions and deposition conditions requires an evolutionary development process that must continue to allow HWs to remain relevant devices.

As indicated by the theoretical handling of this topic, the material pairing that has the greatest index contrast between the two dielectrics would be the most interesting for multilayer HWs with 3 layers or fewer. In this project the greatest index contrast was obtained using the PS/PbS pairing. If surface roughness is an impediment to low loss transmission of Er:YAG or CO_2 laser radiation, another dielectric pair that seems promising in the long term is the ZnS(ZnSe)/PbSe. These pairs are long term goals because these materials have not yet been deposited by this group using the DLPD process. Still, they are of interest because the materials have been deposited by other means and there is a large index contrast between these materials.

REFERENCES

1. Johnson, V.S., Bowden, B., Harrington, J., "Polymer/Metal Sulfide Coated Hollow Glass Waveguides for Delivery of Er:YAG Laser Radiation", *Proc. SPIE* **6433**, pp.64330E1-8 (2007).
2. Matsuura, K., Matsuura, Y., Harrington, J.A., "Evaluation of gold, silver, and dielectric-coated hollow glass waveguides," *Opt. Eng.* **35**(12), pp.3418-3421 (1996).
3. George, R., New dielectric thin film coatings for Ag and Cu coated hollow infrared waveguides, Rutgers University thesis, 2004.
4. Ando, S., Inoue, T., Okudaira, H., et al., "Super stable non-cyanide electroless gold plating bath which as been applied to advanced wiring board manufacture," *IEMT/IMC Proceedings*, pp.220-225 (1997).
5. Iacovangelo, C.D., Zarnoch, K.P., "Substrate-catalyzed electroless gold plating," *J Electrochem. Soc.* **138**(4), pp. 983-988 (1991).
6. Vorobyova, T.N., Poznyak, S.K., Rimskaya, A.A., et al., "Electroless gold pating from a hypophosphite-dicyanoaurate bath," *Surface and Coatings Technology* **176**, pp. 327-336 (2004).

VITA

Valencia Serena Johnson

- 1977 Born June 8 in Brooklyn, New York.
- 1995 Graduated from West Windsor-Plainsboro High School, Princeton Junction, New Jersey.
- 1999 B.S., Johns Hopkins University.
- 2000 Management Associate-Quality Assurance, US Steel, Pittsburgh, Pennsylvania.
- 2001-04 Graduate work in Materials Engineering, Stevens Institute of Technology, Hoboken, New Jersey.
- 2001-03 Teaching Assistant, Physics Department and Chemical, Biomedical and Materials Engineering Department.
- 2002 M.S., Stevens Institute of Technology, Hoboken, New Jersey.
- 2004 Article: S. Marjanovic, J. Toulouse, M. F. Yan, V. S. Johnson, P. W. Wisk, A. R. Kortan, N. Kopylov, R. G. Ahrens, “Erbium Emission in Highly Doped Tellurite and Alumina-Silica Novelty Fibers”, *Optical Fiber Communication Conference (OFC 2004)*, **2**, pp.23-27.
- 2005-07 Graduate work in Materials Science and Engineering, Rutgers University, Piscataway, New Jersey.
- 2006 Article: Aparajita Bandyopadhyay, Amartya Sengupta, Valencia Johnson, James A. Harrington and John F. Federici, “Characterization of Guided THz Propagation Mode in Hollow Polycarbonate Metal Waveguides”, *Proc. SPIE* **6120**, 61200B1.
- 2007 Article: Valencia S. Johnson, Bradley Bowden and James Harrington, “Polymer/Metal Sulfide Coated Hollow Glass Waveguides for Delivery of Er:YAG Laser Radiation”, *Proc. SPIE* **6433**, pp.64330E1-8.
- 2007 1st Place Graduate Student Poster: Polystyrene/Metal Sulfide Coated Hollow Glass Waveguides for Delivery of Er:YAG Laser Radiation”, at Joint Annual

Conference of National Society of Black Physicists/Nat.l Soc. Of Hispanic Physicists,
Boston, MA by OSA/SPIE.

2007 Ph.D. in Materials Science and Engineering.